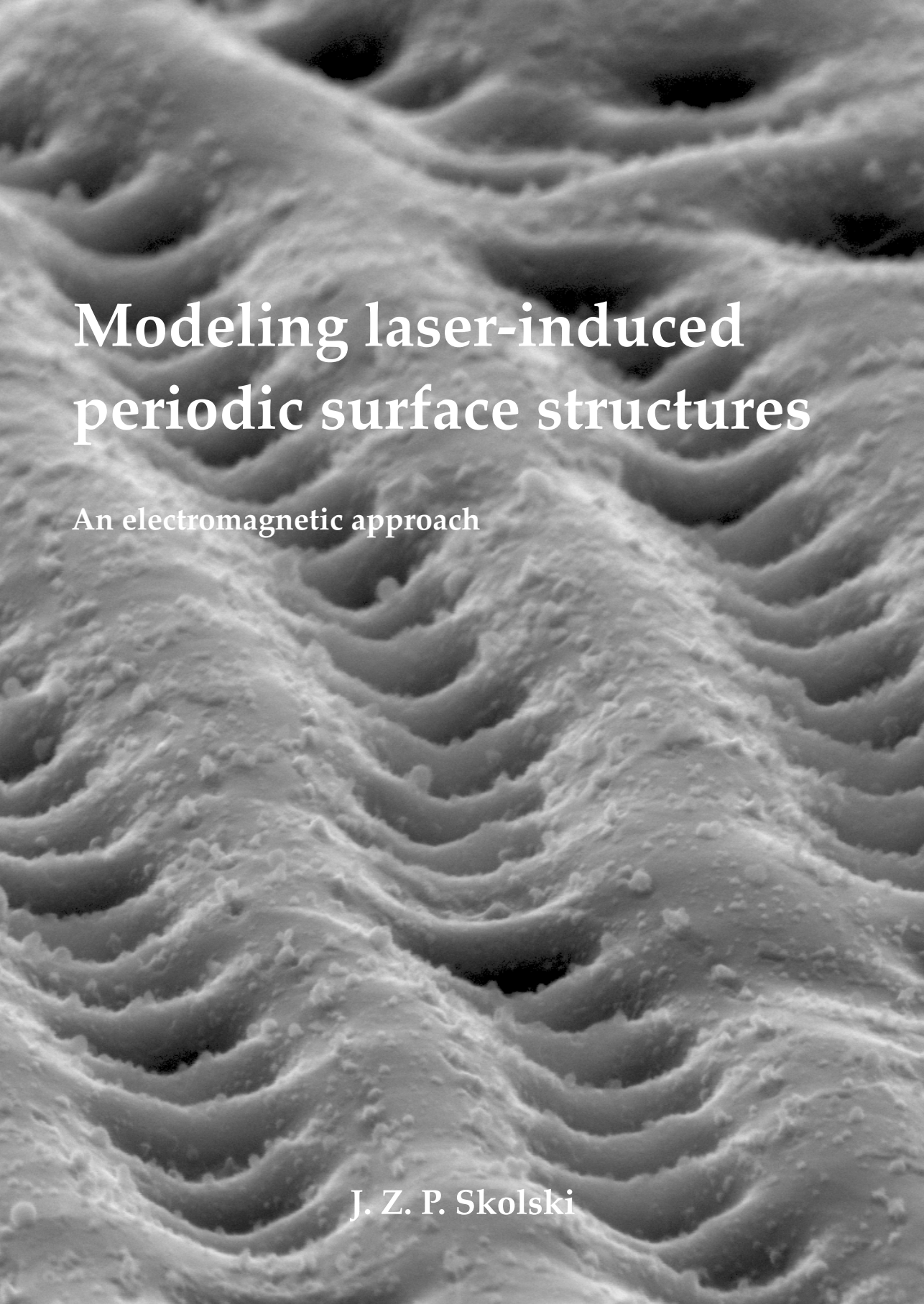

Modeling laser-induced periodic surface structures

An electromagnetic approach

J. Z. P. Skolski

MODELING LASER-INDUCED PERIODIC SURFACE STRUCTURES

AN ELECTROMAGNETIC APPROACH

Johann Zbigniew Pierre Skolski

Composition of the graduation committee:

Chairman and secretary:

prof.dr. G.P.M.R. Dewulf	University of Twente

Promoter and assistant-promoter:

prof.dr.ir. A.J. Huis in 't Veld	University of Twente
dr.ir. G.R.B.E. Römer	University of Twente

Members:

prof.dr. J. Reif	Brandenburg University of Technology
prof.dr. J.Th.M. De Hosson	University of Groningen
prof.dr. K.J. Boller	University of Twente
prof.dr.ir. H.J.W. Zandvliet	University of Twente
prof.dr.ir. A.H. van den Boogaard	University of Twente

The work described in this thesis was performed at the group of Mechanical Automation of the Faculty of Engineering Technology, Chair of Applied Laser Technology, University of Twente, P.O. Box 217, 7500 AE Enschede, The Netherlands.

This research was carried out under project number M61.3.08300 in the framework of the Research Program of the Materials innovation institute (M2i) in the Netherlands (www.m2i.nl).

On the cover, a scanning electron microscopy image of laser-induced periodic surface structures, taken by Jozef Vincenc Obona.

Modeling laser-induced periodic surface structures
J.Z.P Skolski
PhD Thesis, University of Twente, Enschede, The Netherlands
April 2014

ISBN 978-94-91909-07-8

Printed by Gildeprint.

MODELING LASER-INDUCED PERIODIC SURFACE STRUCTURES

AN ELECTROMAGNETIC APPROACH

DISSERTATION

to obtain
the degree of doctor at the University of Twente,
on the authority of the rector magnificus,
prof. dr. H. Brinksma,
on account of the decision of the graduation committee,
to be publicly defended
on Thursday 17$^{\text{th}}$ of April 2014 at 14.45

by

Johann Zbigniew Pierre Skolski

born on 14 October 1985
in Lille, France

This thesis has been approved by the promoter
prof.dr.ir. A.J. Huis in 't Veld

and the assistant-promoter
dr.ir. G.R.B.E Römer

Summary

This thesis presents and discusses laser-induced periodic surface structures (LIPSSs), as well as a model explaining their formation.

LIPSSs are regular wavy surface structures with dimensions usually in the submicrometer range, which can develop on the surface of many materials exposed to laser radiation. The most common type of LIPSSs, which can be produced with continuous wave lasers or pulsed lasers, have a periodicity close to the laser wavelength and a direction orthogonal to the polarization of the laser radiation. They are usually referred to as low spatial frequency LIPSSs (LSFLs). It is generally accepted that these LIPSSs are the result of the interaction of the laser radiation with the rough surface of the material. The "Sipe theory" is commonly considered to be the most adequate theoretical description of this interaction.

Since the early 2000s, with the increasing availability of picosecond and femtosecond laser sources, LIPSSs with a periodicity significantly smaller than the laser wavelength and an orientation either parallel or orthogonal to the polarization have been reported in literature. These LIPSSs, referred to as high spatial frequency LIPSSs (HSFLs), renewed the interest of researchers in the topic for mainly two reasons. First, from a practical point of view, HSFLs show a strong potential for surface nanostructuring due to their small dimensions. While, from a theoretical point of view, the electromagnetic theory adopted to explain LSFL formation fails at accounting for the formation of all HSFLs. Other LIPSSs with a periodicity larger than the laser wavelength and an orientation either parallel or orthogonal to the polarization, referred to as grooves, were also reported.

The Sipe theory provides an analytical solution of Maxwell's equations regarding the interaction of electromagnetic waves with rough surfaces. The main outcome of this theory is the prediction of the frequency domain spectrum of the absorbed laser energy just below the rough surface of the material. The spectrum shows that the interaction of electromagnetic waves with rough surfaces results in a periodic energy profile, with a periodicity close to the wavelength of the laser radiation, in the direction orthogonal to the polarization. In addition, a careful study of the

Sipe theory reveals that the formation of certain kinds of HSFLs can be explained. However, the assumptions and approximations used to derive the Sipe theory hinder the conclusions.

To overcome some of the limitations of the Sipe theory, a numerical model, based on the finite-difference time-domain (FDTD) method, was developed. The FDTD method solves the time dependent Maxwell's curl equations in differential form and allows to simulate the interaction of electromagnetic waves with rough surfaces, providing adequate boundary conditions are chosen. The results of the FDTD simulations are in agreement with the Sipe theory, but also show that the latter is incomplete. By studying the absorbed energy profile as a function of the depth below the rough surface of the material, in the space domain as well as in the frequency domain, it is shown that the FDTD simulations can account for the formation of LSFLs and HSFLs.

Next, the FDTD calculations are coupled with an holographic ablation model to investigate the role of inter-pulse feedback mechanisms. That is, the absorbed energy profile, computed with the FDTD method, is used to modify the rough surface of the simulation domain by "material removal". FDTD simulations are performed on the new surface morphology in order to obtain a new absorbed energy profile. This process is iterated to study the "pulse to pulse" growth of LIPSSs. In the framework of this approach, LSFLs, HSFLs orthogonal to the polarization, HSFLs parallel to the polarization and grooves parallel to the polarization form in the simulation domain. The type of LIPSSs obtained depends on the optical properties of the material and on the quantity of material removed per iteration. LIPSSs are found to be the fingerprints of the interaction of electromagnetic waves with rough surfaces. Each kind of LIPSSs has a specific signature in the frequency domain.

HSFLs orthogonal to the polarization, and their signature in the frequency domain, are only predicted by the model developed in this thesis. It is shown that these HSFLs develop on sapphire and that a good match is found between the theoretical predictions and the experiments.

Publications

Journal articles

J. Z. P. Skolski, G. R. B. E. Römer, A. J. Huis in 't Veld, V. S. Mitko, J. Vincenc Obona, V. Ocelik, and J. Th. M. de Hosson. Modeling of laser induced periodic surface structures. *Journal of Laser Micro/Nanoengineering*, 5:263-268, 2010. Presented during LPM 2010.

J. Vincenc Obona, V. Ocelik, J. Z. P. Skolski, V. S. Mitko, G. R. B. E. Römer, A. J. Huis in 't Veld, and J. Th. M. de Hosson. On the surface topography of ultrashort laser pulse treated steel surfaces. *Applied Surface Science*, 258:1555-1560, 2011.

J. Z. P. Skolski, G. R. B. E. Römer, J. Vincenc Obona, V. Ocelik, A. J. Huis in 't Veld, and J. Th. M. de Hosson. Laser-induced periodic surface structures: Fingerprints of light localization. *Physical Review B*, 85:075320-1-9, 2012.

J. Z. P. Skolski, G. R. B. E. Römer, J. Vincenc Obona, V. Ocelik, A. J. Huis in 't Veld, and J. Th. M. de Hosson. Inhomogeneous absorption of laser radiation: Trigger of LIPSS formation. *Journal of Laser Micro/Nanoengineering*, 8:1-5, 2013. Presented during LPM 2012.

J. Z. P. Skolski, G. R. B. E. Römer, J. Vincenc Obona, and A. J. Huis in 't Veld. Modeling laser-induced periodic surface structures: Finite-difference time-domain feedback simulations. *Journal of Applied Physics*, 115:103102-1-12, 2014.

J. Vincenc Obona, V. Ocelik, J. C. Rao, J. Z. P. Skolski, G. R. B. E. Römer, A. J. Huis in 't Veld, and J. Th. M. de Hosson. Modification of Cu surface with picosecond laser pulses. *Applied Surface Science*, 2014. *to be published*

J. Vincenc Obona, J. Z. P. Skolski, G. R. B. E. Römer, and A. J. Huis in 't Veld. Pulse-analysis-pulse investigation of femtosecond laser-induced periodic surface structures on silicon in air. *under review*, 2014.

Conference articles

J. Vincenc Obona, V. Ocelik, J. Z. P. Skolski, V. S. Mitko, G. R. B. E. Römer, A. J. Huis in 't Veld, and J. Th. M. de Hosson. Surface melting of copper by ultrashort laser pulses. *WIT Transactions on Engineering Sciences*, 71:171-179, 2011.

V. S. Mitko, G. R. B. E. Römer, A. J. Huis in 't Veld, J. Z. P. Skolski, J. Vincenc Obona, V. Ocelik, and J. Th. M. de Hosson. Properties of high-frequency sub-wavelength ripples on stainless steel 304L under ultra short pulse laser irradiation. *Physics Procedia*, 12:99-104, 2011.

D. Scorticati, J. Z. P. Skolski, G. R. B. E. Römer, A. J. Huis in 't Veld, M. Workum, M. Theelen, and M. Zeman. Thin film surface processing by ultrashort laser pulses (USLP). *Proceedings of SPIE - The International Society for Optical Engineering*. 8438:84380T-1-8, 2012.

D. Scorticati, A. Illiberi, G. R. B. E. Römer, T. Bor, W. Ogieglo, M. Klein Gunnewiek, A. Lenferink, C. Otto, J. Z. P. Skolski, F. Grob, D. F. de Lange, and A. J. Huis in 't Veld. Optical and electrical properties of SnO_2 thin films after ultra-short pulsed laser annealing. *Proceedings of SPIE - The International Society for Optical Engineering*. 8826:88260I-1-12, 2013.

G. R. B. E. Römer, J. Z. P. Skolski, J. Vincenc Obona, V. Ocelik, J. Th. M. de Hosson, and A. J. Huis in 't Veld. Laser-induced periodic surface structures, modelling, experiments and applications. *Proceedings of SPIE - The International Society for Optical Engineering*, 8968:89680D-1-9, 2014.

Contents

Chapter 1

Introduction

In this chapter, laser-induced periodic surface structures are introduced, as well as the goal and the outline of this thesis.

1.1 Background

Laser-induced periodic surface structures (LIPSSs) have been studied since the 1960s [1] and observed on many types of materials [2–8]. The most common LIPSSs, also referred to as ripples, consist of wavy surfaces which can be produced on metals [2, 3], semiconductors [4, 5], dielectrics [6] and polymers [7, 8]. When created with linearly polarized laser radiation at normal incidence, these ripples have a periodicity close to the laser wavelength, a height in the hundreds of nanometer range [9, 10] and a direction mostly orthogonal to the polarization of the laser radiation [2–6]. Ripples having these properties can be produced with either continuous wave lasers [11] or pulsed lasers [5, 12] and are usually referred to as low spatial frequency LIPSSs (LSFLs). Typical LSFLs observed on 800H alloyed steel after 800 nm femtosecond laser irradiation are shown in Figure 1.1(a). The cross-section presented in Figure 1.1(b) reveals a LSFL periodicity close to the laser wavelength ($\approx 700\,\text{nm}$) and a height, peak to valley, of about 150 nm. It is generally accepted that LSFL formation is driven by the interaction of electromagnetic waves with the rough surface of materials [4, 13].

Recently, a new kind of ripples has been observed. When applying picosecond or femtosecond laser pulses, ripples with a periodicity significantly smaller than the laser wavelength, referred to as high spatial frequency LIPSSs (HSFLs), can develop [12, 14–27]. As for LSFLs, HSFLs can be produced on metals [14–17], semiconductors [12, 18–23] and dielectrics [24–27]. On the contrary to LSFLs, HSFLs produced at normal incidence of the laser beam can develop either parallel or orthogonal to the polarization. Examples of HSFLs are shown in Figure 1.2(a)

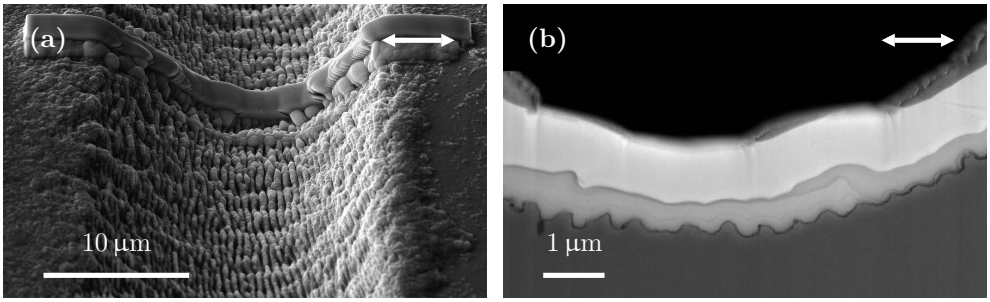

Figure 1.1: (a) 55 ° tilted scanning electron microscopy (SEM) image of typical LSFLs observed on 800H alloyed steel, in a trench of ablated material, after 800 nm femtosecond laser irradiation. (b) SEM image of a transmission electron microscopy lamella. The region from which the lamella was extracted is visible in (a). The polarization direction is indicated by the white arrows in (a) and (b).

and Figure 1.2(b). In Figure 1.2(a), HSFLs observed on sapphire are orthogonal to the laser beam polarization and have a periodicity of about a third of the laser wavelength. In Figure 1.2(b) HSFLs obtained on silicon are parallel to the polarization, while coexisting with LSFLs orthogonal to the polarization, and have a periodicity of about a fifth of the laser wavelength. The height of HSFLs can vary significantly, from tens of nanometers [28, 29] to about a micrometer [10], depending on the material and the laser processing conditions. The physical phenomena leading to the formation of HSFLs are still under debate and several theories have been proposed to explain their formation, such as self-organization [22, 24], second-harmonic generation [12, 18, 21] or by extending the classical electromagnetic waves approach used to understand LSFL formation [21, 27].

LIPSSs can be used for various applications such as colorizing metals [30, 31], controlling tribological properties [32, 33] or modifying the wetting properties of surfaces [34, 35]. Moreover, HSFLs show a strong potential for nanostructuring due to their small dimensions.

1.2 Problem definition

The origin and growth of LIPSSs is still subject of intensive studies [12, 18, 21, 22, 24, 27]. While LSFL formation is relatively well understood for short laser pulses (typically nanosecond pulses) [13], LIPSSs developing under ultra-short laser pulses (picosecond or femtosecond pulses) irradiation show unexplained properties. (i) The periodicity of LSFLs produced under these conditions does not follow strictly the wavelength of the laser light [12, 14, 22, 27, 36–39], in apparent disagreement with the classical electromagnetic theory. (ii) Explanations for the periodicity of HSFLs, significantly smaller than the wavelength of the laser radiation, and their orientation,

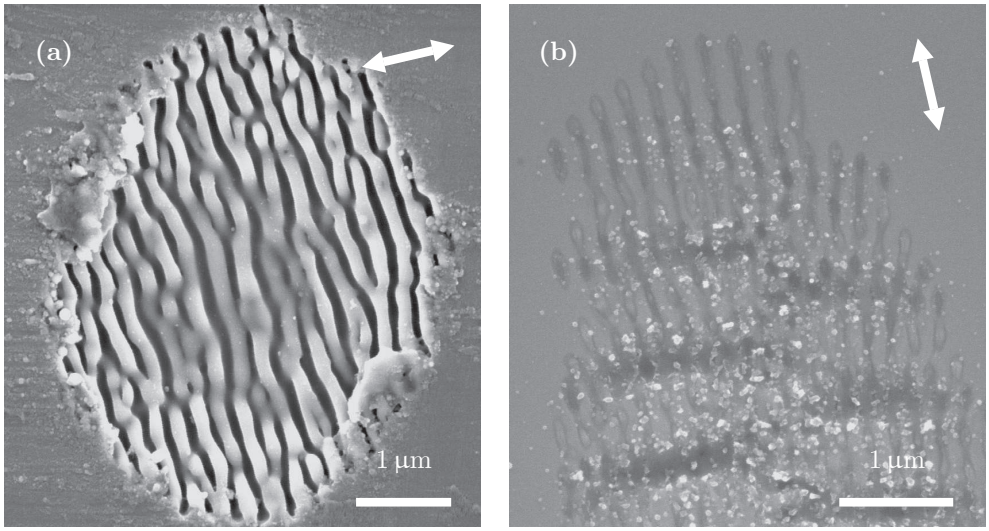

Figure 1.2: (a) SEM image of HSFLs observed on sapphire after 800 nm femtosecond irradiation. (b) SEM image of HSFLs, running vertically, observed on silicon after 1030 nm picosecond irradiation. The onset of LSFL formation, running horizontally, is visible. The polarization direction is indicated by the white arrows in (a) and (b).

either parallel or orthogonal to the polarization of the laser beam, are lacking. (iii) LIPSSs with periodicities larger than the laser wavelength have also been observed. The physics of their formation remains unexplained [12, 39, 40].

From the plethora of new phenomena observed during the last decade, few received explanations [12, 18, 21, 27]. These explanations involved mainly the classical electromagnetic waves approach with extensions. Indeed, the dependence of the periodicity and orientation of LIPSSs on the laser wavelength and polarization suggests that electromagnetic waves are involved in their origin and growth. However, the formation of many LIPSSs remain ununderstood and self-organization was proposed as a mechanism leading to their occurrence [22, 24]. Other effects involving melt dynamics, such as capillary waves, thus surface tension and viscosity, are also known to play a role [41]. The problem discussed in this thesis is therefore formulated as follows: what are the LIPSSs features which can be explained in the frame of an electromagnetic approach?

1.3 Outline

Chapter 2 presents a detailed description of the LIPSSs observed in literature as well as the main theories aimed at explaining their origin and growth. The goal of

this chapter is to describe and classify LIPSSs according to their appearance in terms of periodicities and orientations. This classification is necessary to judge the quality of the models.

Chapter 3 discusses the strengths and limitations of the most promising model found in chapter 2, the Sipe theory [13]. This theory provides an analytical solution of Maxwell's equations regarding the interaction of electromagnetic waves with rough surfaces. The frequency domain spectrum of the absorbed energy, just below the rough surface of materials, is predicted in the frame of the Sipe theory, and interpreted in order to understand LIPSS formation.

Chapter 4 describes a numerical model solving Maxwell's equations, based on the finite-difference time-domain method (FDTD) [42]. The aim of this approach is to overcome some of the limitations of the Sipe theory, identified in chapter 3. The theoretical background necessary to perform the FDTD calculations is presented before discussing the FDTD algorithm and the related boundary conditions.

Chapter 5 is dedicated to the results obtained with the numerical model described in chapter 4. First, the parameters and the simulation domain used in the FDTD calculations are defined. Second, the results of the FDTD calculations are compared to the Sipe theory. Finally, the advantages of the numerical method are highlighted.

Chapter 6 extends the model presented in chapter 4 and chapter 5, by considering inter-pulse feedback mechanisms. The initiation and growth of LIPSS is simulated and discussed with respect to the classification established in chapter 2.

Chapter 7 presents some results of experiments performed with a femtosecond laser source. The experimental results allow the validation of the numerical model, for the case where corresponding experimental data was lacking from literature.

Chapter 8 summarizes the conclusions presented throughout the chapters of this thesis. Suggestions for future research are discussed.

Finally, the **Bibliography**, **Nomenclature** and **Acknowledgments** can be found on page 111, 119 and 123, respectively.

Chapter 2

State of the art

This chapter provides a detailed description of the characteristics of LIPSSs. Here, LIPSSs are classified according to their periodicity and orientation with respect to the polarization of the incident laser light. Theories that have been proposed to explain the origin and the growth of the LIPSSs are presented and evaluated.

2.1 Characteristics of laser-induced periodic surface structures

The spatial characteristics, i.e. periodicity, height and orientation, of LIPSSs depend on material properties and on the laser parameters, such as the wavelength and the polarization of the laser radiation. However, many other parameters are involved in LIPSS formation. Figure 2.1 shows the main parameters influencing LIPSSs principal characteristics, which are their periodicity Λ, height (peak to valley) h and orientation. The laser beam is described by its wavelength λ, angle of incidence θ and direction of polarization. In most cases, the applied polarization is linear but LIPSS formation has also been investigated for circular [16, 43, 44], elliptical [45, 46] or even radial and azimuthal polarized light [47]. For pulsed lasers, the pulse duration τ is of importance, since most of the unexplained phenomena, such as HSFL formation or the variation of LSFL periodicity, occur when ultra-short laser pulses (picosecond of femtosecond pulses) are applied. The energy of the pulse E_p is usually described by the fluence ϕ (energy per surface area) applied to the surface of the material. The number of subsequent pulses N applied to the same location on the surface also affects LIPSSs characteristics. In the following sections, the effects of these laser parameters on LSFLs, HSFLs and other LIPSSs characteristics are described.

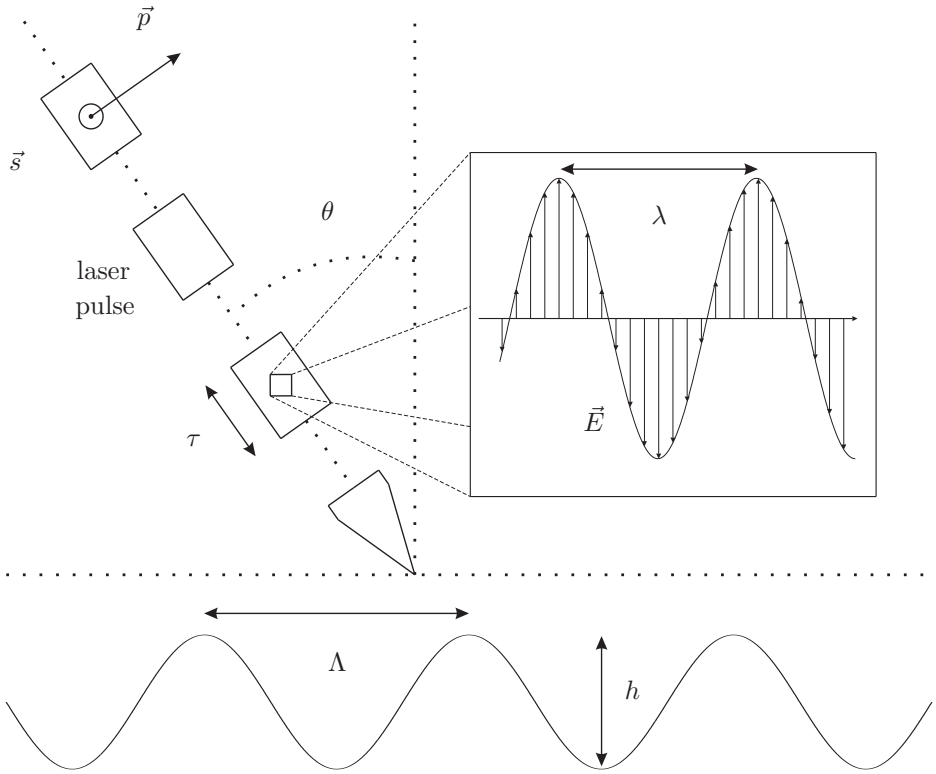

Figure 2.1: The main parameters and the notations used to described LIPSSs as well as the laser parameters. λ is the wavelength of the laser light, θ the angle of incidence, τ the pulse duration, $\vec{p}$ the component of the laser beam polarization parallel to the plane of incidence, $\vec{s}$ the component of the laser beam polarization orthogonal to the plane of incidence, $\vec{E}$ the electric field, Λ the periodicity of LIPSSs and h the height (peak to valley) of LIPSSs.

2.1.1 Low spatial frequency laser-induced periodic surface structures

LSFLs are the most observed kind of LIPSSs. They have been observed on metals [2, 3], semiconductors [4, 5] and dielectrics [6]. At normal incidence of the laser beam, LSFLs show a periodicity close to the laser wavelength ($\Lambda \approx \lambda$), a height in the range of a few hundreds of nanometers [9, 10] and a direction orthogonal to the polarization of the laser radiation. LSFLs can be obtained with continuous wave lasers [11] as well as pulsed lasers [5, 12] when several pulses are applied to the same location of the surface of the material [18, 22, 37, 39, 48, 49]. The number of pulses required to create LSFLs is low (less than 100) [18, 48, 49], but a higher number of pulses can

Table 2.1: Tabulated overview of the diffraction patterns, generated by LSFLs, observed by Van Driel and his coworkers [5, 43, 52, 53]. Here, "Pol" stands for polarization, "$\vec{p}$" for p-polarization, "$\vec{s}$" for s-polarization, "RC" for right-handed circular polarization and "LC" for left-handed circular polarization.

Pol / θ	$\vec{p}$ ↕	$\vec{s}$ ⟶	RC ↻	LC ↺
$\approx 0°$				
$\approx 30°$				
$\lesssim 45°$				
$\gtrsim 45°$		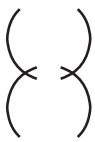		

also lead to their formation [22, 37, 39]. If the subsequent laser pulses are partially overlapping, instead of applied to the same location on the surface, LSFLs can also occur and extend over several laser spots [14, 28, 50]. The fluence regime, in which LSFLs grow, is close to the fluence threshold at which the material starts to ablate for a single pulse, referred to as single pulse ablation threshold [18, 39, 48, 49]. It is worth noting that the fluence applied also affects the height of LSFLs [51].

From the above-mentioned description, the properties of LSFLs can vary significantly. For example, the angle of incidence of the laser beam has a strong influence on the periodicity and orientation of LSFLs [4, 5, 43, 52–54]. Because the LIPSS patterns can be complex, a convenient way of studying the properties of LSFLs, as a function of the angle of incidence, is to characterize LSFLs in the frequency domain. A simple method to study LIPSSs in the frequency domain is to analyze the diffraction pattern produced by a coherent light source, usually a

continuous wave laser, reflected from the surface containing the LIPSSs [5]. This method has been used extensively by Van Driel and his coworkers [5, 43, 52, 53]. A summary of the diffraction patterns they observed is shown in Table 2.1.

For linearly polarized light at normal incidence of the laser beam, $\theta = 0\,^{\circ}$, the diffraction patterns show that LSFLs are not straight lines, which would be represented by "dots" in the frequency domain. For p-polarized laser radiation, two periodicities are observed in the direction orthogonal to the laser beam for $\theta \lesssim 45°$, while for larger angles of incidence, LIPSS patterns parallel to the polarization, represented by the two dots in the frequency domain, have been observed. These diffraction patterns match the SEM images of Young et al. [5]. The dependence of the periodicity of LIPSSs as a function of the angle of incidence is given by $\Lambda = \lambda/\left(1 \pm \sin\left(\theta\right)\right)$ for the two sets of ripples while $\Lambda = \lambda/\cos\left(\theta\right)$ describes the parallel pattern. For s-polarized laser radiation, the diffraction patterns reveal little variations for $\theta \lesssim 45°$. However, for larger angles of incidence, the LIPSS pattern is complex, neither parallel nor orthogonal to the polarization. The SEM observations revealed a periodicity $\Lambda = \lambda/\cos\left(\theta\right)$ for $\theta \leq 45\,^{\circ}$ [5]. Isotropic LIPSS patterns can be obtained when circular polarization is applied. As pointed out by Van Driel et al., it is remarkable that optical inactive materials are sensible to the sense of rotation of the circular polarized light [53].

At normal incidence of the laser beam, LSFLs can also show different characteristics. In several cases, the periodicity of LSFLs does not follow strictly the laser wavelength, as shown in Table 2.2. This characteristic has been observed mainly for ultra-short laser pulses and concerns all types of materials. It is worth noting that the periodicity of LSFLs decreases with increasing number of pulses applied and that the rate of this decrease is also material dependent [37, 39, 55]. It can be difficult to distinguish between LSFLs and HSFLs orthogonal to the polarization. Huang et al. proposed a value of 0.4 for the ratio Λ/λ as a boundary to discriminate HSFLs from LSFLs [37]. However, it is possible to observe LIPSSs with $\Lambda \approx 0.5\lambda$ progressively reaching $\Lambda \approx 0.31\lambda$ within the same laser track [28].

2.1.2 High spatial frequency laser-induced periodic surface structures

As stated in the introduction, HSFLs can be produced on metals [14–17], semiconductors [12, 18–23] and dielectrics [24–27]. They are defined as LIPSSs with a periodicity Λ significantly smaller than the laser wavelength λ ($\Lambda \ll \lambda$). On the contrary to LSFLs, HSFLs develop almost only for pulsed lasers, when the pulses applied are in the picosecond of femtosecond regime. Only a few studies mention HSFLs produced with nanosecond pulses [57, 59]. For linearly polarized light, HSFLs are oriented parallel [14, 17, 22, 23, 27] or orthogonal [12, 16, 18–21, 24–26] to the polarization of the laser light. Examples of periodicities and orientations of HSFLs produced by femtosecond irradiation are listed in Table 2.3. Both orientations, orthogonal or parallel to the laser polarization, have been observed for the different types of materials. The fluence regime in which HSFLs grow is below or close to the single pulse ablation threshold [12, 16, 18, 21, 22].

Table 2.2: Periodicity Λ of LSFLs compared to the wavelength λ of the laser radiation for various materials. In the referenced articles, LSFLs were produced under normal incidence ($\theta = 0°$) of the laser beam. The column "Type" specifies if a material is a metal M, a semiconductor S or a dielectric D. In the third column, the range of the pulse duration τ is indicated. Here, "ns" and "fs" denote nanosecond and femtosecond respectively.

Material	Type	τ	Periodicity Λ	Reference(s)
Si	S	ns	$\Lambda \approx 0.94\lambda$	[56]
Melted quartz	M	ns	$\Lambda \approx 0.71\lambda$	[57]
NaCl	D	ns	$\Lambda \approx 0.67\lambda$	[6]
TiN	M	fs	$\Lambda \approx 0.74\lambda$	[36]
Alloyed steel	M	fs	$\Lambda \approx 0.63\lambda$	[14]
Pt	M	fs	$0.66 \leq \Lambda/\lambda \leq 0.76$	[55]
InP	S	fs	$0.74 \leq \Lambda/\lambda \leq 0.94$	[12]
Si	S	fs	$0.7 \leq \Lambda/\lambda \leq 0.96$	[22, 38, 39, 58]
Diamond	D	fs	$\Lambda \approx 0.94\lambda$	[27]

Apart from the previously mentioned characteristics, it is difficult to define general properties of HSFLs, because of the large variety of observed features. For some materials, it was shown that the periodicity of HSFLs increases with increasing fluence [60, 61], while some materials do not follow such a relation [18, 21]. HSFLs have been observed to occur after only a dozen of pulses [12, 18, 36, 62], but some after hundreds of pulses [16, 63], thousands of pulses [24, 25, 27, 64] or even more (up to 120000 pulses)[22]. It was shown by Borowiec et al. that HSFLs occur easily when the one-photon transparency is achieved [18]. That is, when photons have an energy smaller than the band gap of the material. However, it is not a prerequisite for their formation [12, 22]. Depending on the material and on the processing conditions, the periodicity of HSFLs increases with the laser wavelength [16] or remains constant [25]. The same holds for the angle of incidence, i.e. HSFLs can be sensitive [21] or insensitive [25] to a variation of the angle of incidence. On the contrary to LSFLs, no systematic studies have been carried out to verify the influence of the polarization and the angle of incidence on the characteristics of HSFLs. In addition, it is known that

Table 2.3: Periodicity Λ and orientation of HSFLs compared to the wavelength λ and the polarization of the laser radiation respectively. In the referenced articles, HSFLs were produced under normal incidence ($\theta = 0°$) of the laser beam and femtosecond pulse duration. The column "Type" indicates if a material is a metal M, a semiconductor S or a dielectric D.

Material	Type	Orientation	Periodicity Λ	References
TiN	M	$\perp$	$\Lambda \approx 0.16\lambda$	[16]
Alloyed Steel	M	$\parallel$	$0.15 \leq \Lambda/\lambda \leq 0.24$	[14]
Ti	M	$\parallel$	$0.08 \leq \Lambda/\lambda \leq 0.12$	[17]
Si	S	$\parallel$	$\Lambda \approx 0.25\lambda$	[22]
InP	S	$\perp$	$\Lambda \approx 0.24\lambda$	[18]
ZnO	S	$\perp$	$0.25 \leq \Lambda/\lambda \leq 0.35$	[18]
Sapphire	D	$\perp$	$\Lambda \approx 0.34\lambda$	[18]
Diamond	D	$\parallel$	$\Lambda \approx 0.26\lambda$	[27]

circular polarized light can generate small bumps instead of HSFLs [16, 61]. Finally, the height of HSFLs can be as small as 10 nm [28, 29] or as big as 1 µm [10]. In the latter case, HSFLs have a large aspect ratio (height divided by the width), which increases with increasing applied fluence [10, 51].

2.1.3 Other kinds of laser-induced periodic surface structures

Only a few studies on the formation of LIPSSs with a periodicity larger than the laser wavelength ($\Lambda > \lambda$) are reported in literature. These LIPSSs, usually referred to as "grooves" [12], were observed on metals [40] and semiconductors [12, 39, 40, 50, 56]. Their orientation was found to be orthogonal [40] or parallel [12, 39, 40, 50, 56] to the polarization of the laser radiation. Huang et al. proposed grating coupling as an explanation for groove formation [40]. However, it is not clear why several groove directions are possible.

Yet another kind of LIPSSs with $\Lambda \ll \lambda$ and less directional than HSFLs, referred to as "fine bumps", were observed on silicon [29]. They were produced with rather large wavelengths (about 1300 nm and about 2100 nm) compared to the wavelength of experiments with $\lambda = 800$ nm, typical for fs lasers.

LIPSSs with $\Lambda \leq \lambda$, parallel to the polarization, are also reported in literature [65]. These LIPSSs were referred to as LSFLs by Höhm et al. However, the term "LSFLs" is only used when LIPSSs with $\Lambda \leq \lambda$ are orthogonal to the polarization in this thesis. It is worth noting that the periodicity of these LIPSSs parallel to the polarization was described more precisely than $\Lambda \leq \lambda$ as $\Lambda = \lambda/\mathrm{Re}(\tilde{n})$, where $\mathrm{Re}(\tilde{n})$ is the real part of the complex refractive $\tilde{n}$ of the material. Höhm et al. used the term "LSFLs" because $\mathrm{Re}(\tilde{n})$ is smaller than 2 in reference [65], which makes these LIPSSs fall in the category of LIPSSs with $\Lambda \leq \lambda$ rather than HSFLs.

2.2 Theories

2.2.1 Theories aimed at low spatial frequency laser-induced periodic surface structures

It is commonly accepted that LSFLs with $\Lambda \approx \lambda$ are triggered by the interaction of electromagnetic waves with rough surfaces [4, 6, 13, 54, 66]. Emmony et al. suggested the existence of a "surface-scattered wave", originating at a surface defect, interfering with the incident laser light [4]. While this simple concept is appealing, it has several inconsistencies [13] and several authors proposed a more accurate treatment of this problem [6, 13, 54, 66]. According to Clark et al. [67], "the most rigorous, comprehensive, and indeed the only (theory) that, to our knowledge, can accurately explain all of the observed LIPSSs is that in [13]". The theory presented in [13], usually referred to as the "Sipe theory", after its inventor John Sipe, is indeed able to account for the formation of LSFLs with $\Lambda \approx \lambda$ and their variations of periodicity and orientation as a function of θ. The Sipe theory predicts the inhomogeneous energy absorption of linearly polarized electromagnetic plane waves below the rough surface of materials. This prediction is made in the frequency domain and the results resemble the experimentally determined diffraction patterns shown in Table 2.1. It is assumed that the inhomogeneous energy absorption triggers LIPSS formation.

LSFLs with $\Lambda \leq \lambda$ have been observed and discussed extensively since the early 2000s [12, 14, 22, 27, 36–39, 55, 58], as it was shown in Table 2.2. Already in 1982, surface plasmon polaritons (SPPs) were proposed by Keilmann and Bai as an explanation for the periodicity of LSFLs being smaller than the laser wavelength [57]. SPPs are electromagnetic excitations propagating at the interface between a dielectric and an electrically conductive material [68]. They are the results of the coupling of surface plasmons (oscillations of the electron plasma of the conductors) with photons. As pointed out by Keilmann and Bai, SPPs can be excited from microscopic spatial disturbances. In the framework of this concept, LSFLs are induced by the interference of the incident laser light with SPPs. The reason why SPPs are a good candidate to explain LSFL formation is that they are transverse magnetic (TM) polarized and that their periodicity is smaller than the laser wavelength. Being TM polarized implies that interference pattern of SPPs with the incident laser light is orthogonal to the laser polarization, which coincides with the

orientation of LSFLs [57]. While the involvement of SPPs is known for metals [13, 57], it is more complex for semiconductors and dielectrics. It is proposed that under ultra-short laser irradiation [37, 58], the optical properties of semiconductors and dielectrics can turn metallic. This would allow the excitation of SPPs and their interference with the incident laser light. Several studies show a good match between the observed periodicities of LSFLs and the periodicities predicted by the SPPs/interference theory [37, 58, 69, 70]. It is worth noting that a careful investigation of the Sipe theory [13, 58, 69] reveals that the excitation of SPPs is included.

While SPPs can explain a periodicity Λ of LSFLs smaller than the laser wavelength ($\Lambda \leq \lambda$), it is unclear why Λ depends on the fluence and decreases with the number of pulses applied. Bonse and Krüger gathered three possible explanations [39]. Firstly, the periodicity of SPPs depends on the optical properties of materials [37, 58]. Since the optical properties can vary with the excited states of the material (number of electrons in the conduction band of semiconductors and dielectrics), different fluences lead to different optical properties. Hence, different periodicities of SPPs. Secondly, the periodicity of SPPs is affected by the presence of gratings, LSFLs in this case. According to Huang et al. [37], the grating like LSFLs deepens with the number of pulses applied and this deepening leads to a decrease of the phase velocity of SPPs [71]. Therefore, a decreased periodicity of the interference pattern. However, this scenario suggests that the whole surface region containing LSFLs melts and new LSFLs with a smaller periodicity form. It is in apparent disagreement with the cross-section study of Borowiec et al. [72], in which only a little resolidified layer of material is visible, mostly on top of LSFLs. Thirdly, LSFL periodicity is affected by the angle of incidence. When enough pulses have been applied to form an ablation "crater", the local angle of incidence on the "walls" of the crater can play a role.

As mentioned previously, the periodicity of LSFLs strongly depends on the interaction of electromagnetic waves with rough surfaces. However, other phenomena occur during laser processing , such as melting or ablation of the surface of the materials, which affect LIPSS formation. Young et al. [41] described different melting regimes, depending on the fluence applied, leading to LSFL formation for nanosecond laser pulses. At low fluence, the inhomogeneous absorption of energy can lead to melt periodically the materials and form LSFLs after solidification [41, 73, 74]. It is further suggested that for a higher fluence, LSFLs grow from a melt layer which solidifies at different speed depending on the inhomogeneous absorption. If the melt layer is thick enough, capillary waves can also play an important role [41]. For ultra-short laser pulses, such a study is missing in literature. LSFLs are observed when ablation occurs [25, 39, 49, 58], which forbids to transpose directly the knowledge gained for nanosecond pulses to ultra-short laser pulses. The analysis of cross-sections revealed that ablation is probably playing a key role in LSFL formation under ultra-short pulses irradiation [72]. Regardless of the responsible mechanisms for the transport of matter, feedback mechanisms are of importance for LIPSS growth [37, 39, 41]. As mentioned previously, the optical properties of the irradiated material change during the pulse which, in return, influences the energy absorption. This effect, referred to as intra-pulse

feedback [41], is necessary for the excitation of SPPs on semiconductors and dielectrics for example. The second kind of feedback mechanisms is referred to as inter-pulse feedback. It involves geometrical changes of the surface roughness between subsequent laser pulses. This changed roughness affects the energy absorption during the next laser pulse. Since LSFLs form after several pulses, inter-pulse feedback mechanisms are apparently crucial. The interaction of SPPs with gratings is a good example of such a feedback mechanism. Young et al. used the Sipe theory to explain qualitatively this mechanism [41].

2.2.2 Theories aimed at high spatial frequency laser-induced periodic surface structures

The origin of HSFL is still under debate and several theories have been proposed to account for their formation [18, 21, 22, 24, 27]. Based on the knowledge on LSFL formation, several authors proposed electromagnetic based explanations [18, 21, 27]. Second harmonic generation (SHG) was proposed as a cause of the strong decrease of periodicity compared to the wavelength of the laser radiation [18], however, SHG alone gave inconsistent results [18, 19]. As for LSFLs, it became clear that a change of the optical properties of the material during the laser pulse (intra-pulse feedback) is necessary to explain HSFL formation [19, 21, 27]. Dufft et al. [21] and Wu et al. [27] extended the Sipe theory thanks to estimated variations of the optical properties of materials and, in the case of Dufft et al., SHG to account for HSFL formation. Other electromagnetic explanations have been proposed, such as the existence of "nanoplasma bubbles" [75]. Despite all these attempts to extend existing theories, the formation of several HSFLs remained unexplained [17, 19, 24, 28, 44].

After observing several LIPSS patterns which were not following the classical electromagnetic predictions [22, 24, 25, 29, 64], Reif et al. proposed an alternative to the electromagnetic approach [76]. In this model, LIPSSs are the result of a self-organization process, triggered by ablation [22, 24]. This model accounts for many of the properties of LIPSSs observed, however, no direct relation between the periodicity of LIPSSs and the wavelength of the laser radiation could be predicted [76].

As for LSFLs, the exact mechanisms responsible for the transport of matter are still under investigation. Nonetheless, the investigation of cross-sections suggests that LSFLs and HSFLs form due to the same physical processes [51]. The columnar shapes and the high aspect ratios indicate a strong contribution of the ablation process [10, 51].

2.3 Conclusion

LIPSSs created with linearly polarized femtosecond laser radiation, under normal incidence of the laser beam, can be classified mainly into LSFLs and HSFLs. These two types of LIPSSs have two properties in common: their periodicities depend on the wavelength of the laser radiation and their directions depend on the polarization of the laser light. This strongly suggests that LIPSS formation can be understood in

Table 2.4: Periodicities and orientations of LIPSSs that a complete theory should be able to predict under normal incidence of the laser beam. LIPSSs can be orthogonal $\perp$ or parallel $\parallel$ to the laser beam polarization.

Periodicity Λ	Orientation
$\Lambda \leq \lambda$	$\perp$
$\Lambda = \lambda/\mathrm{Re}(\tilde{n})$	$\parallel$
$\Lambda \ll \lambda$	$\perp$, $\parallel$
$\Lambda > \lambda$	$\perp$, $\parallel$

the framework of an electromagnetic theory. Several models have been proposed in literature. However, none of the proposed models can account for all the observed LIPSSs and their various properties. In Table 2.4, the periodicities and orientations that a complete theory should account for are gathered. A complete theory should also explain the variation of periodicity Λ of LSFLs and a possible change of orientation from HSFLs to LSFLs, as observed in [14, 27].

From the theories mentioned above, the most promising approach to explain LIPSS formation is related to the Sipe theory. While not being able to account for all the observed phenomena, the Sipe theory includes the excitation of SPPs, which provides a good explanation to LSFL formation, and was extended to understand HSFLs in certain cases. Moreover, the effect of the angle of incidence on LSFLs with $\Lambda \approx \lambda$ was correctly simulated. In chapter 3, the Sipe theory is therefore described and analyzed to understand its strengths and its limitations.

Chapter 3

Strengths and limitations of the Sipe theory

The goal of this chapter is to discuss the Sipe theory. The general concept, including the notations, assumptions and outcome are presented first. Next, typical results of the Sipe theory are shown to identify the strengths and limitations of this model.

3.1 Background

The Sipe theory was published in 1983 by Sipe and his coworkers [13]. The goal of this theory is to explain LIPSS formation, and particularly LSFL formation since almost no HSFLs were observed before the 2000s. In the frame of this approach, LIPSSs are thought to be the fingerprints of the inhomogeneous absorption of the laser light below the rough surface of materials. To prove this assertion, Sipe et al. proposed a careful treatment of the interaction of electromagnetic waves with rough surfaces. The concept of the Sipe theory is shown in Figure 3.1. The incident laser radiation interacts with the rough surface, leading to an inhomogeneous energy absorption. The main outcome of the Sipe theory is the prediction of the distribution of the absorbed energy just below the rough surface of the material (dotted line). This prediction is made by solving Maxwell's equations analytically for a plane wave incident on the rough surface. These equations, as well as the resulting absorbed energy are calculated in the frequency domain. The spatial frequency spectrum, referred to as Sipe theory calculations in Figure 3.1, shows white sharp peaks indicating that the absorbed energy is periodic. Since LIPSSs are assumed to grow where the absorbed energy is the largest (represented by the radiating dots) in the Sipe theory, their formation follows the absorbed energy profile. Therefore, a Fourier transform of the height profile of a surface with LIPSSs is directly comparable to the absorbed energy below the rough surface. These Fourier transforms can be obtained by studying

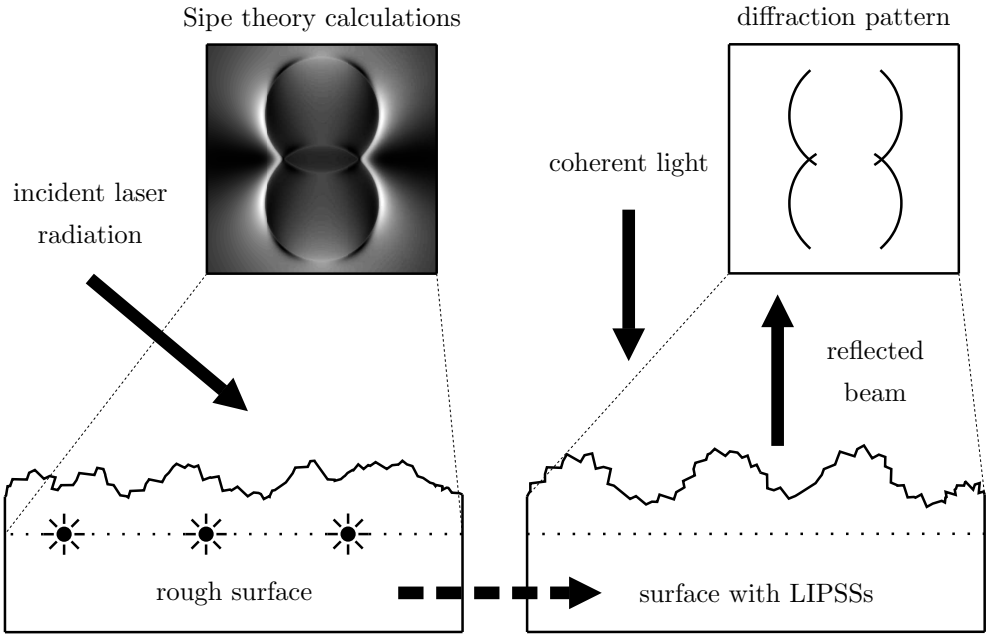

Figure 3.1: Concept of the Sipe theory. The radiating dots just below the rough surface symbolize the locations where the absorbed energy is the largest. The dashed arrow represents the assumption that LIPSS formation occur where the absorbed energy is the largest. The thin dashed lines indicate a frequency domain representation of the absorbed energy (Sipe theory calculations) and the height profile of the rough surface with LIPSSs (diffraction pattern).

diffraction patterns produced by a coherent light source, e.g. a continuous wave laser, reflected from a surface with LSFLs. As mentioned in section 2.1.1, this technique has been extensively used by Van Driel and his coworkers [5, 43, 52, 53], see Table 2.1 on page 7. Their aim was not only to study the effect of the angle of incidence θ on the characteristics of LSFLs, but also to validate the Sipe theory. In the following section, the notations, assumptions and the main outcome of the Sipe theory are presented.

3.2 Notations and assumptions

The geometrical configuration of the problem solved by the Sipe theory is shown in Figure 3.2. For $z > 0$, there is vacuum and a region of thickness l_s, referred to as the "selvedge", in which the surface roughness is confined. While, $z \leq 0$ is the bulk material which is assumed to be infinitely extended. Material properties in the

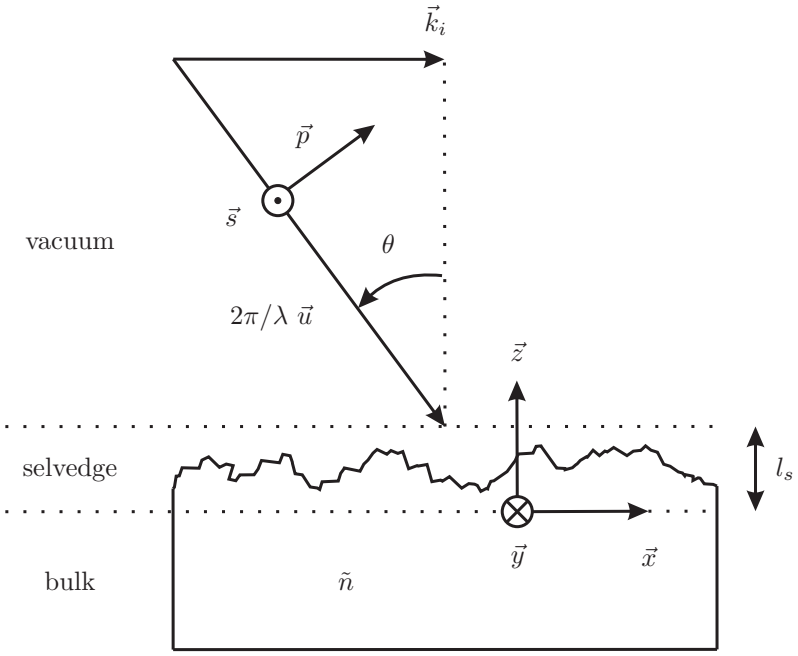

Figure 3.2: Geometry and notations used to describe the Sipe theory. A plane wave, s- (orthogonal to the $(\vec{x}, \vec{z})$ plane) or p- (parallel to the $(\vec{x}, \vec{z})$ plane) polarized, is incident on the rough surface of a material. Here, λ denotes again the wavelength of the incident laser radiation, θ the angle of incidence with respect to the normal to the surface, $2\pi/\lambda\ \vec{u}$ the wave vector of the incident plane wave, with $\vec{u}$ being a unit vector indicating the direction of propagation, $\vec{k}_i$ the component of the wave vector parallel to the $(\vec{x}, \vec{y})$ plane, l_s the selvedge thickness and $\tilde{n}$ the complex refractive index of the material.

bulk and in the selvedge (if there is material) are identical. The optical properties of the material are defined by the complex refractive index $\tilde{n}$, which is assumed to be constant. A plane wave of wavelength λ is incident on the selvedge region at an angle of incidence θ compared to the normal. This plane wave is polarized in a direction parallel (p-polarized) or orthogonal (s-polarized) to the plane of incidence $(\vec{x}, \vec{z})$ and is characterized by a wave vector $2\pi/\lambda\ \vec{u}$, where $\vec{u}$ is a unit vector indicating the direction of propagation. The component of the wave vector parallel to the surface, the $(\vec{x}, \vec{y})$ plane, is referred to as $\vec{k}_i$. The absorbed energy $A(\vec{k})$ is studied at $z = 0$ in the frequency domain, spanned by a vector $\vec{k} = (k_x, k_y)$ parallel to the surface. The Sipe theory predicts that the absorbed energy $A(\vec{k})$ is proportional to the frequency spectrum of the rough surface $b(\vec{k})$, weighted by a function $\eta(\vec{k}, \vec{k}_i)$. The latter is referred to as the efficacy factor. Hence,

$$A(\vec{k}) \propto \eta(\vec{k}, \vec{k}_i)|b(\vec{k})|. \tag{3.1}$$

In other words, $\eta(\vec{k}, \vec{k}_i)$ quantifies the efficacy with which the roughness leads to an inhomogeneous energy absorption at $\vec{k}$.

Only under certain conditions, relation (3.1) is valid and an expression of $\eta(\vec{k}, \vec{k}_i)$ can be derived. These conditions are presented before discussing the results of the Sipe theory. The thickness of the selvedge l_s must satisfy two inequalities. First, the selvedge thickness shall be small compared to the laser wavelength. That is,

$$\frac{2\pi}{\lambda} l_s \ll 1. \tag{3.2}$$

Second, the selvedge thickness shall be small compared to the periodicity of the inhomogeneous energy absorption. That is,

$$\|\vec{k}\| l_s \ll 1. \tag{3.3}$$

Moreover, Sipe et al. assumed a specific statistical roughness model to establish relation (3.1). That is, the roughness is described, in the space domain, as a binary function $b(x, y)$, as shown in Figure 3.3. That is, $b(x, y) = 0$ or 1 for the unfilled (vacuum) and filled parts of the selvedge, respectively. The efficacy factor is calculated for random rough surfaces, $b(x, y)$ being defined by two parameters: the filling factor F and the shape factor s. F and s are used to characterize $b(x, y)$ by the following set of equations,

$$\langle b(\vec{\rho}) \rangle = F, \tag{3.4}$$

$$\langle b(\vec{\rho}) b(\vec{\rho}\,') \rangle = F^2 + (F - F^2) C(\|\vec{\rho} - \vec{\rho}\,'\|), \tag{3.5}$$

$$C(\|\vec{\rho}\|) = \Theta(l_t - \|\vec{\rho}\|), \tag{3.6}$$

$$s = \frac{l_t}{l_s}. \tag{3.7}$$

$\langle \bullet \rangle$ and $\|\vec{\bullet}\|$ denote the ensemble average of $\bullet$ and the norm of $\vec{\bullet}$, respectively. Hence, F is the average of $b(\vec{\rho})$, where $\vec{\rho} = (x, y)$. Θ is the Heaviside, or unit, step function. The parameter l_t, and therefore s, characterizes how the filled part of the selvedge agglomerate through the expression $\langle b(\vec{\rho}) b(\vec{\rho}\,') \rangle$. Indeed, for points (x, y) and (x', y'), if $\|\vec{\rho} - \vec{\rho}\,'\| > l_t$ then $C(\|\vec{\rho} - \vec{\rho}\,'\|) = 0$ and $\langle b(\vec{\rho}) b(\vec{\rho}\,') \rangle = F^2$. Else, $\|\vec{\rho} - \vec{\rho}\,'\| \leq l_t$ and $\langle b(\vec{\rho}) b(\vec{\rho}\,') \rangle = F$. Since $F^2 \leq F$ $(F \leq 1)$, the filled parts of the selvedge tend to agglomerate and form "islands" of radii l_t . Therefore, s is comparable to half of the aspect ratio (the half width divided by the height) of the filled parts of the selvedge. According to Young et al., the best set (F, s) to describe LIPSSs in the Sipe theory equals $(0.1, 0.4)$ [5]. It is the set of parameters which matches the best their experimental results. That is, their SEM observations and the diffractions patterns presented in Table 2.1 on page 7. Moreover, "except for a factor independent of $\vec{k}$, in the case of s-polarized light the theory predicts no dependence of $\eta(\vec{k})$ on s and F" [5]. Thus, in the case of a study at normal incidence $\theta = 0$, the ratios between the different

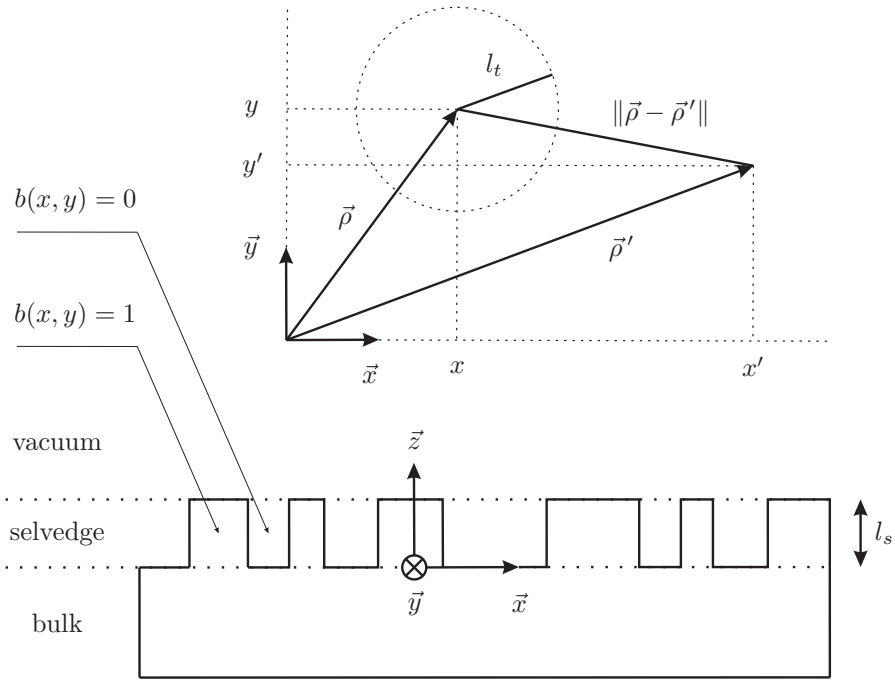

Figure 3.3: Roughness model of the surface as part of the Sipe theory.

frequencies of $\eta(\vec{k})$ are independent of s and F. This is an important property of the model since a study at normal incidence involves no "fitting" parameters.

3.3 Efficacy factor maps

Once all the conditions described previously are fulfilled, relation (3.1) is valid and $\eta(\vec{k}, \vec{k}_i)$ is given by equation (3.8) [13],

$$\eta(\vec{k}, \vec{k}_i) = 2\pi|\upsilon(\vec{k}_+) + \bar{\upsilon}(\vec{k}_-)|, \tag{3.8}$$

where $\vec{k}_\pm = \vec{k}_i \pm \vec{k}$. The operators $|\bullet|$ and $\bar{\bullet}$ represent the absolute value and the complex conjugate of $\bullet$, respectively. For s-polarized light, $\upsilon(\vec{k}_\pm)$ is given by

$$\upsilon(\vec{k}_\pm) = [h_{ss}(k_\pm)(\hat{k}_\pm \cdot \vec{x})^2 + h_{kk}(k_\pm)(\hat{k}_\pm \cdot \vec{y})^2]\gamma_t|t_s(\vec{k}_i)|^2, \tag{3.9}$$

while for p-polarized light, $\upsilon(\vec{k}_\pm)$ is given by

$$\begin{aligned} \upsilon(\vec{k}_\pm) =& [h_{ss}(k_\pm)(\hat{k}_\pm \cdot \vec{y})^2 + h_{kk}(k_\pm)(\hat{k}_\pm \cdot \vec{x})^2]\gamma_t |t_x(\vec{k}_i)|^2 \\ &+ h_{kz}(k_\pm)(\hat{k}_\pm \cdot \vec{x})\gamma_z \tilde{\varepsilon} \bar{t}_x t_z \\ &+ h_{zk}(k_\pm)(\hat{k}_\pm \cdot \vec{x})\gamma_t \bar{t}_z t_x \\ &+ h_{zz}(k_\pm)\gamma_z \tilde{\varepsilon} |t_z|^2. \end{aligned} \tag{3.10}$$

Here, $\vec{\bullet} \cdot \vec{\bullet}$ denotes the scalar product and $\hat{\bullet}$ a normalized vector. That is, $\hat{\bullet} = \vec{\bullet}/\|\vec{\bullet}\|$. Further, $k_\pm$ and ν represent the norm of vector $\vec{k}_\pm$, $\|\vec{k}_\pm\|$ and the norm of the wave vector $2\pi/\lambda\ \vec{u}$, $2\pi/\lambda$, respectively. $\tilde{\varepsilon} = \tilde{n}^2$ is the complex permittivity of the material. Finally, the functions $h(k_\pm)$ are defined by

$$h_{ss}(k_\pm) = \frac{2j\nu}{\sqrt{\nu^2 - k_\pm^2} + \sqrt{\nu^2\tilde{\varepsilon} - k_\pm^2}}, \tag{3.11}$$

$$h_{kk}(k_\pm) = \frac{2j}{\nu} \frac{\sqrt{\nu^2 - k_\pm^2}\sqrt{\nu^2\tilde{\varepsilon} - k_\pm^2}}{\tilde{\varepsilon}\sqrt{\nu^2 - k_\pm^2} + \sqrt{\nu^2\tilde{\varepsilon} - k_\pm^2}}, \tag{3.12}$$

$$h_{zz}(k_\pm) = \frac{2jk_\pm^2}{\tilde{\varepsilon}\sqrt{\nu^2 - k_\pm^2} + \sqrt{\nu^2\tilde{\varepsilon} - k_\pm^2}}, \tag{3.13}$$

$$h_{zk}(k_\pm) = \frac{2jk_\pm}{\nu} \frac{\sqrt{\nu^2 - k_\pm^2}}{\tilde{\varepsilon}\sqrt{\nu^2 - k_\pm^2} + \sqrt{\nu^2\tilde{\varepsilon} - k_\pm^2}}, \tag{3.14}$$

$$h_{kz}(k_\pm) = \frac{2jk_\pm}{\nu} \frac{\sqrt{\nu^2\tilde{\varepsilon} - k_\pm^2}}{\tilde{\varepsilon}\sqrt{\nu^2 - k_\pm^2} + \sqrt{\nu^2\tilde{\varepsilon} - k_\pm^2}}, \tag{3.15}$$

the functions $t(k_i)$ by

$$t_s(k_i) = \frac{2\sqrt{\nu^2 - k_i^2}}{\sqrt{\nu^2 - k_i^2} + \sqrt{\nu^2\tilde{\varepsilon} - k_i^2}}, \tag{3.16}$$

$$t_x(k_i) = \frac{2}{\nu} \frac{\sqrt{\nu^2 - k_i^2}\sqrt{\nu^2\tilde{\varepsilon} - k_i^2}}{\tilde{\varepsilon}\sqrt{\nu^2 - k_i^2} + \sqrt{\nu^2\tilde{\varepsilon} - k_i^2}}, \tag{3.17}$$

$$t_z(k_i) = \frac{2}{\nu} \frac{k_i\sqrt{\nu^2\tilde{\varepsilon} - k_i^2}}{\tilde{\varepsilon}\sqrt{\nu^2 - k_i^2} + \sqrt{\nu^2\tilde{\varepsilon} - k_i^2}}, \tag{3.18}$$

and the functions $\gamma(F, s)$ by

$$\gamma_z(F,s) = \frac{1}{4\pi}\frac{\tilde{\varepsilon}-1}{\tilde{\varepsilon}-(1-F)(\tilde{\varepsilon}-1)(h(s)+Rh_i(s))}, \tag{3.19}$$

$$\gamma_t(F,s) = \frac{1}{4\pi}\frac{\tilde{\varepsilon}-1}{1+\frac{1}{2}(1-F)(\tilde{\varepsilon}-1)(h(s)-Rh_i(s))}, \tag{3.20}$$

$$R = \frac{\tilde{\varepsilon}-1}{\tilde{\varepsilon}+1}, \tag{3.21}$$

$$h(s) = (s^2+1)^{\frac{1}{2}} - s, \tag{3.22}$$

$$h_I(s) = \frac{1}{2}[(s^2+4)^{\frac{1}{2}} + s] - (s^2+1)^{\frac{1}{2}}. \tag{3.23}$$

Thanks to equations (3.8) to (3.23), $\eta(\vec{k},\vec{k}_i)$ can be calculated. Examples of $\eta(\vec{k},\vec{k}_i)$ functions, also referred to as "efficacy factor maps" or "η maps" in this thesis, are shown in Figure 3.4. The η maps shown have been calculated with the following parameters:

- the wavelength of the incident laser radiation $\lambda = 800$ nm,
- the angle of incidence $\theta = 0$ (normal incidence),
- the set $(F,s) = (0.1, 0.4)$, as proposed by Young et al. [5],
- the optical properties of (a) gold $\tilde{n} = 0.181 + 5.1178j$ and (b) silicon $\tilde{n} = 3.692 + 0.0065j$ at room temperature [77].

The η maps are represented with a linear grayscale colormap. The white areas correspond to the largest values of $\eta(\vec{k},\vec{k}_i)$. The white arrows indicate the polarization direction of the laser radiation. The vector $\vec{k} = (k_x, k_y)$, spanning the frequency domain in the $(\vec{x},\vec{y})$ plane shown in Figure 3.2, is normalized by the norm of the wave vector, $2\pi/\lambda$. The main advantage of such a normalization is that it allows to relate the frequency domain directly to the wavelength of the laser radiation. For example, any point on the $\|\vec{k}\| = 1$ circle in the frequency domain corresponds to a periodicity $\Lambda = \lambda$ in the space domain. Likewise, any point inside the $\|\vec{k}\| < 1$ disk corresponds to a periodicity $\Lambda > \lambda$ in the space domain and any point outside the $\|\vec{k}\| < 1$ disk corresponds to a periodicity $\Lambda < \lambda$ in the space domain. Recalling equation (3.1), a large value of $\eta(\vec{k},\vec{k}_i)$ implies that the frequency component $b(\vec{k})$ of the rough surface spectrum leads to a strong energy absorption $A(\vec{k})$ at that location. Since $b(x,y)$ is expected to have a wide range of frequency components $b(\vec{k})$, and $b(\vec{k})$ to be a slowly varying function of $\vec{k}$ [5, 13], $A(\vec{k})$ and $\eta(\vec{k},\vec{k}_i)$ are almost linearly related. Hence, sharps peaks in η maps, i.e. high values of $\eta(\vec{k},\vec{k}_i)$, correspond to a strong energy absorption $A(\vec{k})$ at $\vec{k}$.

In Figure 3.4(a), the η map, which was computed for the optical properties of gold, shows one kind of features. The vertical and horizontal dotted lines indicate $k_x = \pm 1$ and $k_y = \pm 1$, respectively. The bright features, which are on the $\|\vec{k}\| = 1$

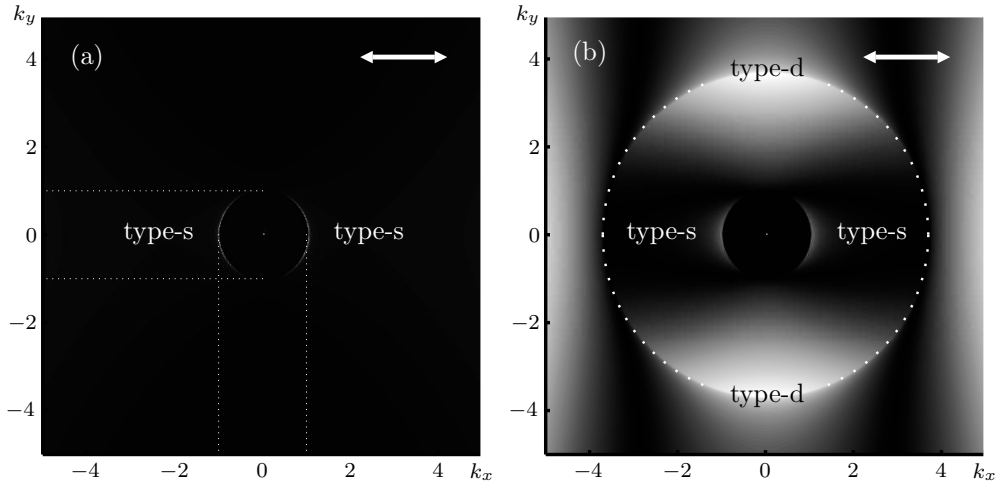

Figure 3.4: η maps computed for $\theta = 0$, $\lambda = 800$ nm, $(F, s) = (0.1, 0.4)$, (a) gold $\tilde{n} = 0.181 + 5.1178j$ and (b) silicon $\tilde{n} = 3.692 + 0.0065j$. The polarization direction is indicated by the white arrows. A linear grayscale colormap is used, in which the white areas correspond to the largest values.

circle, are interrupted at the lower and upper part of the circle. That is, there are two "crescents" which show a preferential direction along the k_x axis. Hence, these correspond to a periodic absorbed energy in the $\vec{x}$ direction, with a periodicity of $\Lambda \approx \lambda$ in the space domain. It is worth noting that the absorbed energy profile does not correspond to perfectly straight lines in the space domain, which would be represented by single dots in the frequency domain. Hence, it is likely to find bifurcations in the space domain. As shown by Young et al. [5], these features are responsible for the growth of LSFLs with a periodicity close to the laser wavelength ($\Lambda \approx \lambda$) and a direction orthogonal to the polarization of the laser radiation. For the sake of clarity, the terms HSFLs and LSFLs are only used to refer to LIPSSs in the space domain in this thesis. Therefore, another notation is used to refer to LIPSSs (or their associated features in the η maps) in the frequency domain. The features presented in Figure 3.4(a) are referred to as type-s in this thesis. This notation has been chosen in accordance with the description proposed by Young et al. [5]. The terms s^+ and s^- were used to refer to LIPSSs produced at off-normal incidence of the laser beam, associated with the type-s features presented here. No specific meaning was associated to the s^+ or s^- notations. Regarding the physical interpretation of type-s features, they are the fingerprints of SPPs when the complex refractive index $\tilde{n}$ fulfills the inequality $\mathrm{Re}(\tilde{n}) < \mathrm{Im}(\tilde{n})$ [13, 78]. As mentioned in section 2.2.1, SPPs, hence type-s features, have been studied extensively to explain LSFL characteristics, especially their periodicity slightly smaller than the laser wavelength ($\Lambda \leq \lambda$).

In Figure 3.4(b), two features need special attention: the type-s features mentioned previously and additional features close to the $\|\vec{k}\| = \mathrm{Re}(\tilde{n})$ dotted circle. These

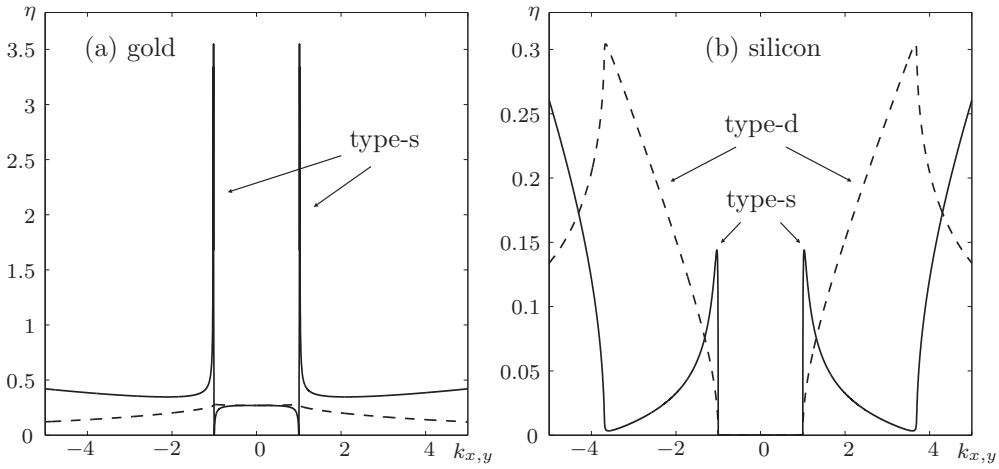

Figure 3.5: Cross-sections of the η maps presented in Figure 3.4. (a) and (b) are related to Figure 3.4(a) and Figure 3.4(b), respectively. The solid lines are cross-sections along $\vec{k}_x$ through $(0, 0)$ while the dashed lines are cross-sections along $\vec{k}_y$ through $(0, 0)$.

features are referred to as type-d features. The "d" stands for "dissident". This word was chosen because the type-d features do not follow the $\|\vec{k}\| = 1$ circle like the type-s, which correspond to the most common ripples. Indeed, LIPSSs in the space domain matching the type-d periodicities have not been observed frequently before the use of femtosecond lasers in experimental study of LIPSSs. Since $\vec{k}$ is normalized by $2\pi/\lambda$, the maxima of the type-d features correspond to a periodicity $\lambda/\mathrm{Re}(\tilde{n})$ of the absorbed energy in the space domain. Moreover, type-d features correspond to a periodic absorbed energy in the $\vec{k}_y$ direction. That is, HSFLs parallel to the laser polarization. In comparison to type-s features, the type-d features have rarely been investigated [21, 27]. Sipe et al. mentioned that it was difficult to observe LIPSSs related to the type-d features experimentally [78]. Interestingly, the type-s features present in Figure 3.4(b) are more spread than in Figure 3.4(a), leading to more variation of periodicity in the space domain. Both type-s and type-d features presented in Figure 3.4(b) are referred to as "radiation remnants" [13, 78]. That is, features of the η maps which are not related to SPPs. It is worth noting that, since $\mathrm{Re}(\tilde{n}) > \mathrm{Im}(\tilde{n})$, the type-s features are not related to SPPs in Figure 3.4(b). A detailed mathematical study of radiation remnants, including a comparison to SPPs, is available in [78].

As an alternative to the 2D representation of the efficacy factor in Figure 3.4, Figure 3.5 shows cross-sections of the η maps. Figure 3.5(a) and Figure 3.5(b) are related to Figure 3.4(a) and Figure 3.4(b), respectively. The solid lines are cross-sections along $\vec{k}_x$ through $(0, 0)$ while the dashed lines are cross-sections along $\vec{k}_y$ through $(0, 0)$. As mentioned previously, the type-s features are the dominant

frequencies in the case of gold, while they are more spread in the case of silicon. It is worth noting that the magnitude of the η maps for gold and silicon cannot be compared since relation (3.1) involves only a proportionality. Interestingly, the solid line in Figure 3.5(b) decreases from the maximum of the type-s feature ($k_x = 1$) until it reaches $k_x = \mathrm{Re}(\tilde{n}) = 3.692$, from where it increases rapidly. This effect is also observed in Figure 3.4(b) and is a limitation of the Sipe theory, as explained in the following part.

3.4 Strengths and limitations

In this section, the strengths of the Sipe theory are discussed first. Then, the limitations of the Sipe theory are analyzed with respect to the assumptions and the results presented in section 3.2 and section 3.3.

3.4.1 Strengths

Several strengths of the Sipe theory were already mentioned in chapter 2, which concern mainly the type-s features. That is, the Sipe theory is able to account for the periodicity and orientation of LSFLs for different angles of incidence θ. This was proven thanks to the diffraction patterns study of Van Driel and his coworkers [5, 43, 52, 53]. Moreover, the rigorous treatment of Maxwell's equations lead to the direct inclusion of SPPs in the model, while the presence of a "surface scattered wave" does not need to be assumed, in contrast to the model of Emmony et al. [4]. This is of importance since SPPs are playing a key role in LSFL formation [37, 58]. Besides the type-s features, a strong advantage of the Sipe theory lays in the type-d features. These features offer the possibility to explain the existence of HSFLs parallel to the polarization as was proposed by Wu et al. [27], as well as the existence of LIPSSs with $\Lambda = \lambda/\mathrm{Re}(\tilde{n})$, parallel to the polarization [65]. It is worth noting that the distinction between HSFLs parallel to the polarization and LIPSSs with $\Lambda = \lambda/\mathrm{Re}(\tilde{n})$, parallel to the polarization, is only a terminological issue here. This distinction is not recalled in the rest of this thesis.

An important extension which strengthen the validity of the Sipe theory was proposed by Bonse, Dufft and their coworkers [21, 58]. They coupled the Sipe theory to a Drude model, which estimates the optical properties of excited materials such as zinc oxide [21] and silicon [58]. Indeed, the optical properties of materials change during a laser pulse which can lead to variations of the absorbed energy profile. This effect is referred to as intra-pulse feedback and is taken into account by calculating η maps for different values of the complex refractive index $\tilde{n}$ predicted by the Drude model. In addition, the extended model allows η maps to be calculated with half of the wavelength and adapted optical properties to account qualitatively for second-harmonic generation [21].

Besides intra-pulse feedback, inter-pulse feedback mechanisms can be understood qualitatively in the frame of the Sipe theory [5]. The function $b(\vec{k})$ is expected to be a slowly varying function of $\vec{k}$ for a surface with homogeneously distributed

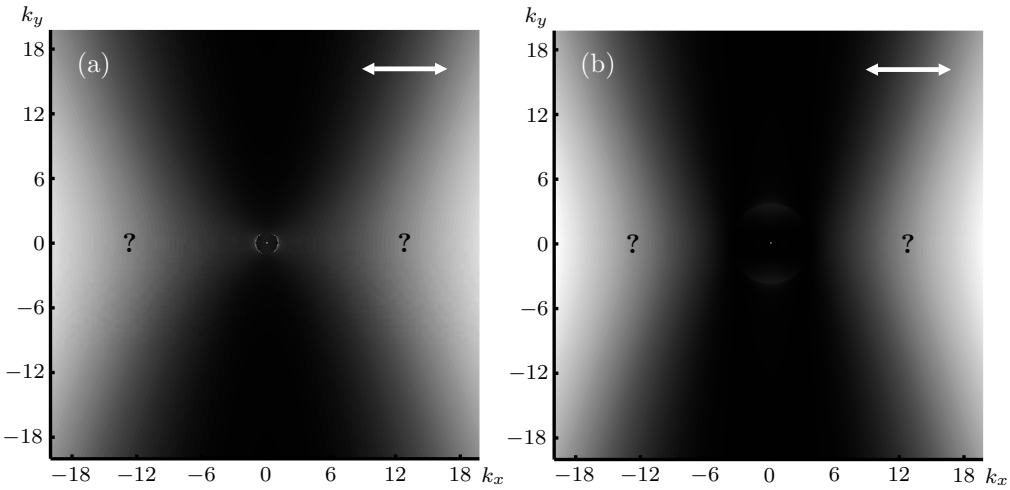

Figure 3.6: Same η map as in Figure 3.4 but shown for larger values of k_x and k_y. The polarization direction is indicated by the white arrows. A linear grayscale colormap is used, in which the white areas correspond to the largest values of $\eta(\vec{k}, \vec{k}_i)$.

roughness [13], while $\eta(\vec{k}, \vec{k}_i)$ has sharp peaks. The latter implies that if the laser fluence exceeds a certain threshold, localized melting is triggered at locations where the inhomogeneous energy input is the largest (peaks of $\eta(\vec{k}, \vec{k}_i)$) and LIPSS start to grow according to $A(\vec{k})$. Mathematically, the function $b(\vec{k})$ increases at $\vec{k}$ in accordance with the peaks of $\eta(\vec{k}, \vec{k}_i)$, enhancing the inhomogeneous energy absorption via equation (3.1) and the LIPSS formation. This qualitative feedback effect underlines that the driving function in LIPSS formation is $\eta(\vec{k}, \vec{k}_i)$.

3.4.2 Limitations

As mentioned previously, Figure 3.4(b) and Figure 3.5(b) exhibit a peculiar phenomenon. That is, the solid line in Figure 3.5(b) decreases from the maximum of the type-s feature ($k_x = 1$) until it reaches $k_x = \mathrm{Re}(\tilde{n})$, from where it increases rapidly. In Figure 3.6, η maps shown with the same conditions as in Figure 3.4, but for larger values of k_x and k_y. In the center of these larger η maps, type-s and type-d features are hardly visible but are present nonetheless. The η maps are dominated by broad white areas present at large values of k_x. This region of the η maps is of importance. Indeed, if HSFLs orthogonal to the polarization are a consequence of the interaction of electromagnetic waves with rough surfaces, the η maps should show a preferential energy absorption for large values of k_x. However, inequality (3.3) is not valid for large values of k_x, therefore no conclusions may be drawn concerning the implication of these features in the space domain.

A further limitation of the Sipe theory lies in inequality (3.2), which confines the

approach to a small selvedge thickness compared to the laser wavelength λ. This is problematic because LIPSSs may have heights comparable to λ, as mentioned in chapter 1 and 2. Moreover, due to the definition of the roughness function $b(x, y)$, the Sipe theory only applies to simple isotropic rough surfaces. Therefore, a surface which contains LIPSSs to start with is out of the scope of the Sipe theory.

A third limitation of the Sipe theory is that it calculates $\eta(\vec{k}, \vec{k}_i)$ for a plane just below the rough surface only. Hence, it does not allow a study of the η maps as a function of the depth in the bulk of the material.

One of the most severe limitations of the Sipe theory is that it does not allow a space domain investigation of $A(x, y)$. Indeed, equation (3.1) gives information about the amplitude of the absorbed energy spectrum but not about its phase. Thus, it is not possible to go from the frequency domain to the space domain by inverse Fourier transformation. The reason for this lack of information about the phase is that the η maps are calculated for the roughness functions $b(x, y)$ which are known only statistically. Figure 3.4(b) is a good example to show the importance of having space domain results. From this Figure, it is hard to determine which of the type-s or type-d features are the most pronounced in the space domain. Therefore it is difficult to predict which kind of LIPSSs will be found experimentally. Moreover, the frequencies contained in the broad white areas present at large values of k_x in Figure 3.6 have an unknown impact on the space domain.

Finally, a last limitation of the Sipe theory discussed here is its inability to account for low frequencies ($||\vec{k}|| < 1$), even though LIPSSs with a periodicity above the laser wavelength have been reported [12, 39, 40, 50, 56]. There is no clear reason why those frequencies are not found following the Sipe theory. It can be due to one or several drawbacks discussed above. For example, grooves discussed in section 2.1.3 are appearing on materials after a significant number of pulses. Hence, to investigate the initiation and growth of grooves, a correct incorporation of inter-pulse feedback mechanisms in the model would be required. Moreover, grooves form where ripples were present first, which cannot be modeled due to inequality (3.2).

3.5 Conclusion

The Sipe theory offers several answers to the initiation and growth of LIPSSs, via a careful treatment of the interaction of electromagnetic waves with rough surfaces. As shown in Table 3.1, type-s features can account for the formation of LSFLs while type-d features concern HSFL formation parallel to the polarization of the laser light. However, the approximations and assumptions made by Sipe et al. in the derivation of the efficacy factor function, do not allow to draw conclusions whether HSFLs orthogonal to the laser polarization are the result of the interaction of electromagnetic waves with rough surfaces (question mark in Table 3.1). Moreover, LIPSSs with $\Lambda > \lambda$, i.e. grooves, are not predicted in the framework of the Sipe theory.

In chapter 4 a numerical approach, the finite-difference time domain method, is presented. It allows to study the interaction of electromagnetic waves with rough surfaces. The goal is to overcome some of the limitations of the Sipe theory.

Table 3.1: Characteristics of LIPSSs (periodicity Λ and orientation) which can ($\surd$) and cannot ($\times$) be predicted by the Sipe theory under normal incidence of a laser beam.

Periodicity Λ	Orientation	Sipe theory
$\Lambda \leq \lambda$	$\perp$	$\surd$
$\Lambda = \lambda/\mathrm{Re}(\tilde{n})$	$\parallel$	$\surd$
$\Lambda \ll \lambda$	$\perp$	**?**
$\Lambda > \lambda$	$\perp$, $\parallel$	$\times$

Chapter 4

Numerical approach: the finite-difference time-domain method

This chapter is dedicated to the finite-difference time-domain method. The theoretical background required to discretize Maxwell's equations is discussed first. Next, the general concept of the finite-difference time-domain method and the assumptions made in the framework of this thesis are presented.

4.1 Introduction

As discussed in chapter 3, the Sipe theory has several limitations which can be overcome by solving Maxwell's equations numerically, rather than analytically. For that purpose, the finite-difference time-domain (FDTD) method has been selected. This method was introduced by Yee in 1966 [79], but the term "finite-difference time-domain" and its acronym "FDTD" was employed for the first time by Taflove in 1980 [80]. The original algorithm proposed by Yee is based on the two coupled Maxwell's curl equations, which are solved numerically in the time domain, using finite differences. While the concept of the FDTD method is relatively old, FDTD calculations gained popularity in the 1990s thanks to the increase of computational power. In this thesis, the FDTD method has been selected because it is accurate and robust. That is, "the sources of error in FDTD calculations are well understood, and can be bounded to permit accurate models for a very large variety of electromagnetic problems" [42]. Moreover, the FDTD method is a systematic approach, meaning that it is easy to investigate new geometries [42]. Regarding other common computational electromagnetic methods, the method of moments (MoM) and the finite element method (FEM), the FDTD method has been preferred

for two reasons in the framework of this thesis. First, the MoM is known to handle electromagnetically penetrable materials poorly in comparison to the FEM or the FDTD method [81]. This is a strong drawback since semiconductors and dielectrics are of interest in this thesis. Secondly, "it (the FDTD method) is the only method which one can realistically implement oneself in a reasonable timeframe" [81].

As mentioned previously, the FDTD method is based on the two coupled Maxwell's curl equations. Therefore, in section 4.2, the theoretical background of FDTD calculations is presented. Next, the FDTD algorithm is discussed in section 4.3, along with the boundary conditions relevant to simulate the interaction of electromagnetic waves with rough surfaces.

4.2 Theoretical background

In this section, the Maxwell's equations and the constitutive relations, linking the electromagnetic field and the response of the material, are presented. Assumptions are made regarding the constitutive relations, leading to a set of equations which is ready to be discretized by the FDTD method.

4.2.1 Maxwell's equations

In the absence of external charges and currents, the macroscopic set of Maxwell's equations in differential form can be expressed by equations (4.1a) to (4.1d) [82].

Gauss' law for the electric field:

$$\vec{\nabla} \cdot \vec{D} = 0, \tag{4.1a}$$

Gauss' law for the magnetic field:

$$\vec{\nabla} \cdot \vec{B} = 0, \tag{4.1b}$$

Ampere's law:

$$\frac{\partial \vec{D}}{\partial t} - \vec{\nabla} \times \vec{H} = 0, \tag{4.1c}$$

Faraday's law:

$$\frac{\partial \vec{B}}{\partial t} + \vec{\nabla} \times \vec{E} = 0. \tag{4.1d}$$

Here, $\vec{D}$ denotes the electric flux density, $\vec{E}$ the electric field, $\vec{B}$ the magnetic flux density and $\vec{H}$ the magnetic field. Further, $\partial\vec{\bullet}/\partial t$ denotes the partial derivative of $\vec{\bullet}$

with respect to time t. $\vec{\nabla} \cdot \vec{\bullet}$ and $\vec{\nabla} \times \vec{\bullet}$ are the divergence and the rotational (also referred to as curl operator) of $\vec{\bullet}$, respectively. In this set of equations, the response of the material to an electromagnetic excitation is not described. This is provided by the constitutive relations.

4.2.2 Constitutive relations

The four fields are linked through the following constitutive relations

$$\vec{D} = \varepsilon_0 \vec{E} + \vec{P}, \tag{4.2}$$

$$\vec{H} = \frac{1}{\mu_0} \vec{B} - \vec{M}, \tag{4.3}$$

where ε_0 and μ_0 are the permittivity and the permeability of vacuum respectively. Here, $\vec{P}$ is referred to as the polarization and is defined as the dipole moment per unit volume inside the material. It describes the alignment of microscopic dipoles in the presence of electric fields [68]. Finally, $\vec{M}$ is referred to as the magnetization and is defined as the magnetic moment per unit volume. It describes the effect of a material on the magnetic field. In this thesis, only non-magnetic media are considered. That is, $\vec{M} = 0$ and then equation (4.3) reduces to

$$\vec{H} = \mu_0^{-1} \vec{B}. \tag{4.4}$$

This is not a limitation since most of the materials on which LIPSSs were observed are non-magnetic, as shown in chapter 2.

To solve Maxwell's equations, it is required to define the reaction of materials $\vec{P}$ to electromagnetic excitations. As in the Sipe theory [13], materials are assumed to be linear and isotropic. The most general relation between $\vec{P}$ and $\vec{E}$ for linear isotropic media is given by

$$\vec{P}(\vec{r}, t) = \varepsilon_0 \int \chi(\vec{r} - \vec{r}', t - t') \vec{E}(\vec{r}', t') dt' d\vec{r}', \tag{4.5}$$

where χ is a scalar function referred to as the dielectric susceptibility. Equation (4.5) accounts for the non-locality in time and space of the response of a medium. The response can be assumed to be local in space if the wavelength in the medium is significantly longer than all characteristic dimensions such as the size of the unit cell or the mean free path of the electrons [68]. It is assumed in this work that the response is always local in space. Hence, $\chi(\vec{r}, t) = \chi(t)\delta(\vec{r})$, where δ is the Dirac delta function, and equation (4.5) reduces to

$$\vec{P}(\vec{r}, t) = \varepsilon_0 \int \chi(t - t') \vec{E}(\vec{r}, t') dt'. \tag{4.6}$$

4.2.3 Plane wave decomposition

Equation (4.6) can be simplified by applying the Fourier transform

$$\tilde{f}\left(\vec{\kappa},\omega\right)=\int\int f\left(\vec{r},t\right)e^{j(\omega t-\vec{\kappa}\cdot\vec{r})}d\vec{r}dt. \tag{4.7}$$

That is, the fields are decomposed into plane waves of wave vector $\vec{\kappa}$ and angular frequency ω [68]. One advantage of applying Fourier transformations is to turn convolutions into products. Hence, equation (4.6) becomes equation (4.8) in the frequency domain.

$$\tilde{P}(\vec{\kappa},\omega)=\varepsilon_0\tilde{\chi}(\omega)\tilde{E}(\vec{\kappa},\omega). \tag{4.8}$$

Due to the linearity of Maxwell's equations, it is also possible to decompose equations (4.1a) to (4.1d) without losing generality since the inverse Fourier transform,

$$f\left(\vec{r},t\right)=\int\int\tilde{f}\left(\vec{\kappa},\omega\right)e^{j(\vec{\kappa}\cdot\vec{r}-\omega t)}d\vec{r}dt, \tag{4.9}$$

allows to go backward. It is worth noting that $\tilde{\bullet}$ is used to refer to the Fourier transform of $\bullet$. In the case of a vector $\vec{\bullet}$, the Fourier transform should be denoted as $\tilde{\vec{\bullet}}$, but $\tilde{\bullet}$ is used for simplicity. $\tilde{\bullet}$ are in general complex functions, therefore the $\tilde{\bullet}$ notation is not only used to refer to Fourier transforms in this thesis, but also to indicate that scalar values are complex.

The Fourier transform has also other properties which are exploited in this thesis. For example, the Fourier transform of a derivative $\partial\vec{\bullet}/\partial t$ becomes the product of $-j\omega$ with $\tilde{\bullet}$,

$$\frac{\partial\vec{\bullet}}{\partial t}\Longleftrightarrow-j\omega\tilde{\bullet}. \tag{4.10}$$

This is easily proven by performing an integration by parts on relation (4.7). Similarly, the Fourier transform of a rotational $\vec{\nabla}\times\vec{\bullet}$ can be expressed as the cross product of $j\vec{\kappa}$ with $\tilde{\bullet}$,

$$\vec{\nabla}\times\vec{\bullet}\Longleftrightarrow j\vec{\kappa}\times\tilde{\bullet}. \tag{4.11}$$

4.2.4 Linear isotropic non-dispersive media

For linear and isotropic media that exhibit a local response in space, the relation between $\vec{P}$ and $\vec{E}$ is given by equation (4.8) in the frequency domain. Then, if the medium is assumed to be non-dispersive, as in the Sipe theory, $\tilde{\chi}(\omega)$ is constant and (4.8) reduces to

$$\tilde{P}(\vec{\kappa},\omega)=\varepsilon_0\tilde{\chi}\tilde{E}(\vec{\kappa},\omega). \tag{4.12}$$

Introducing $\tilde{\varepsilon}_r=1+\tilde{\chi}$, referred to as the complex relative permittivity, equation (4.2) can be written as

$$\tilde{D}(\vec{\kappa},\omega) = \varepsilon_0 \tilde{\varepsilon}_r \tilde{E}(\vec{\kappa},\omega). \tag{4.13}$$

Equation (4.13) is the simplest form of the constitutive relation for a linear, isotropic, non-dispersive medium that exhibits a local response in space. Substituting it in Ampere's law (4.1c) in the frequency domain and using equivalences (4.10) and (4.11) yields

$$-j\omega\varepsilon_0\tilde{\varepsilon}_r\tilde{E} = j\vec{\kappa}\times\tilde{H}, \tag{4.14}$$

which can be rewritten as

$$-j\omega\varepsilon_0 \mathrm{Re}(\tilde{\varepsilon}_r)\tilde{E} + \varepsilon_0\omega\mathrm{Im}(\tilde{\varepsilon}_r)\tilde{E} = j\vec{\kappa}\times\tilde{H}. \tag{4.15}$$

For the sake of simplicity, the dependence of Fourier transformed quantities on $\vec{\kappa}$ and ω is omitted in the rest of the thesis. Then, applying the inverse Fourier transform on equation (4.15) yields

$$\varepsilon_0 \mathrm{Re}(\tilde{\varepsilon}_r)\frac{\partial\vec{E}}{\partial t} + \varepsilon_0\omega\mathrm{Im}(\tilde{\varepsilon}_r)\vec{E} = \vec{\nabla}\times\vec{H}. \tag{4.16}$$

Using different notations, Maxwell's curl equations for linear, isotropic, non-dispersive media that exhibit a local response in space read

$$\varepsilon_0\varepsilon_r\frac{\partial\vec{E}}{\partial t} + \sigma\vec{E} = \vec{\nabla}\times\vec{H}, \tag{4.17}$$

$$\mu_0\frac{\partial\vec{H}}{\partial t} + \vec{\nabla}\times\vec{E} = 0, \tag{4.18}$$

in which the relative permittivity ε_r and the conductivity σ are defined as

$$\varepsilon_r = \mathrm{Re}(\tilde{\varepsilon}_r), \tag{4.19}$$

$$\sigma = \varepsilon_0\omega\mathrm{Im}(\tilde{\varepsilon}_r). \tag{4.20}$$

It is worth noting that the complex relative permittivity $\tilde{\varepsilon}_r$ is linked to the complex refractive index $\tilde{n}$ by $\tilde{\varepsilon}_r = \tilde{n}^2$. $\mathrm{Re}(\tilde{n})$ and $\mathrm{Im}(\tilde{n})$ are usually referred to as the refractive index and the extinction coefficient, respectively. With these notations, equations (4.19) and (4.20) can be rewritten as

$$\varepsilon_r = \mathrm{Re}(\tilde{n})^2 - \mathrm{Im}(\tilde{n})^2, \tag{4.21}$$

$$\sigma = 2\varepsilon_0\omega\mathrm{Re}(\tilde{n})\mathrm{Im}(\tilde{n}). \tag{4.22}$$

4.2.5 Drude dispersive media

As mentioned in chapter 3, Bonse, Dufft and their coworkers used a Drude model to describe the optical properties of excited materials [21, 58]. The Drude model is based on a classical description of the motion of electrons. In the framework of this approach, a gas of free electrons of density N_e is considered within a fixed background of positive ions [68]. The exact mechanisms related to the electron-electron and the electron-ion interactions are not directly considered. That is, these interactions are taken into account by modifying the mass of the electrons m_e by a multiplying factor m_{opt}, leading to the effective optical mass $m_{\text{eff}} = m_e m_{\text{opt}}$ of the electrons. The electrons respond to the electric field $\vec{E}$ via the Lorentz force $-e\vec{E}$, with e being the elementary charge. Their motion is damped by collisions which have a characteristic frequency $\gamma = 1/\tau_{\text{Drude}}$, where τ_{Drude} is referred to as the relaxation time of the free electron gas or Drude damping time [58, 68]. Following this approach, the equation of motion of an electron is simply given by equation

$$m_{\text{eff}} \frac{\partial^2 \vec{x}}{\partial t^2} + m_{\text{eff}} \gamma \frac{\partial \vec{x}}{\partial t} = -e\vec{E}, \tag{4.23}$$

with $\vec{x}$ being the displacement of the electron. Applying the Fourier transform, equation (4.23) becomes

$$m_{\text{eff}} \omega^2 \tilde{x} + j m_{\text{eff}} \gamma \omega \tilde{x} = e\tilde{E}. \tag{4.24}$$

Rearranging the terms gives

$$\tilde{x} = \frac{e}{m_{\text{eff}} \left(\omega^2 + j\gamma\omega\right)} \tilde{E}. \tag{4.25}$$

The polarization of the material linked to the free electrons $\vec{P}_{\text{Drude}}$ is related to the displacement by $\vec{P}_{\text{Drude}} = -eN_e\vec{x}$, leading to

$$\tilde{P}_{\text{Drude}} = -\varepsilon_0 \frac{\omega_p^2}{\omega^2 + j\gamma\omega} \tilde{E}, \tag{4.26}$$

with the plasma frequency ω_p of the electron gas given by

$$\omega_p^2 = N_e e^2 / \left(\varepsilon_0 m_{\text{eff}}\right). \tag{4.27}$$

In the approach of Bonse, Dufft and their coworkers, the polarization $\vec{P}^*$ of excited semiconductors can be described as $\vec{P}^* = \vec{P} + \vec{P}_{\text{Drude}}$. When semiconductors are not excited, no free electrons contribute to the Drude polarization, thus, $N_e = 0$ and $\vec{P}_{\text{Drude}} = 0$. Non-excited materials are assumed to be non-dispersive and $\tilde{P}^* = \tilde{P} = \varepsilon_0 \tilde{\chi} \tilde{E}$. For Drude dispersive media describing this kind of excitation, the constitutive relation injected in Ampere's law is simply given by

$$\vec{D} = \varepsilon_0 \vec{E} + \vec{P}^* = \varepsilon_0 \vec{E} + \vec{P} + \vec{P}_{\text{Drude}}. \tag{4.28}$$

Then, Ampere's law becomes

$$\varepsilon_0 \frac{\partial \vec{E}}{\partial t} + \frac{\partial \vec{P}}{\partial t} + \vec{J}_{\text{Drude}} = \vec{\nabla} \times \vec{H}, \tag{4.29}$$

with $\vec{J}_{\text{Drude}} = \partial \vec{P}_{\text{Drude}}/\partial t$ being referred to as the Drude internal current in this thesis. For the sake of simplicity, the subscript "Drude" will be omitted since no confusion is possible.

Similarly to what was shown in the previous section, $\varepsilon_0 \vec{E} + \vec{P}$ can be expressed in the frequency domain thanks to the complex relative permittivity and the derived quantities defined by (4.19) and (4.20). Finally, following the same procedure, Ampere's law is written as

$$\varepsilon_0 \varepsilon_r \frac{\partial \vec{E}}{\partial t} + \sigma \vec{E} + \vec{J} = \vec{\nabla} \times \vec{H}. \tag{4.30}$$

However, $\vec{J}$ depends on $\vec{E}$ in a complex manner and equation (4.30) is not sufficient for the FDTD calculations by itself. The dependence of $\vec{J}$ on $\vec{E}$ must be expressed explicitly in the time domain. Starting from the frequency domain, $\tilde{J} = -j\omega \tilde{P}_{\text{Drude}}$ substituted in equation (4.26) leads to

$$\tilde{J} = j\omega \varepsilon_0 \frac{\omega_p^2}{\omega^2 + j\gamma\omega} \tilde{E}. \tag{4.31}$$

Rewriting yields

$$\left(\omega^2 + j\gamma\omega\right) \tilde{J} = j\omega \varepsilon_0 \omega_p^2 \tilde{E}, \tag{4.32}$$

which gives

$$-j\omega \tilde{J} + \gamma \tilde{J} = \varepsilon_0 \omega_p^2 \tilde{E}. \tag{4.33}$$

Reverting to the space domain gives

$$\frac{\partial \vec{J}}{\partial t} + \gamma \vec{J} = \varepsilon_0 \omega_p^2 \vec{E}, \tag{4.34}$$

which will be used to perform the FDTD calculations.

Finally, it is worth noting that equation (4.28) can be expressed by means of a complex permittivity $\tilde{\varepsilon}_r^* = \tilde{\varepsilon}_r + \Delta\tilde{\varepsilon}_{\text{Drude}}$, $\Delta\tilde{\varepsilon}_{\text{Drude}}$ being defined by

$$\Delta\tilde{\varepsilon}_{\text{Drude}} = -\frac{\omega_p^2}{\omega^2 + j\gamma\omega}, \tag{4.35}$$

which is the description used by Bonse, Dufft and their coworkers [21, 58]. With the notations described previously, $\tilde{P}_{\text{Drude}} = \varepsilon_0 \Delta\tilde{\varepsilon}_{\text{Drude}} \tilde{E}$ and $\tilde{D} = \varepsilon_0 \tilde{\varepsilon}_r^* \tilde{E}$.

4.3 Finite-difference time-domain method

The FDTD calculations performed in this thesis follow the algorithm introduced by Yee in 1966 [79]. While a modified formulation has been chosen to handle lossy and dispersive media, a similar grid is used since Yee's arrangement of the components of the fields is robust [42].

4.3.1 The Yee algorithm

The Yee algorithm solves, for both $\vec{E}$ and $\vec{H}$, the time dependent Maxwell's curl equations in differential form. That is, Ampere's law and Faraday's law are discretized using central-difference approximations for both the time derivatives and the space derivatives. The most striking characteristic of Yee's algorithm is related to the position of the components of $\vec{E}$ and $\vec{H}$ in space [79], as shown in Figure 4.1. Such an arrangement is commonly referred to as the Yee cell. Each component of $\vec{E}$ and $\vec{H}$ is surrounded by four circulating $\vec{H}$ and $\vec{E}$ components, respectively. As pointed out by Taflove and Hagness [42], Yee's algorithm simulates both the differential and integral form of the macroscopic Maxwell's equations, meaning among others that it enforces by nature both Gauss' laws (4.1a) and (4.1b) in the absence of electric and magnetic charges. Moreover, the continuity of the tangential components of $\vec{E}$ and $\vec{H}$ across an interface is insured thanks to the Yee cell arrangement. Further, $\vec{E}$ and $\vec{H}$ are not only staggered in space, but also in time. The finite-difference equations are solved in a leapfrog manner [42], meaning that $\vec{E}$ is calculated at a certain time-step, then $\vec{H}$ is calculated for the following time-step using the previously computed $\vec{E}$. The process is repeated until the desired effect is observed, such as the steady state for example.

4.3.2 Finite-differences

Maxwell's curl equations, (4.18) and (4.18), for linear, isotropic, non-dispersive media that exhibit a local response in space, read, when expressed in Cartesian coordinates:

$$\varepsilon_0 \varepsilon_r \frac{\partial E_x}{\partial t} + \sigma E_x = \frac{\partial H_z}{\partial y} - \frac{\partial H_y}{\partial z}, \tag{4.36}$$

$$\varepsilon_0 \varepsilon_r \frac{\partial E_y}{\partial t} + \sigma E_y = \frac{\partial H_x}{\partial z} - \frac{\partial H_z}{\partial x}, \tag{4.37}$$

$$\varepsilon_0 \varepsilon_r \frac{\partial E_z}{\partial t} + \sigma E_z = \frac{\partial H_y}{\partial x} - \frac{\partial H_x}{\partial y}, \tag{4.38}$$

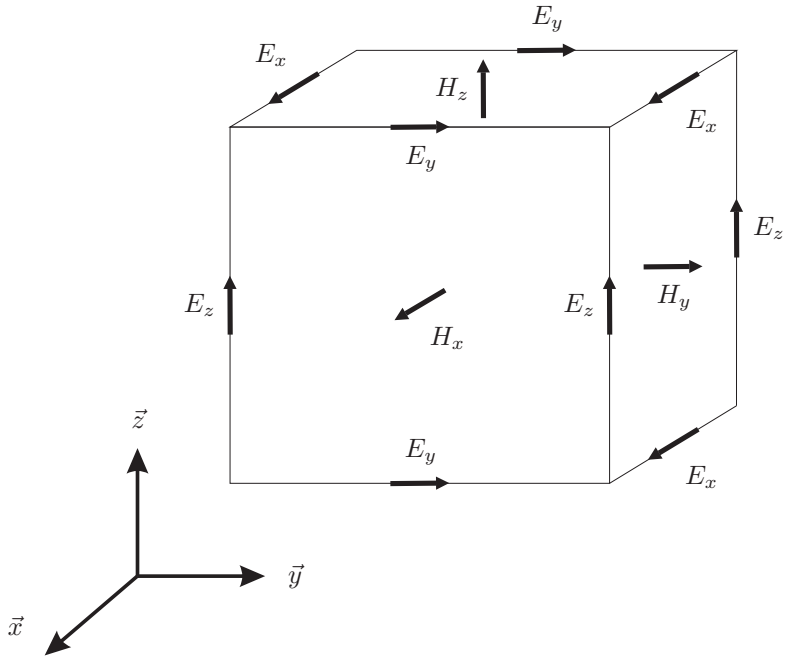

Figure 4.1: Components of $\vec{E}$ and $\vec{H}$ following a Yee cell arrangement in space. Adapted from [79].

and

$$\mu_0 \frac{\partial H_x}{\partial t} = -\left(\frac{\partial E_z}{\partial y} - \frac{\partial E_y}{\partial z}\right), \tag{4.39}$$

$$\mu_0 \frac{\partial H_y}{\partial t} = -\left(\frac{\partial E_x}{\partial z} - \frac{\partial E_z}{\partial x}\right), \tag{4.40}$$

$$\mu_0 \frac{\partial H_z}{\partial t} = -\left(\frac{\partial E_y}{\partial x} - \frac{\partial E_x}{\partial y}\right). \tag{4.41}$$

For the finite-difference calculations, Δx, Δy and Δz are used to refer to the space increments in the $\vec{x}$, $\vec{y}$ and $\vec{z}$ direction, respectively. The time increment is denoted as Δt. As mentioned previously, Yee used central-difference approximations for both the time derivatives and the space derivatives, which are second-order accurate. Taking equation (4.39) as an example, the partial derivatives evaluated at a discrete point $[(i + 1/2)\Delta x, j\Delta y, k\Delta z]$ in space and $m\Delta t$ in time are given by

$$\frac{\partial H_x}{\partial t}\left[\left(i+\frac{1}{2}\right)\Delta x, j\Delta y, k\Delta z, m\Delta t\right] = \frac{H_x|_{i+\frac{1}{2},j,k}^{m+\frac{1}{2}} - H_x|_{i+\frac{1}{2},j,k}^{m-\frac{1}{2}}}{\Delta t} + O\left[(\Delta t)^2\right], \tag{4.42}$$

$$\frac{\partial E_z}{\partial y}\left[\left(i+\frac{1}{2}\right)\Delta x, j\Delta y, k\Delta z, m\Delta t\right] = \frac{E_z|_{i+\frac{1}{2},j+\frac{1}{2},k}^{m} - E_z|_{i+\frac{1}{2},j-\frac{1}{2},k}^{m}}{\Delta y} + O\left[(\Delta y)^2\right], \tag{4.43}$$

and

$$\frac{\partial E_y}{\partial z}\left[\left(i+\frac{1}{2}\right)\Delta x, j\Delta y, k\Delta z, m\Delta t\right] = \frac{E_y|_{i+\frac{1}{2},j,k+\frac{1}{2}}^{m} - E_y|_{i+\frac{1}{2},j,k-\frac{1}{2}}^{m}}{\Delta z} + O\left[(\Delta z)^2\right], \tag{4.44}$$

where i, j, k and m are integers. Note that, the subscript j should not be confused with the imaginary unit. Similarly, the subscript k should not be confused with the wave vector $\vec{\kappa}$ of a plane wave, or the vector $\vec{k}$ spanning the frequency domain from chapter 3. $O[\bullet]$ is the big O notation used to describe the error terms.

For the sake of simplicity, the space increments are omitted when a function of space is evaluated and the time step is indicated by a superscript. The leapfrog algorithm is clear from the fact that H_x is computed at the $m+1/2$ and $m-1/2$ time steps, while E_y and E_z are available at the m^{th} time step. The space indices are in accordance with the Yee cell centered in (i,j,k). Using the finite-difference expressions, equation (4.39) is approximated numerically by

$$\begin{aligned} H_x|_{i+\frac{1}{2},j,k}^{m+\frac{1}{2}} = {} & H_x|_{i+\frac{1}{2},j,k}^{m-\frac{1}{2}} \\ & - \frac{\Delta t}{\mu_0 \Delta y}\left(E_z|_{i+\frac{1}{2},j+\frac{1}{2},k}^{m} - E_z|_{i+\frac{1}{2},j-\frac{1}{2},k}^{m}\right) \\ & + \frac{\Delta t}{\mu_0 \Delta z}\left(E_y|_{i+\frac{1}{2},j,k+\frac{1}{2}}^{m} - E_y|_{i+\frac{1}{2},j,k-\frac{1}{2}}^{m}\right). \end{aligned} \tag{4.45}$$

Equation (4.45) expresses how to calculate $H_x^{m+\frac{1}{2}}$ from $H_x^{m-\frac{1}{2}}$, E_y^m and E_z^m, which are supposed to be calculated in the previous time step. Similarly, the other components

of $\vec{H}$, H_y and H_z, can be updated by applying finite-difference approximations to (4.40) and (4.41) which gives

$$\begin{aligned} H_y|_{i,j+\frac{1}{2},k}^{m+\frac{1}{2}} &= H_y|_{i,j+\frac{1}{2},k}^{m-\frac{1}{2}} \\ &- \frac{\Delta t}{\mu_0 \Delta z}\left(E_x|_{i,j+\frac{1}{2},k+\frac{1}{2}}^{m} - E_x|_{i,j+\frac{1}{2},k-\frac{1}{2}}^{m}\right) \\ &+ \frac{\Delta t}{\mu_0 \Delta x}\left(E_z|_{i+\frac{1}{2},j+\frac{1}{2},k}^{m} - E_z|_{i-\frac{1}{2},j+\frac{1}{2},k}^{m}\right) \end{aligned} \tag{4.46}$$

and

$$\begin{aligned} H_z|_{i,j,k+\frac{1}{2}}^{m+\frac{1}{2}} &= H_z|_{i,j,k+\frac{1}{2}}^{m-\frac{1}{2}} \\ &- \frac{\Delta t}{\mu_0 \Delta x}\left(E_y|_{i+\frac{1}{2},j,k+\frac{1}{2}}^{m} - E_y|_{i-\frac{1}{2},j,k+\frac{1}{2}}^{m}\right) \\ &+ \frac{\Delta t}{\mu_0 \Delta y}\left(E_x|_{i,j+\frac{1}{2},k+\frac{1}{2}}^{m} - E_x|_{i,j-\frac{1}{2},k+\frac{1}{2}}^{m}\right), \end{aligned} \tag{4.47}$$

respectively.

The update of $\vec{E}$ is slightly different due to the $\sigma\vec{E}$ term in equation (4.17). Applying central differences to equation (4.36) for example, leads to

$$\begin{aligned} &\varepsilon_0\varepsilon_r \frac{E_x|_{i,j+\frac{1}{2},k+\frac{1}{2}}^{m+1} - E_x|_{i,j+\frac{1}{2},k+\frac{1}{2}}^{m}}{\Delta t} + \sigma E_x|_{i,j+\frac{1}{2},k+\frac{1}{2}}^{m+\frac{1}{2}} = \\ &\frac{H_z|_{i,j+1,k+\frac{1}{2}}^{m+\frac{1}{2}} - H_z|_{i,j,k+\frac{1}{2}}^{m+\frac{1}{2}}}{\Delta y} - \frac{H_y|_{i,j+\frac{1}{2},k+1}^{m+\frac{1}{2}} - H_y|_{i,j+\frac{1}{2},k}^{m+\frac{1}{2}}}{\Delta z}. \end{aligned} \tag{4.48}$$

While E_x^m, $H_z^{m+\frac{1}{2}}$ and $H_y^{m+\frac{1}{2}}$ are known from the previous time step, $E_x^{m+\frac{1}{2}}$ is not. A simple way to handle this case is to assume that $E_x^{m+\frac{1}{2}}$ is well described by the arithmetic average of E_x^{m+1} and E_x^m

$$E_x^{m+\frac{1}{2}} = \frac{E_x^{m+1} + E_x^m}{2}. \tag{4.49}$$

This assumption leads to stable and accurate results [42]. Except for this specific case, the rest of the discretization is straightforward and results in

$$\begin{aligned} E_x|_{i,j+\frac{1}{2},k+\frac{1}{2}}^{m+1} &= \frac{2\varepsilon_0\varepsilon_r - \sigma\Delta t}{2\varepsilon_0\varepsilon_r + \sigma\Delta t} E_x|_{i,j+\frac{1}{2},k+\frac{1}{2}}^{m} \\ &+ \frac{2\Delta t/\Delta y}{2\varepsilon_0\varepsilon_r + \sigma\Delta t}\left(H_z|_{i,j+1,k+\frac{1}{2}}^{m+\frac{1}{2}} - H_z|_{i,j,k+\frac{1}{2}}^{m+\frac{1}{2}}\right) \\ &- \frac{2\Delta t/\Delta z}{2\varepsilon_0\varepsilon_r + \sigma\Delta t}\left(H_y|_{i,j+\frac{1}{2},k+1}^{m+\frac{1}{2}} - H_y|_{i,j+\frac{1}{2},k}^{m+\frac{1}{2}}\right). \end{aligned} \tag{4.50}$$

Following the same procedure for equations (4.37) and (4.38) leads to a complete update of $\vec{E}$ by calculating

$$\begin{aligned} E_y|^{m+1}_{i+\frac{1}{2},j,k+\frac{1}{2}} &= \frac{2\varepsilon_0\varepsilon_r - \sigma\Delta t}{2\varepsilon_0\varepsilon_r + \sigma\Delta t} E_x|^{m}_{i+\frac{1}{2},j,k+\frac{1}{2}} \\ &+ \frac{2\Delta t/\Delta z}{2\varepsilon_0\varepsilon_r + \sigma\Delta t}\left(H_x|^{m+\frac{1}{2}}_{i+\frac{1}{2},j,k+1} - H_x|^{m+\frac{1}{2}}_{i+\frac{1}{2},j,k}\right) \\ &- \frac{2\Delta t/\Delta x}{2\varepsilon_0\varepsilon_r + \sigma\Delta t}\left(H_z|^{m+\frac{1}{2}}_{i+1,j,k+\frac{1}{2}} - H_z|^{m+\frac{1}{2}}_{i,j,k+\frac{1}{2}}\right) \end{aligned} \tag{4.51}$$

and

$$\begin{aligned} E_z|^{m+1}_{i+\frac{1}{2},j+\frac{1}{2},k} &= \frac{2\varepsilon_0\varepsilon_r - \sigma\Delta t}{2\varepsilon_0\varepsilon_r + \sigma\Delta t} E_z|^{m}_{i+\frac{1}{2},j+\frac{1}{2},k} \\ &+ \frac{2\Delta t/\Delta x}{2\varepsilon_0\varepsilon_r + \sigma\Delta t}\left(H_y|^{m+\frac{1}{2}}_{i+1,j+\frac{1}{2},k} - H_y|^{m+\frac{1}{2}}_{i,j+\frac{1}{2},k}\right) \\ &- \frac{2\Delta t/\Delta y}{2\varepsilon_0\varepsilon_r + \sigma\Delta t}\left(H_x|^{m+\frac{1}{2}}_{i+\frac{1}{2},j+1,k} - H_x|^{m+\frac{1}{2}}_{i+\frac{1}{2},j,k}\right). \end{aligned} \tag{4.52}$$

4.3.3 Auxiliary differential equation method

In the case of Drude dispersive media, an extra term, the Drude internal current $\vec{J}$, is needed to update $\vec{E}$ by using equation (4.30). A technique, referred to as the auxiliary differential equation (ADE) method, is commonly used to treat this problem [42, 83]. Using the ADE method, $\vec{J}$ is accounted for by considering equation (4.34) which is differentiated, employing arithmetic average when necessary, into

$$\vec{J}^{m+1} = \frac{2-\gamma\Delta t}{2+\gamma\Delta t}\vec{J}^{m} + \frac{\varepsilon_0\Delta t\omega_p^2}{2+\gamma\Delta t}\left(\vec{E}^{m+1} + \vec{E}^{m}\right). \tag{4.53}$$

As for the $\sigma\vec{E}$ term discussed in the previous section, $\vec{J}^{m+1/2}$ appears when (4.30) is differentiated. Using the arithmetic average and equation (4.53), $\vec{J}^{m+1/2}$ is given by

$$\vec{J}^{m+\frac{1}{2}} = \frac{\vec{J}^{m+1} + \vec{J}^{m}}{2} = \frac{1}{2}\left[(1+\alpha)\,\vec{J}^{m} + \beta\left(\vec{E}^{m+1} + \vec{E}^{m}\right)\right], \tag{4.54}$$

with α and β being defined by

$$\alpha = \frac{2-\gamma\Delta t}{2+\gamma\Delta t} \tag{4.55}$$

and

$$\beta = \frac{\varepsilon_0\omega_p^2\Delta t}{2+\gamma\Delta t}. \tag{4.56}$$

Then, $\vec{E}$ is updated in the same manner as for non-dispersive media with few extra terms related to $\vec{J}$,

$$\begin{aligned} E_x^{m+1} = & \frac{2\varepsilon_0\varepsilon_r - (\sigma+\beta)\Delta t}{2\varepsilon_0\varepsilon_r + (\sigma+\beta)\Delta t} E_x^m \\ & + \frac{2\Delta t}{2\varepsilon_0\varepsilon_r + (\sigma+\beta)\Delta t} \left[\vec{\nabla} \times \vec{H}^{m+\frac{1}{2}} - (1+\alpha)\,\Delta t \vec{J}^m\right]. \end{aligned} \tag{4.57}$$

Handling $\vec{H}$ is done in the same manner as for non-dispersive media since the same equations are governing the variations of the magnetic field. That is, $\vec{H}$ is updated via equations (4.45), (4.46) and (4.47). With equations (4.50), (4.51), (4.52), (4.54) and (4.57), all the equations necessary to update the electric field have been presented. Now, the core of the FDTD calculations is complete, but, boundary conditions and source terms are required obtaining results.

It is worth noting that the absorbed energy per Yee cell is simply computed by adding the electrical losses at each time step

$$\left[\sigma \left(\vec{E}^m\right)^2 + \vec{J}^m \cdot \vec{E}^m\right] \Delta t \Delta x \Delta y \Delta z. \tag{4.58}$$

4.3.4 Numerical stability and accuracy

Taflove and Brodwin derived the criteria for the stability of Yee's algorithm for lossless media [84]. For three dimensional FDTD calculations in a Cartesian frame, the unstable range of the algorithm is reached when $\Delta t > \Delta t_{\max}$, where $\Delta t_{\max}$ is defined as

$$\Delta t_{\max} = \frac{1}{c\sqrt{\frac{1}{\Delta x^2} + \frac{1}{\Delta y^2} + \frac{1}{\Delta z^2}}}. \tag{4.59}$$

where c is the speed of light in vacuum.

Regarding lossy media, Pereda et al. show that when the arithmetic average is used to describe the $\sigma\vec{E}$ term, as proposed in equation (4.49) and (4.50) for example, an identical criteria as the one for lossless media can be derived [85]. For Drude media, Chun et al. proved that the same stability criteria can also be applied [86].

While Δt is bounded by a clear rule, Δx, Δy and Δz are chosen empirically, in function of the smaller wavelength in the simulation domain. The smaller these values are chosen, the more accurate the simulation will be. However, it comes at the price of a loss of computation speed and an increase in computer memory usage. It is commonly accepted that 10 to 20 cells per wavelength lead to accurate results [42].

Regardless of the dimensions chosen for the geometrical grid, the Yee algorithm, including lossy media, is known to be unstable when ε_r is negative [87, 88]. In this case, it is necessary to simulate the response of the material by the Drude model for example (see section 4.2.5 and section 4.3.3).

4.4 Boundary conditions

The core of the FDTD calculations has been presented in section 4.3, but the boundary conditions have to be handled. A source term is necessary, which is introduced in the simulation domain via the total-field scattered-field (TFSF) technique [42]. Moreover, the simulation domain has a finite size and specific boundary conditions, such as the convolution perfectly matched layer (CPML) [89], have to be implemented to avoid non-physical reflections of the electromagnetic fields at the boundaries of the simulation domain.

4.4.1 Total-field scattered-field technique

The TFSF technique allows to introduce plane waves in the simulation domain and has been extensively discussed by Taflove and Hagness in [42]. For the sake of completeness, the features related to the TFSF method, necessary to understand the FDTD calculations presented in this thesis, are explained in this section. The concept behind the TFSF method is that the electric field and the magnetic field are decomposed into the incident and the scattered fields, as expressed mathematically by

$$\vec{E} = \vec{E}_{\text{inc}} + \vec{E}_{\text{scat}} \tag{4.60}$$

and

$$\vec{H} = \vec{H}_{\text{inc}} + \vec{H}_{\text{scat}} \tag{4.61}$$

Here, the incident fields, $\vec{E}_{\text{inc}}$ and $\vec{H}_{\text{inc}}$, are the fields which would propagate without the presence of scatterers in the simulation domain, which is the roughness in this thesis. They are assumed to be known at any grid points. The scattered fields, $\vec{E}_{\text{scat}}$ and $\vec{H}_{\text{scat}}$, are the fields resulting from the interaction of the incident fields with the scatterers and are are initially unknown.

Due to the linearity of Maxwell's equations, the incident and scattered fields can be handled independently. Hence, it is possible to apply the FDTD calculations only on the total-fields (TFs) or on the scattered-fields (SFs) as shown in Figure 4.2. Starting with the one dimensional case, assuming that only $E_x \neq 0$ and $H_y \neq 0$, the FDTD calculations follow their usual scheme in the TFs and SFs regions. That is, the expressions for non-dispersive media are computed according to

$$\begin{aligned} E_x|_{k+\frac{1}{2}}^{m+1} = {} & \frac{2\varepsilon_0\varepsilon_r - \sigma\Delta t}{2\varepsilon_0\varepsilon_r + \sigma\Delta t} E_x|_{k+\frac{1}{2}}^{m} \\ & - \frac{2\Delta t/\Delta z}{2\varepsilon_0\varepsilon_r + \sigma\Delta t} \left(H_y|_{k+1}^{m+\frac{1}{2}} - H_y|_{k}^{m+\frac{1}{2}} \right), \end{aligned} \tag{4.62}$$

$$H_y|_{k}^{m+\frac{1}{2}} = H_y|_{k}^{m-\frac{1}{2}} - \frac{\Delta t}{\mu_0 \Delta z} \left(E_x|_{k+\frac{1}{2}}^{m} - E_x|_{k-\frac{1}{2}}^{m} \right), \tag{4.63}$$

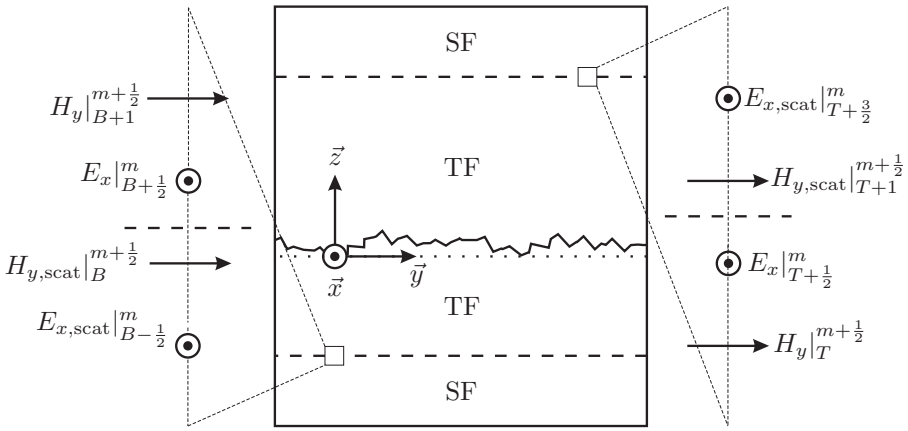

Figure 4.2: Zones of the FDTD calculations with respect to the TFs and SFs. The problems occurring at the interfaces are shown on the right and left side of the drawing.

$$E_{x,\mathrm{scat}}|_{k+\frac{1}{2}}^{m+1} = \frac{2\varepsilon_0\varepsilon_r - \sigma\Delta t}{2\varepsilon_0\varepsilon_r + \sigma\Delta t} E_{x,\mathrm{scat}}|_{k+\frac{1}{2}}^{m} - \frac{2\Delta t/\Delta z}{2\varepsilon_0\varepsilon_r + \sigma\Delta t}\left(H_{y,\mathrm{scat}}|_{k+1}^{m+\frac{1}{2}} - H_{y,\mathrm{scat}}|_{k}^{m+\frac{1}{2}}\right), \tag{4.64}$$

and

$$H_{y,\mathrm{scat}}|_{k}^{m+\frac{1}{2}} = H_{y,\mathrm{scat}}|_{k}^{m-\frac{1}{2}} - \frac{\Delta t}{\mu_0\Delta z}\left(E_{x,\mathrm{scat}}|_{k+\frac{1}{2}}^{m} - E_{x,\mathrm{scat}}|_{k-\frac{1}{2}}^{m}\right). \tag{4.65}$$

It is worth noting that the vacuum region is just a specific type of non-dispersive medium, with $\varepsilon_r = 1$ and $\sigma = 0$. However, problems occur at the interface between the TFs and SFs region as indicated in Figure 4.2. Indeed, if the FDTD calculations are performed incautiously at the interfaces, the following equations are obtained:

$$E_x|_{T+\frac{1}{2}}^{m+1} = \frac{2\varepsilon_0\varepsilon_r - \sigma\Delta t}{2\varepsilon_0\varepsilon_r + \sigma\Delta t} E_x|_{T+\frac{1}{2}}^{m} - \frac{2\Delta t/\Delta z}{2\varepsilon_0\varepsilon_r + \sigma\Delta t}\left(H_{y,\mathrm{scat}}|_{T+1}^{m+\frac{1}{2}} - H_y|_{T}^{m+\frac{1}{2}}\right), \tag{4.66}$$

$$H_{y,\mathrm{scat}}|_{T+1}^{m+\frac{1}{2}} = H_{y,\mathrm{scat}}|_{T+1}^{m-\frac{1}{2}} - \frac{\Delta t}{\mu_0\Delta z}\left(E_{x,\mathrm{scat}}|_{T+\frac{3}{2}}^{m} - E_x|_{T+\frac{1}{2}}^{m}\right), \tag{4.67}$$

$$E_x|_{B+\frac{1}{2}}^{m+1} = \frac{2\varepsilon_0\varepsilon_r - \sigma\Delta t}{2\varepsilon_0\varepsilon_r + \sigma\Delta t} E_x|_{B+\frac{1}{2}}^{m} - \frac{2\Delta t/\Delta z}{2\varepsilon_0\varepsilon_r + \sigma\Delta t}\left(H_y|_{B+1}^{m+\frac{1}{2}} - H_{y,\mathrm{scat}}|_{B}^{m+\frac{1}{2}}\right), \tag{4.68}$$

and

$$H_{y,\mathrm{scat}}|_{B}^{m+\frac{1}{2}} = H_{y,\mathrm{scat}}|_{B}^{m-\frac{1}{2}} - \frac{\Delta t}{\mu_0\Delta z}\left(E_x|_{B+\frac{1}{2}}^{m} - E_{x,\mathrm{scat}}|_{B-\frac{1}{2}}^{m}\right). \tag{4.69}$$

These equations are not consistent since they mix FDTD calculations between total-fields and scattered-fields. Recalling that the incident fields are assumed to be known, equations (4.60) and (4.61) can be used to make the equations consistent, leading to

$$\begin{aligned} E_x|_{T+\frac{1}{2}}^{m+1} = {} & \frac{2\varepsilon_0\varepsilon_r - \sigma\Delta t}{2\varepsilon_0\varepsilon_r + \sigma\Delta t} E_x|_{T+\frac{1}{2}}^{m} \\ & - \frac{2\Delta t/\Delta z}{2\varepsilon_0\varepsilon_r + \sigma\Delta t}\left(H_{y,\mathrm{scat}}|_{T+1}^{m+\frac{1}{2}} - H_y|_{T}^{m+\frac{1}{2}}\right) \\ & - \frac{2\Delta t/\Delta z}{2\varepsilon_0\varepsilon_r + \sigma\Delta t} H_{y,\mathrm{inc}}|_{T+1}^{m+\frac{1}{2}}, \end{aligned} \tag{4.70}$$

$$\begin{aligned} H_{y,\mathrm{scat}}|_{T+1}^{m+\frac{1}{2}} = {} & H_{y,\mathrm{scat}}|_{T+1}^{m-\frac{1}{2}} - \frac{\Delta t}{\mu_0\Delta z}\left(E_{x,\mathrm{scat}}|_{T+\frac{3}{2}}^{m} - E_x|_{T+\frac{1}{2}}^{m}\right) \\ & - \frac{\Delta t}{\mu_0\Delta z} E_{x,\mathrm{inc}}|_{T+\frac{1}{2}}^{m}, \end{aligned} \tag{4.71}$$

$$\begin{aligned} E_x|_{B+\frac{1}{2}}^{m+1} = {} & \frac{2\varepsilon_0\varepsilon_r - \sigma\Delta t}{2\varepsilon_0\varepsilon_r + \sigma\Delta t} E_x|_{B+\frac{1}{2}}^{m} \\ & - \frac{2\Delta t/\Delta z}{2\varepsilon_0\varepsilon_r + \sigma\Delta t}\left(H_y|_{B+1}^{m+\frac{1}{2}} - H_{y,\mathrm{scat}}|_{B}^{m+\frac{1}{2}}\right) \\ & + \frac{2\Delta t/\Delta z}{2\varepsilon_0\varepsilon_r + \sigma\Delta t} H_{y,\mathrm{inc}}|_{B}^{m+\frac{1}{2}}, \end{aligned} \tag{4.72}$$

and

$$\begin{aligned} H_{y,\mathrm{scat}}|_{B}^{m+\frac{1}{2}} = {} & H_{y,\mathrm{scat}}|_{B}^{m-\frac{1}{2}} - \frac{\Delta t}{\mu_0\Delta z}\left(E_x|_{B+\frac{1}{2}}^{m} - E_{x,\mathrm{scat}}|_{B-\frac{1}{2}}^{m}\right) \\ & + \frac{\Delta t}{\mu_0\Delta z} E_{x,\mathrm{inc}}|_{B+\frac{1}{2}}^{m}. \end{aligned} \tag{4.73}$$

Thanks to equations (4.70) through (4.73), the TFs and SFs are well handled at the interfaces. It is now possible to introduce the source term, which is simply given by

$$E_x|^{m+1}_{T+\frac{1}{2}} = E_x|^{m}_{T+\frac{1}{2}} + E_0 \sin\left(2\pi\frac{c}{\lambda}m\Delta t\right). \tag{4.74}$$

where λ and c denote the wavelength of the laser radiation and the speed of light in vacuum, respectively.

To calculate the incident fields, it is sufficient to run a one dimensional (1D) FDTD scheme in parallel to the main scheme, without the scatterers. Hence, $E_{x,\mathrm{inc}}$ and $H_{y,\mathrm{inc}}$ are known at every time step via the 1D FDTD scheme and can be subtracted or added to keep the consistency of the main FDTD scheme. Following the above mentioned procedure, a plane wave traveling only in the TF region can be introduced in the simulation domain.

For the sake of simplicity, it was assumed that only $E_x \neq 0$ and $H_y \neq 0$. This is also sufficient for the purpose of this thesis. Since the focus is put on the interaction of linearly polarized light, arriving at normal incidence, with rough surfaces, it is always possible to assume that the incident light is polarized along $\vec{x}$. In this case, the plane wave travels along $\vec{z}$ and only $E_{x,\mathrm{inc}} \neq 0$ and $H_{y,\mathrm{inc}} \neq 0$.

4.4.2 Periodic boundary conditions

Due to limited computer memory, the simulation domain has to have finite dimensions. This causes problems at the edges of the simulation domain, as shown in Figure 4.3. At the edge of the simulation domain in the $\vec{y}$ direction, a Yee cell is cut in half (dotted lines). In this region, the update equation for H_x, for example, is simply given by

$$\begin{aligned} H_x|^{m+\frac{1}{2}}_{i+\frac{1}{2},\mathrm{end},k} &= H_x|^{m-\frac{1}{2}}_{i+\frac{1}{2},\mathrm{end},k} \\ &- \frac{\Delta t}{\mu_0 \Delta y}\left(E_z|^{m}_{i+\frac{1}{2},\mathrm{end}+\frac{1}{2},k} - E_z|^{m}_{i+\frac{1}{2},\mathrm{end}-\frac{1}{2},k}\right) \\ &+ \frac{\Delta t}{\mu_0 \Delta z}\left(E_y|^{m}_{i+\frac{1}{2},\mathrm{end},k+\frac{1}{2}} - E_y|^{m}_{i+\frac{1}{2},\mathrm{end},k-\frac{1}{2}}\right). \end{aligned} \tag{4.75}$$

However, $E_z|^{m}_{i+\frac{1}{2},\mathrm{end}+\frac{1}{2},k}$ does not exist and therefore H_x cannot be updated. Since LIPSSs are periodic, periodic boundary conditions are well adapted to circumvent this problem. Hence, $E_z|^{m}_{i+\frac{1}{2},\mathrm{end}+\frac{1}{2},k}$ is assumed to be equal to $E_z|^{m}_{i+\frac{1}{2},\frac{1}{2},k}$,

$$E_z|^{m}_{i+\frac{1}{2},\mathrm{end}+\frac{1}{2},k} = E_z|^{m}_{i+\frac{1}{2},\frac{1}{2},k}. \tag{4.76}$$

Similarly, H_z, E_x and E_z need periodic boundary conditions for their update in the $\vec{y}$ direction, which are given by

$$E_x|^{m}_{i,\mathrm{end}+\frac{1}{2},k+\frac{1}{2}} = E_x|^{m}_{i,\frac{1}{2},k+\frac{1}{2}}, \tag{4.77}$$

$$H_z|^{m-\frac{1}{2}}_{i,0,k+\frac{1}{2}} = H_z|^{m-\frac{1}{2}}_{i,\mathrm{end},k+\frac{1}{2}}, \tag{4.78}$$

and

$$H_x|^{m-\frac{1}{2}}_{i+\frac{1}{2},0,k} = H_x|^{m-\frac{1}{2}}_{i+\frac{1}{2},\mathrm{end},k} \tag{4.79}$$

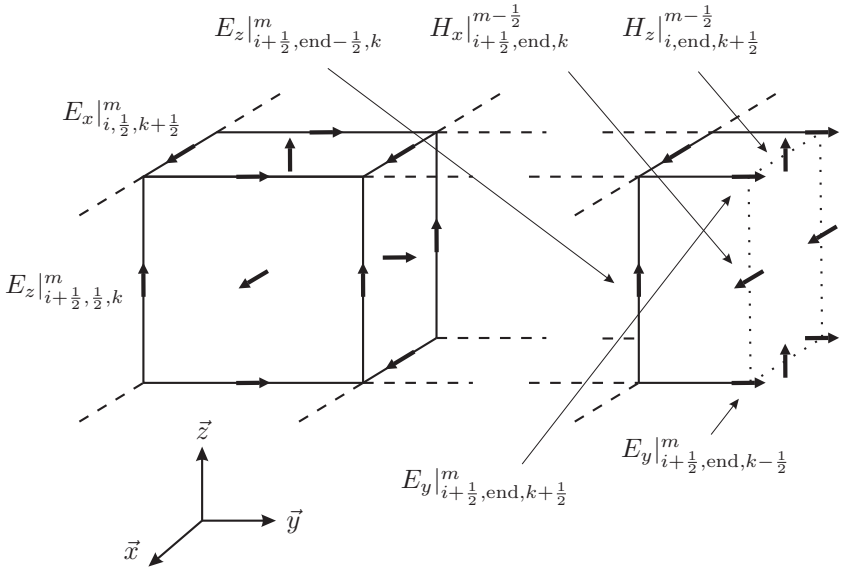

Figure 4.3: Drawing of a part of the simulation domain showing the necessity of handling the boundary conditions in the $\vec{y}$ direction.

In the $\vec{x}$ direction, boundary conditions need to be specified to update E_y, E_z, H_y and H_z. These conditions are given by

$$H_z|^{m-\frac{1}{2}}_{0,j,k+\frac{1}{2}} = H_z|^m_{\mathrm{end},j,k+\frac{1}{2}}, \tag{4.80}$$

$$H_y|^{m-\frac{1}{2}}_{0,j+\frac{1}{2},k} = H_y|^{m-\frac{1}{2}}_{\mathrm{end},j+\frac{1}{2},k}, \tag{4.81}$$

$$E_z|^m_{\mathrm{end}+\frac{1}{2},j+\frac{1}{2},k} = E_z|^m_{\frac{1}{2},j+\frac{1}{2},k} \tag{4.82}$$

and

$$E_y|^m_{\mathrm{end}+\frac{1}{2},j,k+\frac{1}{2}} = E_y|^m_{\frac{1}{2},j,k+\frac{1}{2}} \tag{4.83}$$

In the $\vec{z}$ direction, no periodic boundary conditions are needed, as shown in Figure 4.2. Instead, the scattered fields need to be handled in order to avoid non-physical reflections in the simulation domain. This is achieved by using the convolution perfectly matched layers (CPMLs) in this thesis.

4.4.3 Convolution perfectly matched layer

As discussed above, the electromagnetic field cannot be updated easily at the edges of the simulation domain. If these fields are kept constant, equal to 0,

non-physical reflexions occur when an electromagnetic wave reaches the boundary of the simulation domain. Several authors have put considerable efforts to avoid such reflections in order to simulate unbounded regions, such as a semi-infinitely extended substrate. One of the most important developments to that regard lies in the work of Berenger [90]. Berenger described the perfectly matched layer (PML), which is a part of the simulation domain that allows electromagnetic waves to "pass through" without reflections. More importantly, the PML can be designed to absorb electromagnetic waves, therefore to simulate unbounded regions. Theoretically, in non-discretized space, the PML of Berenger is perfectly matched with the host medium. However, in practice, the discretization degrades the PML performance and reflections do occur. Several alternatives and improvements to the PML have been proposed and many references can be found in the book of Taflove and Hagness [42]. From these techniques, the convolution PML (CPML) has been chosen in this thesis [89], due to its efficiency and adaptability.

For the sake of simplicity and concision, the fundamentals regarding how the PML and CPML work are not discussed in this thesis, since very good explanations are available in literature [42, 89]. Instead, the steps required for the implementation of the algorithm, in the specific case of this thesis, are presented. The key concept is to calculate extra functions Ψ and to use these to modify the fields. In the case of a CPML orthogonal to the $\vec{z}$ axis, only E_x, E_y, H_x and H_y need to be modified in the CPML region. For example, in a CPML region which is N_{med} cells thick, related to the medium, the Ψ function associated with E_x, denoted here as Ψ_{E_x}, is given by equation (4.84) [42].

$\forall k \in [1, N_{\text{med}}]$,

$$\begin{aligned}\Psi_{E_x}\big|_{i,j+\frac{1}{2},k+\frac{1}{2}}^{m+\frac{1}{2}} &= \psi_1|_{k+\frac{1}{2}}\,\Psi_{E_x}\big|_{i,j+\frac{1}{2},k+\frac{1}{2}}^{m-\frac{1}{2}} \\ &\quad + \frac{\psi_2|_{k+\frac{1}{2}}}{\Delta z}\left(H_y\big|_{i,j+\frac{1}{2},k+1}^{m+\frac{1}{2}} - H_y\big|_{i,j+\frac{1}{2},k}^{m+\frac{1}{2}}\right)\end{aligned} \tag{4.84}$$

where $\Psi_{E_x} \neq 0$ only in the CPML region. The coefficients ψ_1 and ψ_2 are defined as

$$\psi_1|_{k+\frac{1}{2}} = \exp\left[-\frac{\Delta t}{\epsilon_0}\left(\rho|_{k+\frac{1}{2}} + \xi|_{k+\frac{1}{2}}\right)\right] \tag{4.85}$$

and

$$\psi_2|_{k+\frac{1}{2}} = \frac{\xi|_{k+\frac{1}{2}}}{\rho|_{k+\frac{1}{2}} + \xi|_{k+\frac{1}{2}}}\left(\psi_1|_{k+\frac{1}{2}} - 1\right). \tag{4.86}$$

Note that ψ_1 and ψ_2 change gradually with z via ξ and ρ. A polynomial scaling of ξ and ρ usually gives good results and is used in this thesis. Hence, ξ and ρ are defined by

$$\xi_{\text{med}}|_k = \xi_{\text{med}}^{\max}\left(\frac{N_{\text{med}} - k + 1}{N_{\text{med}}}\right)^{m_\xi} \tag{4.87}$$

and

$$\rho_{\text{med}}|_k = \rho_{\text{med}}^{\max}\left(\frac{k}{N_{\text{med}}}\right)^{m_\rho}. \tag{4.88}$$

where $\xi_{\text{med}}^{\max}$, $\rho_{\text{med}}^{\max}$, m_ξ and m_ρ are the maximum of the ξ function, the maximum of the ρ function, the order of the ξ polynomial and the order of the ρ polynomial, respectively. These coefficients are usually tuned, depending on the laser wavelength and the geometry of the problem, to obtain the smallest reflections and the largest absorption. It is worth noting that ξ is maximum at the edge of the simulation grid while it is the contrary for ρ.

Once the Ψ_{E_x} function has been calculated, it is used to modify E_x via

$$E_x|^{m+1}_{i,j+\frac{1}{2},k+\frac{1}{2}} = u\left(E_x|^{m}_{i,j+\frac{1}{2},k+\frac{1}{2}}\right) - \frac{2\Delta t}{2\varepsilon_0\varepsilon_r + \sigma\Delta t}\Psi_{E_x}|^{m+\frac{1}{2}}_{i,j+\frac{1}{2},k+\frac{1}{2}}. \tag{4.89}$$

E_x is first updated in the same manner as for the usual FDTD calculations, $u\left(E_x|^{m}_{i,j+\frac{1}{2},k+\frac{1}{2}}\right)$, then modified using Ψ_{E_x}.

Similar Ψ functions need to be calculated for E_y, H_x and H_y for the CPML region to work. These functions and the expressions required to update the fields are given by the following equations:

$$\begin{aligned}\Psi_{E_y}|^{m+\frac{1}{2}}_{i+\frac{1}{2},j,k+\frac{1}{2}} &= \psi_1|_{k+\frac{1}{2}}\Psi_{E_y}|^{m-\frac{1}{2}}_{i+\frac{1}{2},j,k+\frac{1}{2}} \\ &\quad + \frac{\psi_2|_{k+\frac{1}{2}}}{\Delta z}\left(H_x|^{m+\frac{1}{2}}_{i+\frac{1}{2},j,k+1} - H_x|^{m+\frac{1}{2}}_{i+\frac{1}{2},j,k}\right),\end{aligned} \tag{4.90}$$

$$E_y|^{m+1}_{i+\frac{1}{2},j,k+\frac{1}{2}} = u\left(E_y|^{m}_{i+\frac{1}{2},j,k+\frac{1}{2}}\right) + \frac{2\Delta t}{2\varepsilon_0\varepsilon_r + \sigma\Delta t}\Psi_{E_y}|^{m+\frac{1}{2}}_{i+\frac{1}{2},j,k+\frac{1}{2}}, \tag{4.91}$$

$$\begin{aligned}\Psi_{H_x}|^{m}_{i+\frac{1}{2},j,k} &= \psi_1|_k\Psi_{H_x}|^{m-1}_{i+\frac{1}{2},j,k} \\ &\quad + \frac{\psi_2|_k}{\Delta z}\left(E_y|^{m}_{i+\frac{1}{2},j,k+\frac{1}{2}} - E_y|^{m}_{i+\frac{1}{2},j,k-\frac{1}{2}}\right),\end{aligned} \tag{4.92}$$

$$H_x|^{m+\frac{1}{2}}_{i+\frac{1}{2},j,k} = u\left(H_x|^{m-\frac{1}{2}}_{i+\frac{1}{2},j,k}\right) + \frac{\Delta t}{\mu_0}\Psi_{H_x}|^{m}_{i+\frac{1}{2},j,k}, \tag{4.93}$$

$$\begin{aligned}\Psi_{H_y}|^{m}_{i,j+\frac{1}{2},k} &= \psi_1|_k\Psi_{H_y}|^{m-1}_{i,j+\frac{1}{2},k} \\ &\quad + \frac{\psi_2|_k}{\Delta z}\left(E_x|^{m}_{i,j+\frac{1}{2},k+\frac{1}{2}} - E_x|^{m}_{i,j+\frac{1}{2},k-\frac{1}{2}}\right),\end{aligned} \tag{4.94}$$

and

$$H_y|^{m+\frac{1}{2}}_{i,j+\frac{1}{2},k} = u\left(H_y|^{m-\frac{1}{2}}_{i,j+\frac{1}{2},k}\right) - \frac{\Delta t}{\mu_0}\Psi_{H_y}|^{m}_{i,j+\frac{1}{2},k}. \tag{4.95}$$

For Drude dispersive media, the Ψ functions are calculated in the same manner as for non-dispersive media [42]. However, E_x and E_y are modified in the CPML region according to

$$\begin{aligned} E_x|^{m+1}_{i,j+\frac{1}{2},k+\frac{1}{2}} &= u\left(E_x|^{m}_{i,j+\frac{1}{2},k+\frac{1}{2}}\right) \\ &\quad - \frac{2\Delta t}{2\varepsilon_0\varepsilon_r + \Delta t\,(\sigma+\beta)}\Psi_{E_x}|^{m+\frac{1}{2}}_{i,j+\frac{1}{2},k+\frac{1}{2}} \end{aligned} \tag{4.96}$$

and

$$\begin{aligned} E_y|^{m+1}_{i+\frac{1}{2},j,k+\frac{1}{2}} &= u\left(E_y|^{m}_{i+\frac{1}{2},j,k+\frac{1}{2}}\right) \\ &\quad + \frac{2\Delta t}{2\varepsilon_0\varepsilon_r + \Delta t\,(\sigma+\beta)}\Psi_{E_y}|^{m+\frac{1}{2}}_{i+\frac{1}{2},j,k+\frac{1}{2}}. \end{aligned} \tag{4.97}$$

Moreover, the equations to update J_x and J_y need to be slightly modified, because they involve E_x and E_y, as described by

$$\begin{aligned} J_x|^{m+1}_{i,j+\frac{1}{2},k+\frac{1}{2}} &= u\left(J_x|^{m}_{i,j+\frac{1}{2},k+\frac{1}{2}}\right) \\ &\quad - \frac{2\Delta t\beta}{2\varepsilon_0\varepsilon_r + \Delta t\,(\sigma+\beta)}\Psi_{E_x}|^{m+\frac{1}{2}}_{i,j+\frac{1}{2},k+\frac{1}{2}} \end{aligned} \tag{4.98}$$

and

$$\begin{aligned} J_y|^{m+1}_{i+\frac{1}{2},j,k+\frac{1}{2}} &= u\left(J_y|^{m}_{i+\frac{1}{2},j,k+\frac{1}{2}}\right) \\ &\quad + \frac{2\Delta t\beta}{2\varepsilon_0\varepsilon_r + \Delta t\,(\sigma+\beta)}\Psi_{E_y}|^{m+\frac{1}{2}}_{i+\frac{1}{2},j,k+\frac{1}{2}}. \end{aligned} \tag{4.99}$$

So far, the CPML equations have been presented for the medium region but they are almost identical for the upper part of the simulation domain. That is, above the rough surface in Figure 4.2. The only difference concerns the ξ and ρ polynomials, which have to be scaled inversely compared to equations (4.87) and (4.88).

4.5 Conclusion

In this chapter, the background and equations required to perform FDTD calculations for plane waves interacting with rough surfaces have been presented. The plane waves are launched in the simulation domain via the TFSF technique and arrive at normal incidence at the surface of the medium. Periodic boundary conditions were introduced in the $\vec{x}$ and $\vec{y}$ direction to simulate infinitely extended rough surfaces. Similarly, CPMLs were introduced to terminate the simulation domain in the $\vec{z}$ direction. Equations for FDTD calculations in non-dispersive as well as dispersive media were derived. Using the results from this chapter, the interaction of plane waves with rough surfaces is studied numerically and compared to the Sipe theory in the next chapter.

Chapter 5

Comparison of the FDTD simulations and the Sipe theory

In this chapter, the absorbed energy below the rough surface of materials is studied based on the results of FDTD calculations. First, the numerical results are compared to the analytical approach provided by Sipe and his coworkers. Next, new insights brought by the numerical simulations are discussed.

5.1 Introduction

As mentioned in chapter 3, the Sipe theory has several drawbacks and limitations. Many of them are expected to be circumvented by using a numerical approach. To investigate the interaction of electromagnetic waves with rough surfaces, the FDTD method has been selected and presented in chapter 4. In this chapter, the FDTD method is used to calculate the absorbed energy below the rough surface of materials and the results are compared to the Sipe theory. Figure 5.1 illustrates the steps taken in this chapter. That is, using the FDTD method, the interaction of a plane wave with the rough surface is simulated, leading to an inhomogeneous energy absorption in the material. At the $z = 0$ plane, the absorbed energy is predicted in the frequency domain by the Sipe theory. Likewise, the FDTD method allows to calculate the absorbed energy in the same plane, which can be represented in the frequency domain using the Fourier transform. The results can be compared to the Sipe theory. This comparison is one of the main goals of this chapter. Additionally, the FDTD calculations are not limited to the $z = 0$ plane only, nor to the frequency domain.

It is impractical to compare the analytical and the numerical approaches for all combinations of wavelengths, optical properties and rough surfaces. Therefore, the first part of this chapter is dedicated to define the parameters for which the

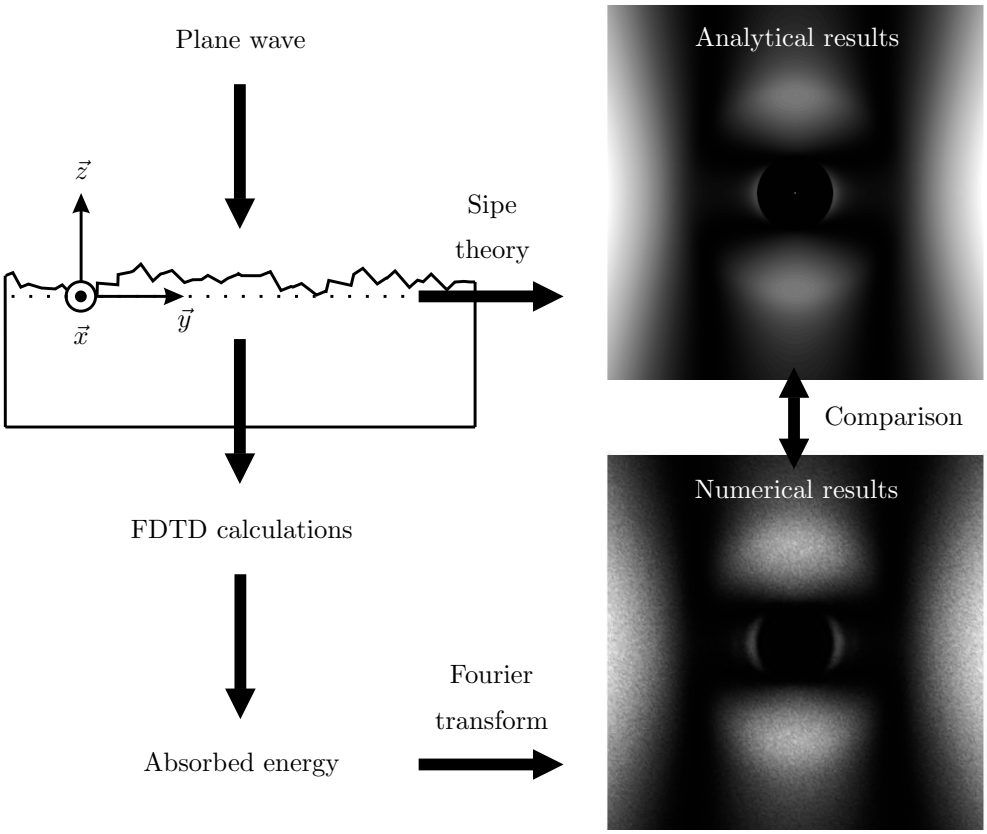

Figure 5.1: The steps taken in this chapter in order to compare the numerical results to the Sipe theory.

numerical results from the FDTD method are compared to the Sipe theory. Using these parameters, the second part deals with the comparison of the Sipe theory and the FDTD results. Finally, the advantages of the FDTD method and new insights derived from it, are discussed in the third part.

5.2 Simulation parameters

In this section, the simulation parameters used for the comparison of the numerical and analytical approach are defined: the source term, the optical properties of the medium, the dimensions of the Yee grid and the rough surfaces.

5.2.1 Source term

As discussed in chapter 4, and as listed in Table 2.4 on 14 and Table 3.1 on page 27, the LIPSSs of interest in this thesis are produced with linearly polarized radiation arriving at normal incidence on the surface of materials. Since isotropic rough surfaces are concerned in this chapter, it is always possible to assume that the light is polarized along the $\vec{x}$ axis. Therefore, the plane wave introduced in the simulation domain for the FDTD calculations is the one described in section 4.4.1. That is, a plane wave of wavelength λ, polarized in the $\vec{x}$ direction and traveling in the $\vec{z}$ direction. It is also what was used to compute the η maps of Figure 3.4 on page 22. Besides the angle of incidence $\theta = 0$ and the polarization direction, the wavelength selected for the comparison is logically $\lambda = 800\,\text{nm}$ since most femtosecond laser sources operate at this wavelength.

5.2.2 Optical properties

The optical properties used for the comparison are based on the Drude model proposed by Bonse et al. [58]. As mentioned in chapter 2, the Sipe theory has been combined with a Drude model to take into account, qualitatively, intra-pulse feedback mechanisms when a laser beam strikes a silicon sample. In the framework of this approach, the optical properties of excited silicon are described by the complex permittivity $\tilde{\varepsilon}_r^* = \tilde{\varepsilon}_r + \Delta\tilde{\varepsilon}_{\text{Drude}}$, as discussed in section 4.2.5. For the sake of convenience, the expression of $\Delta\tilde{\varepsilon}_{\text{Drude}}$ is recalled here

$$\Delta\tilde{\varepsilon}_{\text{Drude}} = -\frac{N_e e^2}{\varepsilon_0 m_{\text{eff}}\left(\omega^2 + j\gamma\omega\right)} = -\frac{\omega_p^2}{\omega^2 + j\gamma\omega}, \tag{5.1}$$

in which e, N_e, m_{eff}, ω and γ are respectively the electron charge, the electron density in the conduction band, the optical effective mass of the carriers, the angular frequency of the laser radiation, and the characteristic frequency of the electron collisions. The values of $m_{\text{eff}} = m_e m_{\text{opt}}$ and $\gamma = 1/\tau_{\text{Drude}}$ are calculated from the values of m_{opt} and τ_{Drude} given in the article of Bonse et al. [58]. That is, $m_{\text{opt}} = 0.18$ and $\tau_{\text{Drude}} = 1.1\,\text{fs}$. The complex refractive index of excited silicon is simply given by $\tilde{n}^* = \sqrt{\tilde{\varepsilon}_r^*}$ and depicted in Figure 5.2 as a function of the electron density in the conduction band N_e.

For the FDTD calculations, two distinct parts of this graph have to be considered. First, when $\text{Re}\left(\tilde{n}^*\right) > \text{Im}\left(\tilde{n}^*\right)$ the material can be considered non-dispersive, like it is assumed in the Sipe theory, because $\text{Re}\left(\tilde{\varepsilon}_r^*\right) = \varepsilon_r^* = \text{Re}\left(\tilde{n}^*\right)^2 - \text{Im}\left(\tilde{n}^*\right)^2$ is positive. In that case, the FDTD algorithm is stable and σ^* is calculated based on $\tilde{n}^*$ via $\sigma^* = 2\varepsilon_0\omega\text{Re}\left(\tilde{n}^*\right)\text{Im}\left(\tilde{n}^*\right)$, as explained in chapter 4. However, when $\text{Re}\left(\tilde{n}^*\right) \leq \text{Im}\left(\tilde{n}^*\right)$, $\text{Re}\left(\tilde{\varepsilon}_r^*\right)$ would be negative in the non-dispersive case. Therefore, the FDTD calculations for Drude dispersive media are used to ensure the stability of the algorithm.

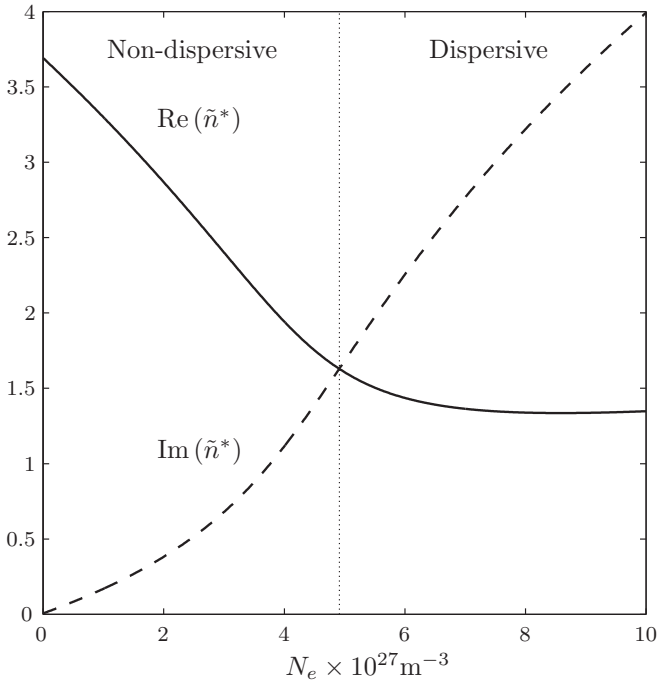

Figure 5.2: Real part $\mathrm{Re}\,(\tilde{n}^*)$ and imaginary part $\mathrm{Im}\,(\tilde{n}^*)$ of the complex refractive index of excited silicon $\tilde{n}^*$, for different electron densities N_e in the conduction band.

5.2.3 Space and time increments

The space increments Δx, Δy and Δz are chosen depending on the smallest wavelength traveling in the simulation domain and the smallest detail needed to be resolved. In addition, the space increments cannot be too small because several periods of LIPSSs need to be contained in the simulation domain, while the available resources, in terms of computer memory, are limited. The smallest wavelength traveling in the simulation domain is given by $\lambda/\mathrm{Re}\,(\tilde{n}^*)$, when $\mathrm{Re}\,(\tilde{n}^*)$ is at its maximum. That is, $\mathrm{Re}\,(\tilde{n}^*) = 3.692$ and $\lambda/\mathrm{Re}\,(\tilde{n}^*) \approx 217\,\mathrm{nm}$. As mentioned in section 4.3.4, a minimum of 10 cells per wavelength leads to accurate results. Hence, $\Delta x = \Delta y = 20\,\mathrm{nm}$ satisfies the above mentioned conditions. In the $\vec{z}$ direction, a finer grid is necessary to investigate the absorbed energy just below rough surfaces. Therefore $\Delta z = 5\,\mathrm{nm}$ was chosen.

Once the space increments are defined, the time increment must satisfy the stability criteria $\Delta t < \Delta t_{\max}$, with $\Delta t_{\max}$ being calculated based on equation (4.59). That is, $\Delta t_{\max} \approx 1.57\,\mathrm{fs}$. Hence, $\Delta t = 1.5\,\mathrm{fs}$ is valid and is used throughout this chapter.

5.2.4 Rough surfaces

For a valid comparison, similar rough surfaces as defined in the Sipe theory need to be used for the FDTD calculations. Although it is not possible to have rough surfaces identical to the ones described in the Sipe theory, due to the staircase approximation involved in the Yee algorithm, the main requirements used by Sipe et al. can be followed [13]. These requirements have already been discussed in section 3.2, but are recalled here for convenience. First, the height of the rough surfaces is small compared to the wavelength of the incident laser light. Second, the rough surfaces are isotropic. Finally, the rough surfaces are random, only characterized by binary functions defining the filled parts of the selvedge. While, the first two requirements are easily satisfied, the last one is more difficult. Indeed, to perform FDTD calculations, a well defined rough surface is required. However, the solution provided by Sipe et al. is an average for rough surfaces defined statistically. To enable the comparison between the two approaches, FDTD calculations are performed for a set of random rough surfaces instead of only a single rough surface. Then, the results of this set are averaged in the frequency domain, to allow the comparison to the Sipe theory.

To create a random rough surface for the FDTD calculations, a binary function is used to define the "presence" of material. At and below the $z = 0$ plane, the presence of material is assumed everywhere. For the plane just above $z = 0$, the Yee cell properties alternate between the optical properties of the medium and the optical properties of vacuum, depending on the value of the binary function. By considering one layer of Yee cells just above the $z = 0$ plane, the maximum height of the rough surface is controlled and kept small compared to the incident laser radiation ($\Delta z \ll \lambda$). To assure the isotropy of the rough surface, random numbers are generated to determine when the binary function is equal to 0 or 1. As explained in section 3.2, the rough surfaces used in the Sipe theory are defined by the couple (F, s), which is usually chosen as $(0.1, 0.4)$. While the shape factor s cannot be controlled correctly for the FDTD calculations, due to the staircase approximation in the Yee algorithm, it is possible to control the filling factor F. Indeed, when the random numbers are generated, it is possible to control the number of zeros and ones to have an average of 0.1. In addition, it is worth recalling that the couple (F, s) does not influence the position of the peaks in the η maps when $\theta = 0$ [5]. Hence, the position of the dominant frequencies can be compared without bias between the FDTD calculations and the Sipe theory. In the frame of this comparison, a set of 100 different rough surfaces was generated and used for the FDTD calculations. Using more than 100 rough surfaces was not improving the results significantly.

5.3 Comparison of the numerical and analytical approaches

The simulation parameters have been defined in the previous section to enable the comparison between the numerical and analytical approaches. In this section, the simulation domain is presented first, including the required FDTD features discussed

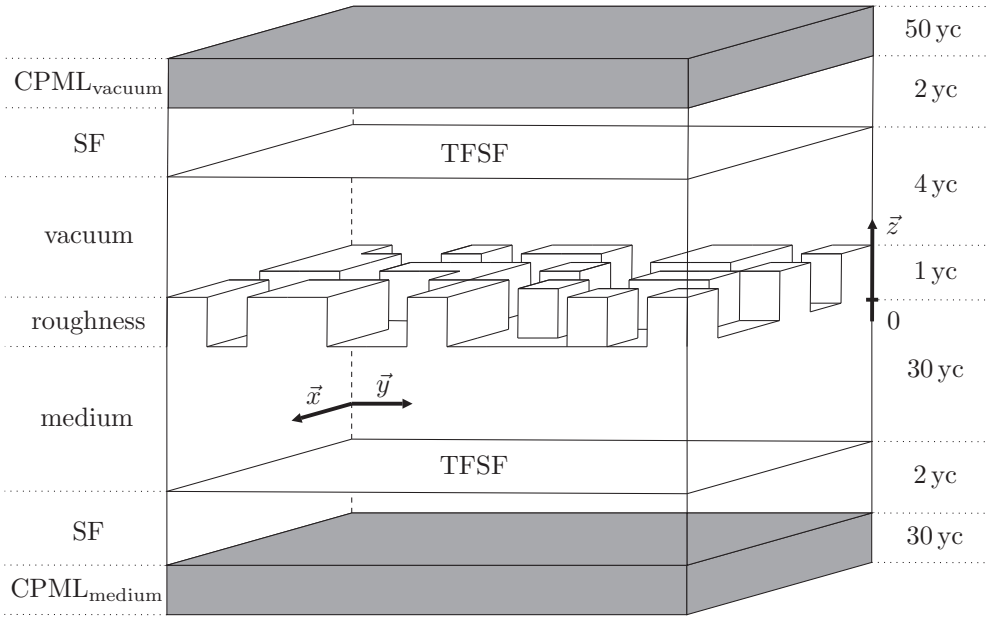

Figure 5.3: Schematic drawing of the simulation domain. The drawing is not to scale. The dimensions are indicated on the right side in terms of number of Yee cells (yc).

in chapter 4. Next, a result, i.e. an example of absorbed energy profile, is presented in order to confirm the need of a set of rough surfaces. Finally, the results of the FDTD calculations are compared to the Sipe theory.

5.3.1 Simulation domain

In Figure 5.3, the simulation domain used for the FDTD calculations is shown schematically. Above the rough surface which has a thickness of one Yee cell, there is vacuum, while for $z \leq 0$ the medium occupies the space. Both the vacuum and the medium are supposed to be infinitely extended in the $\vec{z}$ direction. This is achieved thanks to the CPML$_{\text{vacuum}}$ and CPML$_{\text{medium}}$ layers respectively (gray rectangles). Periodic boundary conditions are used in the $\vec{x}$ and $\vec{y}$ directions. In addition, the domain is separated into the total-field (TF) region, in between the TFSF planes, and the scattered field (SF) regions in order to introduce the plane wave in the simulation domain.

As mentioned in the previous section, the rough surface is only one Yee cell thick. The medium region, without considering the SF part, is 30 cell thick. Although it is not useful to have $30 \times 5\,\text{nm} = 150\,\text{nm}$ of material below the rough surface for the comparison to the Sipe theory, it was chosen to investigate how the

different frequencies evolve with z, which will be discussed in part 5.4. The region above the rough surface and the SF regions occupy a small space in the simulation domain, because these regions are of no interest in this thesis. The $\text{CPML}_{\text{vacuum}}$ and $\text{CPML}_{\text{medium}}$ are 50 and 30 Yee cell thick respectively. The numbers of Yee cells dedicated to the CPMLs were chosen empirically, in order to minimize the numerical errors while keeping the computational demands reasonable. Similarly, the coefficients ξ and ρ related to the CPML, defined in chapter 4, were tuned depending on the thickness of the CPML and the other simulation parameters.

5.3.2 Example of absorbed energy spectrum

FDTD calculations have been performed with the parameters mentioned above, for one single rough surface, to study the absorbed energy profile in the $z = 0$ plane. The Fourier transform of the absorbed energy profile is shown in Figure 5.4(a). As for the η maps in chapter 3, the vector $\vec{k} = (k_x, k_y)$ spanning the frequency domain is normalized by the norm of the wave vector, $2\pi/\lambda$. The optical properties used for the computation were $\tilde{n} = 3.692 + 0.0065j$. That is, the optical properties of silicon at room temperature for $\lambda = 800\,\text{nm}$, which corresponds to $N_e = 0\ \text{m}^{-3}$ in Figure 5.2. It is worth noting that $N_e = 0\ \text{m}^{-3}$ does not mean that there is no free carriers in the material, but that the contribution of the existing free carriers to the modification of the optical properties of the material, in the framework of the Drude model, is negligible. The corresponding η map, according to the Sipe theory, was computed with the same conditions and is shown in Figure 5.4(b) to allow comparison.

Although the spectrum obtained after one FDTD simulation is noisy, see Figure 5.4(a), it is possible to identify type-d features at the same location (in terms of frequencies) as in the η map. This is of importance since the existence of these frequencies has been predicted only in the Sipe theory. Hence, type-d features are not artifacts of the Sipe theory and its approximations, but "real" frequencies which can be responsible for LIPSS formation, as proposed by Wu et al. for example [27]. The type-s features are harder to distinguish around the $\|\vec{k}\| = 1$ circle in Figure 5.4(a). An averaged solution, based on a set of 100 rough surfaces, is required to identify this type of features with certainty. The averaged solutions, computed via the FDTD method, will be referred to as FDTD-η map in this thesis.

5.3.3 FDTD-η maps

In Figure 5.5 and 5.6, the results of the averaged FDTD simulations are presented and compared to the Sipe theory. Figure 5.5 contains the results of calculations performed when $\text{Re}\,(\tilde{n}^*) > \text{Im}\,(\tilde{n}^*)$, while Figure 5.6 concerns $\text{Re}\,(\tilde{n}^*) < \text{Im}\,(\tilde{n}^*)$. The FDTD-$\eta$ maps and the η maps are shown in the left and right columns, respectively. To ease the comparison, isolines in the FDTD-η maps and the η maps are represented. That is, the black regions indicate frequency values between 0 and 25% of the maximum of the map, the dark gray regions values between 25 and 50%, the light gray regions values between 50 and 75% and the white regions values between 75 and 100% .

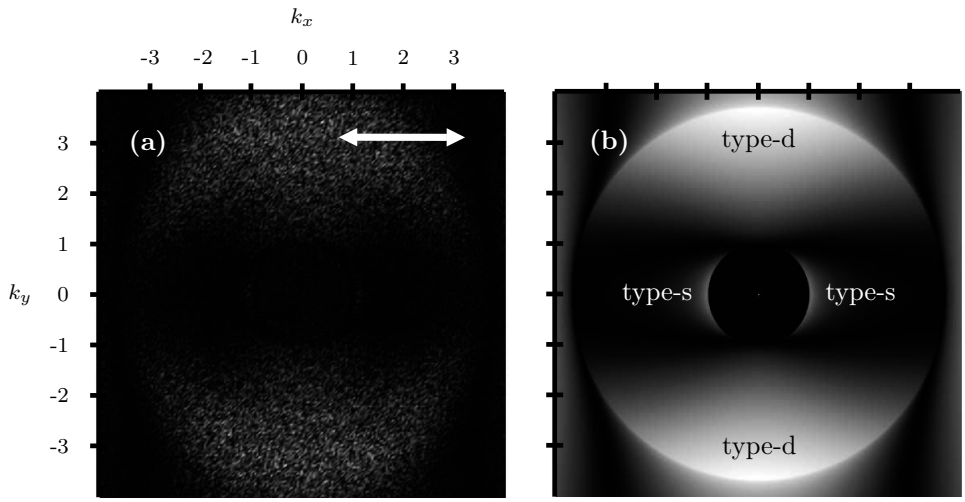

Figure 5.4: (a) Frequency spectrum of the absorbed energy in the $z = 0$ plane, obtained via FDTD calculations, and (b) the corresponding η map. Simulation parameters: $\lambda = 800\,\text{nm}$ and $\tilde{n} = 3.692 + 0.0065j$. The polarization direction is indicated by the white arrow. The frequency domain is normalized by the norm of the wave vector, $2\pi/\lambda$.

In comparison to Figure 5.4, the resemblance between the Sipe theory and the FDTD calculations is more apparent due to the averaging over 100 rough surfaces. In Figure 5.5(a), the type-s features can be observed even though they are not as pronounced as in the Sipe theory. In addition, the presence of the type-d features is again confirmed. In both kind of maps, the evolution of the different features as a function of N_e follows the same trend. That is, in Figure 5.5, the type-s features become larger with increasing N_e, while the type-d features tend to disappear progressively. Interestingly, frequencies at $\|k_x\| \approx 3$ to 4 appear in Figures 5.5(c-f). These features of the maps are referred to as type-r features in this thesis. The letter "r" refers to "roughness" as explained in section 5.4, in which the type-r features are discussed extensively. As mentioned in chapter 3, the Sipe theory does not handle features at high frequencies correctly, however, the agreement between the FDTD-η maps and the η maps regarding the type-r features is remarkable for $\|k_x\| \leq 4$. It is worth noting that the type-s, type-d and type-r notations are useful for the discussion, but can become ambiguous, as is illustrated by Figure 5.5(e). Indeed, the type-s and type-r features merge and a clear distinction is therefore difficult. One difference between the FDTD-η and the η maps is visible in Figure 5.5(e), where frequencies are visible for $\|\vec{k}\| < 1$. While the amplitude of these frequencies is small compared to the type-s or the type-r features, these frequencies are nonetheless important from a theoretical point of view since they correspond to periodicities larger than the laser wavelength ($\Lambda > \lambda$). They are referred to as type-g features in

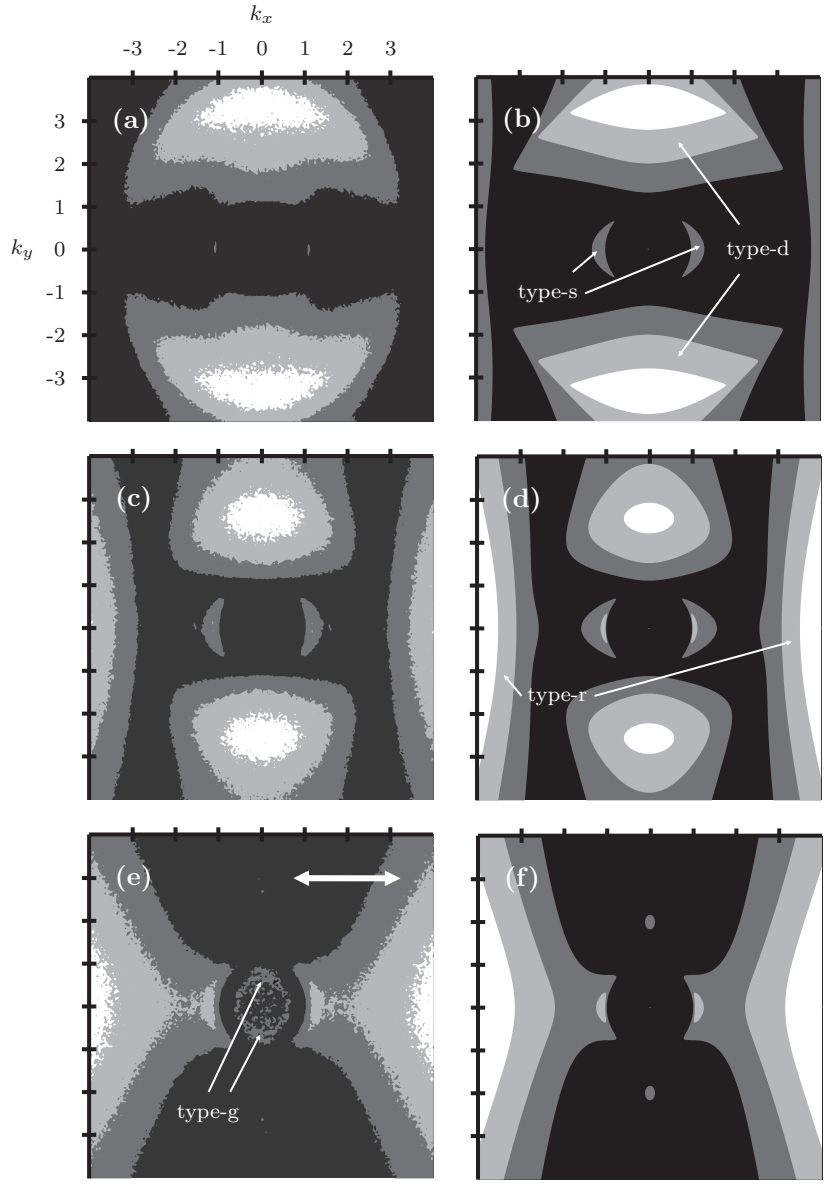

Figure 5.5: FDTD-η maps (left column) and η maps (right column) computed with the parameters defined in section 5.2 and the simulation domain described in section 5.3.1. (a,b) $N_e = 0$ m^{-3}, $\tilde{n} = 3.692 + 0.0065j$. (c,d) $N_e = 2 \times 10^{27}$ m^{-3}, $\tilde{n}^* = 2.868 + 0.382j$. (e,f) $N_e = 4 \times 10^{27}$ m^{-3}, $\tilde{n}^* = 1.943 + 1.116j$. The polarization direction is indicated by the white arrow.

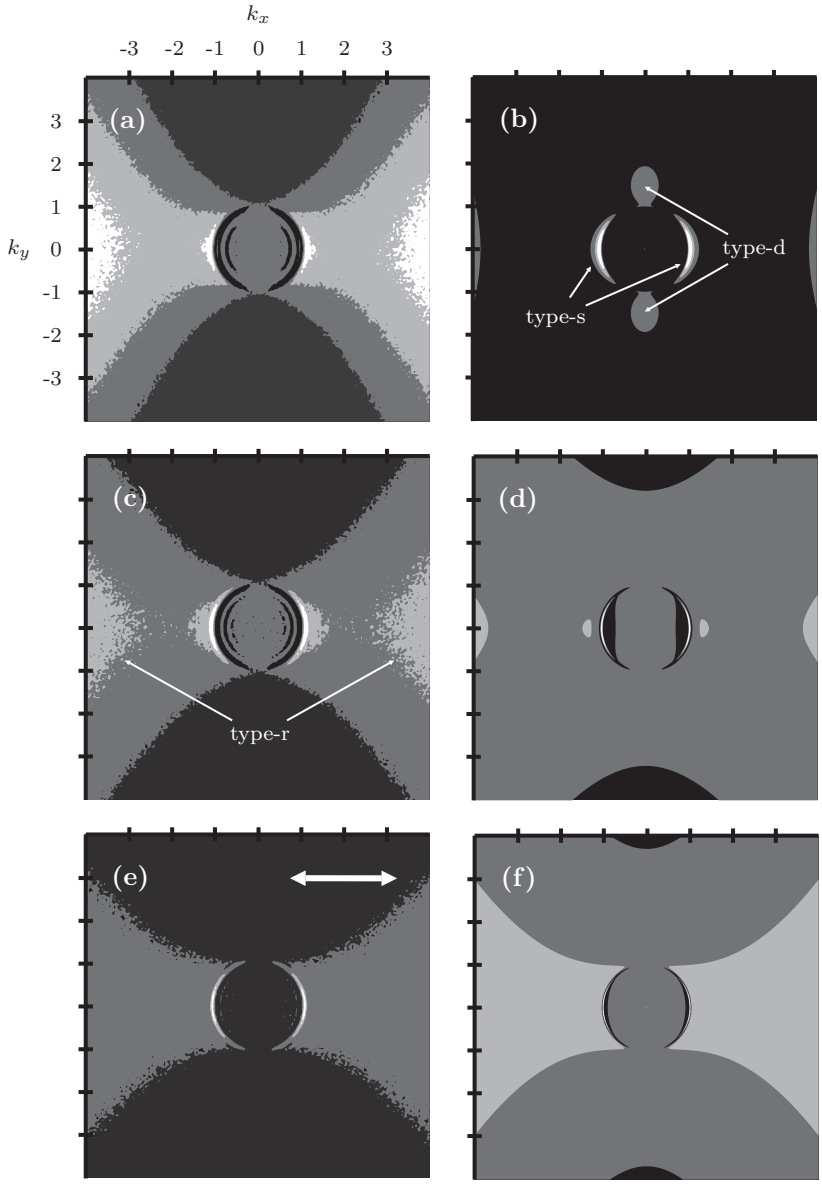

Figure 5.6: FDTD-η maps (left column) and η maps (right column) computed with the parameters defined in section 5.2 and the simulation domain described in section 5.3.1. (a,b) $N_e = 6 \times 10^{27}$ m^{-3}, $\tilde{n}^* = 1.436 + 2.255j$. (c,d) $N_e = 8 \times 10^{27}$ m^{-3}, $\tilde{n}^* = 1.339 + 3.220j$. (e,f) $N_e = 10 \times 10^{27}$ m^{-3}, $\tilde{n}^* = 1.348 + 3.993j$. The polarization direction is indicated by the white arrow.

this thesis, where "g" stands for "grooves". If grooves form, their spectrum shows frequencies within the $\|\vec{k}\| < 1$ disk [39], therefore the notation follows naturally.

For LIPSS formation, the interpretation of Figure 5.5 is straightforward if the type-r features are disregarded. In this case, if LIPSSs form according to the inhomogeneous energy absorption patterns, their characteristics should be defined by the type-d features and the type-s features at low ($N_e = 0$ m^{-3} and $N_e = 2 \times 10^{27}$ m^{-3}) and high excitations states ($N_e = 4 \times 10^{27}$ m^{-3}), respectively. That is, HSFLs parallel to the polarization of the laser light with a periodicity $\Lambda \approx \lambda/\mathrm{Re}\,(n^*)$ for the type-d features and LSFLs with $\Lambda < \lambda$ for the type-s features. LSFLs with a periodicity $\Lambda \approx \lambda$ are unlikely to form since the type-s features follow the outer part of the $\|\vec{k}\| = 1$ circle and are, in addition, spread in the frequency domain. The presence of type-r features makes the interpretation more complex since it affects the periodicity of LIPSSs in the direction orthogonal to the polarization. As explained in chapter 3, the Sipe theory is not valid for large values of $\|k_x\|$, therefore the characteristics of type-r features are discussed in section 5.4, where the advantages of the numerical approach are presented in more details. It is worth noting that this discussion started with "if LIPSSs form according to the inhomogeneous energy absorption patterns". Indeed, under certain conditions, such as being outside the adequate fluence regime for example, LIPSSs do not form. In the rest of this chapter, the FDTD-η maps are interpreted without recalling this statement, which is also the main assumption of the Sipe theory.

The agreement between the FDTD-η maps and the η maps is less apparent for the case where $\mathrm{Re}\,(n^*) < \mathrm{Im}\,(n^*)$, as shown in Figure 5.6. The main difference concerns the type-r features which are present in the FDTD-η maps, see Figures 5.6(a) and (c), while they are almost absent in the η maps, see Figure 5.6(b) and Figure 5.6(d). This difference is probably due to the limitations of the Sipe theory. Apart from the type-r features, the type-s features show a similar evolution with an increase of N_e in the FDTD-η maps and the η maps. That is, these features are more prominent at the $\|\vec{k}\| = 1$ circle and are less spread in the frequency domain. Hence, a higher excitation leads to a periodicity of LSFLs closer to the wavelength of the incident laser light and to more regular LSFLs in the space domain. As explained in chapter 3, type-s features are related to SPPs when $\mathrm{Re}\,(n^*) < \mathrm{Im}\,(n^*)$ and can account for the properties of LSFLs with a good accuracy [37, 58]. However, the role of the type-r features needs to be clarified to allow conclusions on the cause of LSFL formation, and their variation of periodicity.

5.4 Advantages of the numerical approach

As mentioned in chapter 3, the assumptions and approximations of the Sipe theory limit the interpretation of the η maps to frequencies of relatively small $\|\vec{k}\|$. It was shown in the previous section that the type-r features, present at large $\|k_x\|$, are of importance. Indeed, it is crucial to understand their role and how they influence the effect of the type-s and type-d features in the space domain. In this section the advantages of the numerical approach over the analytical approach of Sipe are

discussed. First, the depth dependence of the FDTD-η maps is investigated, including the evolution of the type-r properties as a function of z. Next, space domain results are shown and analyzed with the knowledge derived from the frequency maps.

5.4.1 Depth dependence of the FDTD-η maps

FDTD calculations allow to study the depth dependence of the absorbed energy spectrum. An example of the evolution of the FDTD-η maps as a function of z, for $N_e = 3 \times 10^{27}$ m^{-3}, is shown in Figure 5.7. Instead of using z, which is always negative below the rough surface (see Figure 5.3), the depth $\delta = -z$ is used. The FDTD-η maps have been drawn using the isolines defined in section 5.3.3. It should be noted that different scales have been used for Figures 5.7(a-c), Figures 5.7(d-f) and Figures 5.7(g-i).

Figure 5.7(a) is similar to an η map when analyzing high frequencies. That is, no type-s or type-d features can be observed, because their amplitudes are smaller than 25% (first isoline) of the maximum amplitude of the type-r features. Surprisingly, the $\delta = 0$ nm case seems of little interest to explain LIPSS formation while all the calculations of the Sipe theory were made for that depth. Besides $\delta = 0$ nm, the type-r features are strongly depth dependent. That is, they depend significantly on the distance δ from the rough surface, and tend to disappear when δ is large. Therefore, the "r" letter was chosen for "roughness". The evolution on the type-r features follows mainly two trends when δ is increasing, from Figure 5.7(a) to Figure 5.7(i). First, their position in the frequency domain shifts progressively towards the center $\|\vec{k}\| = 0$ of the map. Secondly, their amplitude decreases. These two trends combined makes the type-r features merge with the type-s features, until they disappear at about $\delta = 70$ nm. Apart from their "fusion" with the type-r features, the shape and amplitude of the type-s features are almost constant, as shown in Figure 5.7(d) to Figure 5.7(i), except for the first 20 nm of depth, in Figure 5.7(a) to Figure 5.7(c). Here the type-r features are concealing the presence of any other frequency. Similarly, the type-d features are also showing little, i.e. gradual, variations with the depth. Their position shifts slightly towards the center of the FDTD-η maps and their amplitude increases slowly.

In the previous section, the type-r features were disregarded while interpreting the FDTD-η maps for LIPSS formation. Although disregarding the type-r features seems to be a correct approximation for $\delta \geq 50$ nm, Figures 5.7(a-e) shows that the problem is, in general, more complex. Even without a strong presence of the type-r features, predicting what kind of LIPSS form from an FDTD-η map can be difficult. Indeed, the type-s and type-d features do "compete" in terms of amplitude, as can be observed from Figure 5.7(f) to Figure 5.7(i), and conclusions about the presence of LSFLs or HSFLs cannot be drawn. The space domain analysis may reveal which feature is dominant. For $\delta \leq 50$ nm, the type-r features cannot be neglected. As mentioned in chapter 3, if HSFLs orthogonal to the polarization are a consequence of the interaction of electromagnetic waves with rough surfaces, the absorbed energy spectrum should show a preferential energy absorption for large k_x, which is exactly what is observed here. Moreover, with increasing depth, the position of the type-r

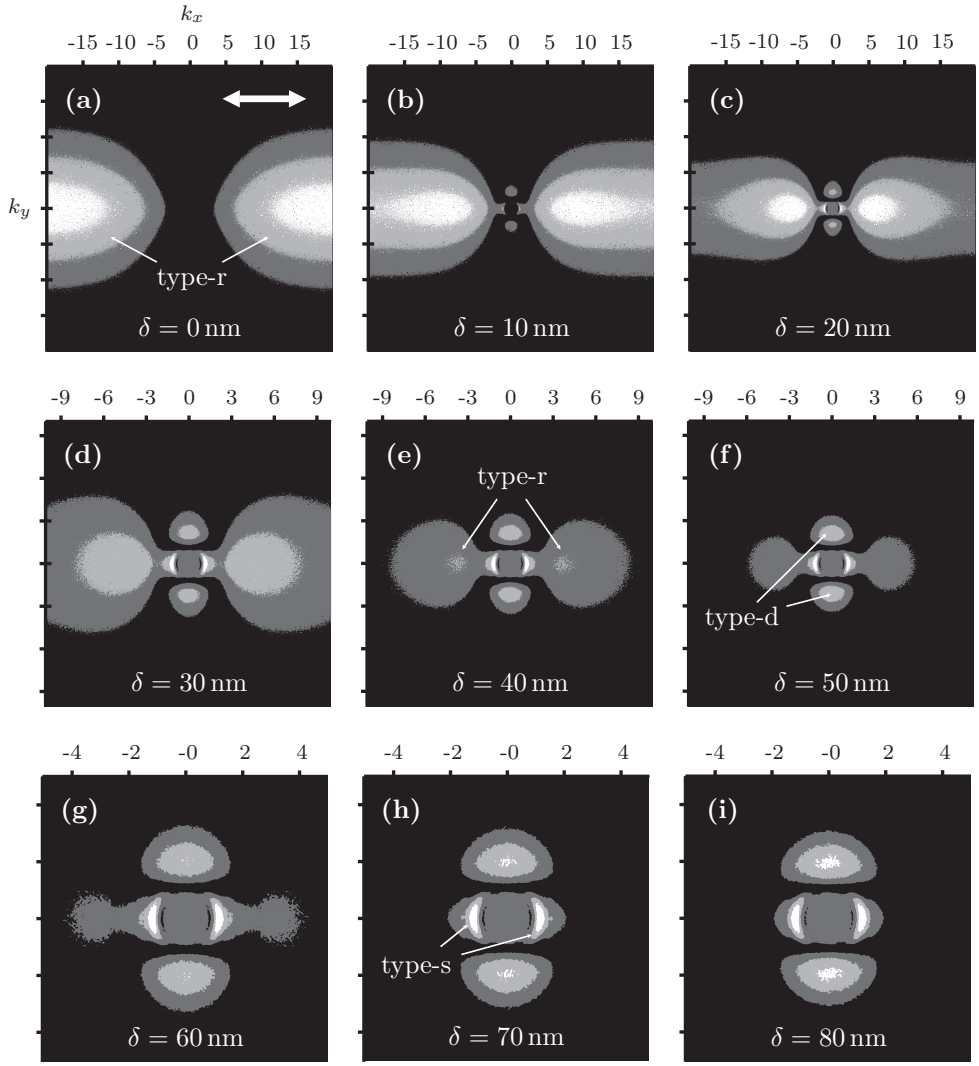

Figure 5.7: FDTD-η maps computed with the parameters defined in section 5.2 and the simulation domain described in section 5.3.1. The optical properties are calculated with $N_e = 3 \times 10^{27}$ m^{-3}, which leads to $\tilde{n}^* = 2.401 + 0.679j$. Note that different scales have been used for (a-c), (d-f) and (g-i). The polarization direction is indicated by the white arrow. The vertical scale is identical to the horizontal scale.

maximum amplitude decreases from $k_x \approx 16$ in Figure 5.7(a) up to $k_x \approx 4$ in Figure 5.7(e). These frequencies would lead to HSFLs orthogonal to the polarization with a periodicity in the range of $0.06\lambda \leq \Lambda \leq 0.25\lambda$, which is in agreement with Table 2.3 on page 10. This discussion shows that the type-r features can explain the formation of HSFLs orthogonal to the laser polarization. However, it is unclear which LIPSSs will form since the type-s, type-d and type-r features are competing at different depths δ and at different densities of electrons in the conduction band N_e. Qualitatively, HSFLs orthogonal to the polarization should form for physical processes occurring in the first tens of nanometers below the rough surface, since it is where the type-r features are present in the FDTD-η maps. Hence, they are more likely to grow for low fluences leading to small effects in the outer surface.

So far the depth dependence of the FDTD-η map features has been presented for $N_e = 3\times10^{27}$ m^{-3}. For the sake of concision, figures equivalent to Figure 5.7 for other values of N_e are not included in this thesis. Instead, the depth dependence of the FDTD-η is discussed on the basis of Figure 5.8 and Figure 5.9 for $\mathrm{Re}\,(\tilde{n}^*) > \mathrm{Im}\,(\tilde{n}^*)$ and $\mathrm{Re}\,(\tilde{n}^*) < \mathrm{Im}\,(\tilde{n}^*)$, respectively. Before analyzing these graphs in details, several points need to be raised. First, Figure 5.8 and Figure 5.9 concern only type-r features since they are the only features of the FDTD-η maps showing significant variations with δ. Second, the data needed to draw the graphs in Figure 5.8 is extracted from the frequencies of the FDTD-η maps above the 75% isoline (white color), while the 50% isoline (light gray color) was taken for Figure 5.9. To achieve the first point, only the frequencies with $k_x > \mathrm{Re}\,(\tilde{n}^*)$ are considered. Indeed, if this last consideration was not taken into account, the type-s features and the type-d features would be included in any calculations while only the type-r features are of interest here. It is worth noting that this distinction, between frequencies higher or lower than $k_x = \mathrm{Re}\,(\tilde{n}^*)$, is not arbitrary. In Figures 5.7(c-g), a clear separation between the type-s and type-r features can be observed for $k_x = \mathrm{Re}\,(\tilde{n}^*) = 2.401$. Mathematically, the frequencies of interest in Figure 5.8 belong to the domain $\Omega_{\delta,\mathrm{N_e}}$, defined by

$$\Omega_{\delta,\mathrm{N_e}} = \left\{ \begin{array}{l} \vec{k} = (k_x, k_y) \\ \\ k_x > \mathrm{Re}\,(\tilde{n}^*) \\ \\ f_{\delta,\mathrm{N_e}}\left(\vec{k}\right) \geq 0.75\,\mathrm{M}_{\delta,\mathrm{N_e}} \end{array} \right\}. \tag{5.2}$$

These frequencies are identified by the vector $\vec{k} = (k_x, k_y)$ spanning the frequency domain, normalized by the norm of the incident wave vector, $2\pi/\lambda$. Further, $f_{\delta,\mathrm{N_e}}(\vec{k})$ refers to the amplitude of the frequency of the FDTD-η map located at $\vec{k}$, computed for a certain N_e and δ, while $\mathrm{M}_{\delta,\mathrm{N_e}}$ is the maximum of this map. In the case of Figure 5.9, the domain is similar to $\Omega_{\delta,\mathrm{N_e}}$, except that 0.5 was used instead of 0.75 since the 50% isoline was considered.

For further analysis, the frequencies in the domain $\Omega_{\delta,\mathrm{N_e}}$ are characterized by their weighted arithmetic mean $\mathrm{W}_{\delta,\mathrm{N_e}}$ and the area they cover in the frequency domain $\mathrm{A}_{\delta,\mathrm{N_e}}$. $\mathrm{W}_{\delta,\mathrm{N_e}}$ is calculated as

$$\mathrm{W}_{\delta,\mathrm{N_e}} = \left(\sum_{\vec{k}\in\Omega_{\delta,\mathrm{N_e}}} f_{\delta,\mathrm{N_e}}\left(\vec{k}\right) \right)^{-1} \sum_{\vec{k}\in\Omega_{\delta,\mathrm{N_e}}} f_{\delta,\mathrm{N_e}}\left(\vec{k}\right) k_x, \tag{5.3}$$

which gives the location of the type-r features within the FDTD-η maps. It is worth noting that only k_x is of interest since the type-r features are symmetric for k_y. To help the reader understand the quantity $\mathrm{W}_{\delta,\mathrm{N_e}}$, in Figure 5.7, it can be observed that the location of the type-r features is moving towards the center with increasing δ. Hence, $\mathrm{W}_{\delta,\mathrm{N_e}}$ will decrease with increasing δ, starting from $\mathrm{W}_{\delta,\mathrm{N_e}} \approx 16$ (large value of k_x), to reach $\mathrm{W}_{\delta,\mathrm{N_e}} = 0$ when the type-r features disappear. $\mathrm{A}_{\delta,\mathrm{N_e}}$ is defined as

$$\mathrm{A}_{\delta,\mathrm{N_e}} = \sum_{\vec{k}\in\Omega_{\delta,\mathrm{N_e}}} \Delta k_x \Delta k_y, \tag{5.4}$$

where Δk_x and Δk_y are the frequency domain increments. While the amplitude of the frequencies in $\Omega_{\delta,\mathrm{N_e}}$ are large, a significant $\mathrm{A}_{\delta,\mathrm{N_e}}$ is necessary to have an impact in the space domain. Hence, knowing the location of the type-r features is not enough and $\mathrm{A}_{\delta,\mathrm{N_e}}$ is also needed to discuss the role of the type-r features.

In Figure 5.8(a), the evolution of $\mathrm{W}_{\delta,\mathrm{N_e}}$ as a function of δ is presented for $N_e = 0$ m^{-3}, $N_e = 2 \times 10^{27}$ m^{-3} and $N_e = 4 \times 10^{27}$ m^{-3}. As for the type-r features for $N_e = 3 \times 10^{27}$ m^{-3}, presented in Figure 5.7, the location of the type-r features shifts towards the center of the FDTD-η maps until the they are concealed by the type-s or type-d features, which is indicated by $\mathrm{W}_{\delta,\mathrm{N_e}} = 0$ in this graph. The evolution $\mathrm{A}_{\delta,\mathrm{N_e}}$, shown in Figure 5.8(b), is also in accordance with what is observed in Figure 5.7. That is, the area covered by the type-r features in the frequency domain decreases with an increasing depth. The slight increase of $\mathrm{A}_{\delta,\mathrm{N_e}}$ at the beginning of the curve, for all N_e, is simply explained by studying Figure 5.7(a) and Figure 5.7(b). The frequencies in $\Omega_{\delta,\mathrm{N_e}}$ are truncated in Figure 5.7(a), while they are taken into account in Figure 5.7(b). From the two graphs presented in Figure 5.8, it can be concluded that the type-r features are more prominent when N_e is large, at least for the $\mathrm{Re}\,(\tilde{n}^*) > \mathrm{Im}\,(\tilde{n}^*)$ case. In addition, the depth should not be too large, $\delta < 40\,\mathrm{nm}$.

Before discussing the interpretation of the type-r features in the frame of LIPSS formation, the evolution of the type-r features as function of δ for the $\mathrm{Re}\,(\tilde{n}^*) < \mathrm{Im}\,(\tilde{n}^*)$ regime is shown in Figure 5.9. The solid, dashed and dotted curves are related to $N_e = 6 \times 10^{27}$ m^{-3}, $N_e = 8 \times 10^{27}$ m^{-3} and $N_e = 10 \times 10^{27}$ m^{-3}, respectively. The 50% isoline has been chosen to represent the type-r features since the frequencies of the 75% isoline are concealed by the type-s features rapidly with increasing depth. In contrary to Figure 5.8, the type-r features are prominent for low N_e. However, their charateristics as a function of δ are similar. That is, their location shifts to lower k_x and they occupy progressively smaller areas in the frequency domain. Interestingly, even when $\mathrm{A}_{\delta,\mathrm{N_e}} \approx 0$ for the solid and dashed curves, $\mathrm{W}_{\delta,\mathrm{N_e}} \neq 0$. This can be attributed to the fact that the main part of the type-r features is merged with the type-s features, but a small part remains at $k_x > \mathrm{Re}\,(\tilde{n}^*)$.

From all the information about the FDTD-η maps gathered in Figure 5.5 to Figure 5.9, LIPSS formation is complex, especially when the type-r features

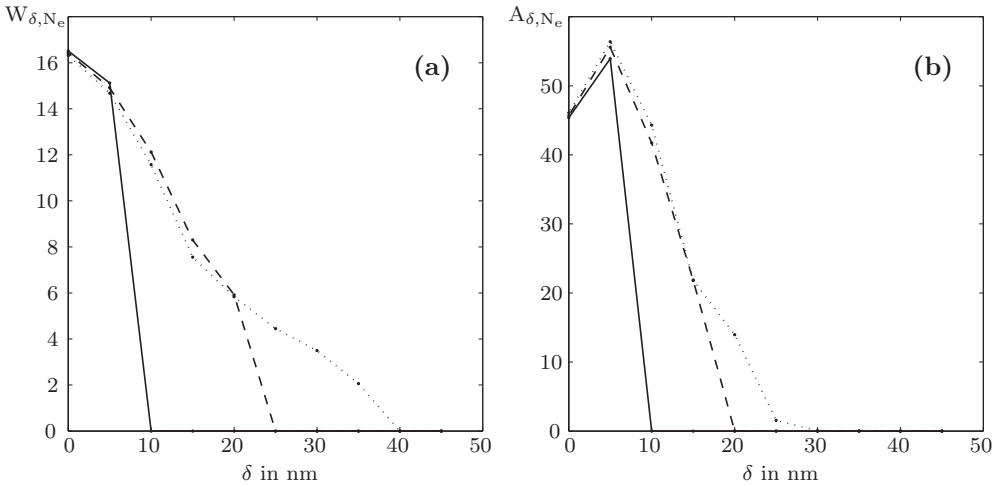

Figure 5.8: Evolution of W_{δ,N_e} (a) and A_{δ,N_e} (b) as a function of δ for $N_e = 0$ m^{-3}, $N_e = 2 \times 10^{27}$ m^{-3} and $N_e = 4 \times 10^{27}$ m^{-3}, which corresponds to the solid, dashed and dotted curves, respectively. For these values of N_e, $\mathrm{Re}(\tilde{n}^*) > \mathrm{Im}(\tilde{n}^*)$. The 75% isoline was considered to draw these graphs.

cannot be disregarded. However, when $\delta \gtrsim 50$ nm, the interpretation is almost straightforward. If LIPSSs are produced according to these FDTD-η maps, LSFLs or HSFLs parallel to the polarization should form, depending on the importance of the type-s and type-d features, respectively. For depths smaller than 50 nm, HSFLs orthogonal to the polarization could grow. However, their periodicity is hardly predictable since the location of the type-r features in the FDTD-η maps depends strongly on δ. This lack of deterministic properties is in agreement with Table 2.3 on 10, in which HSFLs show large variations of their periodicity. It is worth noting that if HSFLs orthogonal to the polarization form due to the presence of the type-r features, intermediate N_e are more favorable to their growth. That is, when the material is excited ($N_e \neq 0$ m^{-3}) but not when the SPPs are too pronounced in the frequency domain, via the type-s features. Qualitatively, HSFLs orthogonal to the polarization should grow at low fluence, where they compete with HSFLs parallel to the polarization when materials are transparent.

The results presented above were computed assuming constants optical properties and the intra-pulse feedback mechanisms were taken into account in the same manner as for the Sipe-Drude theory [58]. When semiconductors or dielectrics are excited, their optical properties change not only with time but also with the depth δ. Therefore, no quantitative conclusion can be drawn regarding the exact evolution of the characteristics of the frequency domain features. Instead, the trends and observations should serve as a guideline to interpret LIPSS formation.

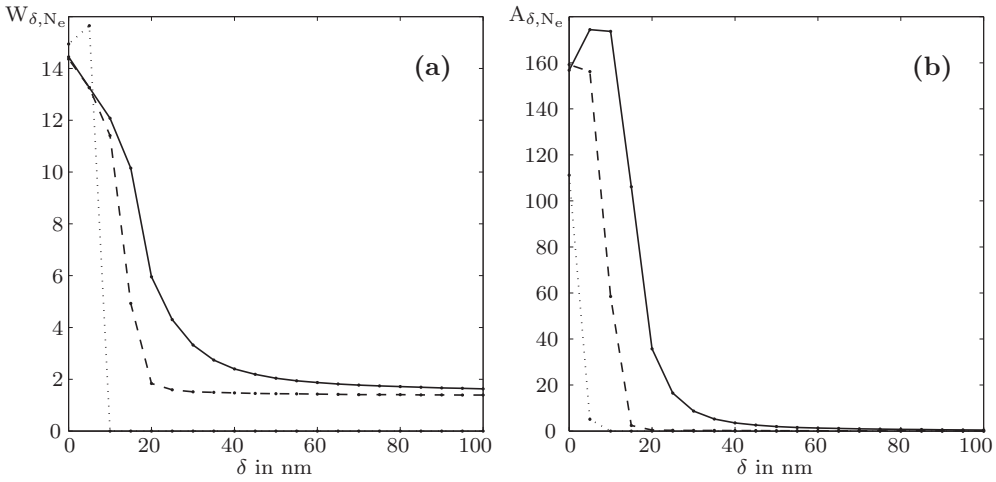

Figure 5.9: Evolution of W_{δ,N_e} (a) and A_{δ,N_e} (b) as a function of δ for $N_e = 6 \times 10^{27}$ m^{-3}, $N_e = 8 \times 10^{27}$ m^{-3} and $N_e = 10 \times 10^{27}$ m^{-3}, which corresponds to the solid, dashed and dotted curves, respectively. For these values of N_e, $\mathrm{Re}(\tilde{n}^*) < \mathrm{Im}(\tilde{n}^*)$. The 50% isoline was considered to draw these graphs.

5.4.2 Space domain results

One of the advantages of the FDTD method, when studying LIPSSs formation, is its ability to study space domain results. That is, the absorbed energy profile in the space domain. It allows to determine which of the frequency domain features is dominant, while this is not always clear from Sipe theory or from the FDTD-η maps.

In Figure 5.10, the absorbed energy profile for $N_e = 0$ m^{-3} and $N_e = 8 \times 10^{27}$ m^{-3} at $\delta = 0$ nm are shown. The absorbed energy has been calculated using one of the well defined random rough surfaces from the set of hundreds, described in section 5.2.4. From these calculations, involving a 20×20 μm^2 surface, a 5×5 μm^2 area was extracted to present the results. Top view representations of the absorbed energy, within that area, are drawn with a linear gray scale. The white and black colors are related to the high and low absorbed energies, respectively.

The "fingerprints" of the type-r features in the space domain are present in the form of small black "stripes", which have a preferential orientation orthogonal to the polarization of the laser radiation. To that respect, both Figure 5.10(a) and Figure 5.10(b) are representative of the type-r expression in the space domain for $0 \leq N_e \leq 10 \times 10^{27}$ m^{-3}. In Figure 5.10(a), white stripes running more or less parallel to the polarization of the laser radiation can be observed. This was expected since the type-d features were pronounced in Figure 5.5(a) on page 59. Surprisingly, thin stripes running parallel to the polarization of the laser radiation are also visible in Figure 5.10(b) (highlighted by few white marks), while no type-d features were

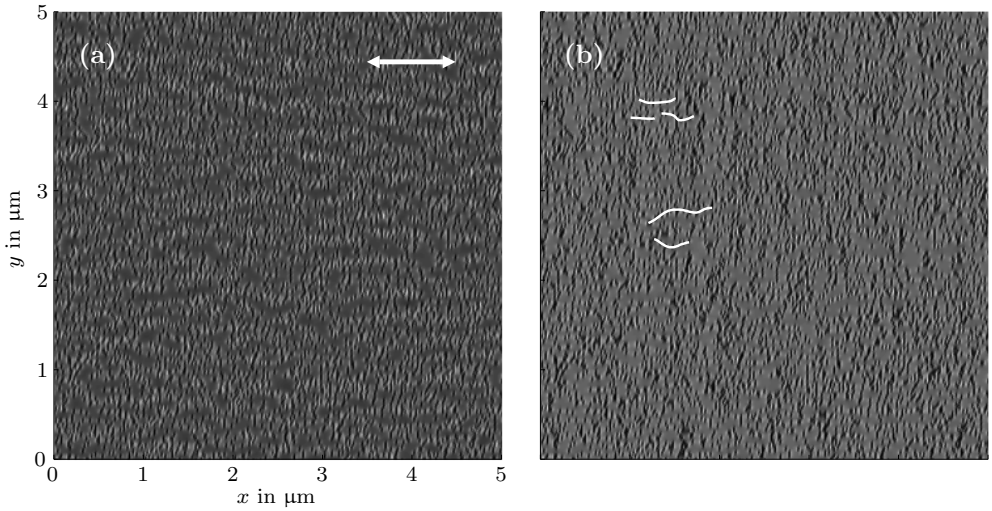

Figure 5.10: 5×5 µm^2 top view representations of the absorbed energy profile just below a random rough surface, $\delta = 0$ nm, for (a) $N_e = 0$ m^{-3} and (b) $N_e = 8 \times 10^{27}$ m^{-3}. The polarization direction is indicated by the white arrow.

visible for $N_e = 8 \times 10^{27}$ m^{-3}, see Figure 5.6(c). In fact, the type-d features are present, but concealed by the other frequencies. This phenomenon is interesting since HSFLs parallel to the polarization are expected to develop on metals, for example on alloyed steel or titanium as indicated in Table 2.3 on page 10. It is worth noting that close to the surface, $\delta = 0$ nm, only features possibly related to HSFLs are observable.

In Figure 5.11 and Figure 5.12, 10×10 µm^2 top view representations of the absorbed energy at 50 nm and 75 nm below a random rough surface are shown in the left and right column, respectively, for different N_e. Figure 5.11 is discussed first and concerns $N_e = 0$ m^{-3}, $N_e = 2 \times 10^{27}$ m^{-3} and $N_e = 3 \times 10^{27}$ m^{-3}. The linear gray scale color map has been abandoned because of the poor contrast it offers, instead, a color map ranging from blue to red for the smallest to the largest value, respectively, is used. As can be observed, the energy profiles for $N_e = 0$ m^{-3} in Figure 5.11(a) and Figure 5.11(b) are similar. A periodic energy absorption, with a periodicity $\Lambda \approx 285$ nm and a preferential direction parallel to the polarization of the laser light, can be observed. The periodicity is larger than the one predicted by analyzing the type-d features of the η map, which predicts $\Lambda = \lambda/\mathrm{Re}\,(\tilde{n}) \approx 217$ nm, and of the FDTD-η map at $\delta = 0$ nm, which predicts $\Lambda \approx 240$ nm. This larger periodicity is due to the depth dependence of the type-d features, as discussed in section 5.4.1. With increasing depth, their location shifts progressively towards the center of the FDTD-η maps, leading to larger periodicities. No differences can be observed between Figure 5.11(a) and Figure 5.11(b) since the type-r features are already negligible for $\delta = 50$ nm.

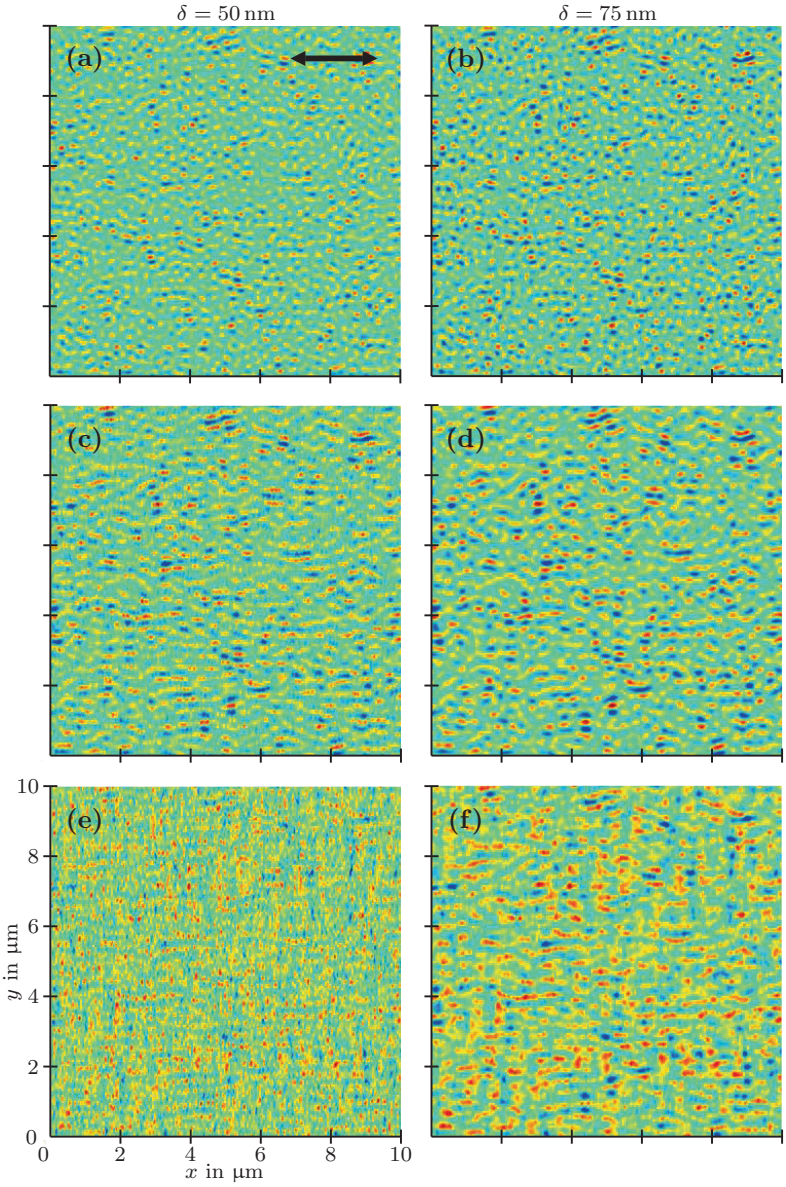

Figure 5.11: 10×10 µm^2 top view representations of the absorbed energy 50 nm (left column) and 75 nm (right column) below a random rough surface, for (a-b) $N_e = 0$ m^{-3}, (c-d) $N_e = 2 \times 10^{27}$ m^{-3} and (e-f) $N_e = 3 \times 10^{27}$ m^{-3}. The polarization direction is indicated by the black arrow. Each picture is shown with a color map ranging from blue to red for the smallest to the largest value, respectively.

For $N_e = 2 \times 10^{27}$ m^{-3}, that is in Figure 5.11(c) and Figure 5.11(d), a periodic energy absorption mostly parallel to the polarization of the laser radiation can be observed. Its periodicity, $\Lambda \approx 375$ nm, is also larger than what is expected from the η map, which predicts $\Lambda = \lambda/\mathrm{Re}\,(\tilde{n}) \approx 280$ nm, and from the FDTD-η map at $\delta = 0$ nm, which predicts $\Lambda \approx 305$ nm. This variation of periodicity has the same cause as for $N_e = 0$ m^{-3}, which is the depth dependence of the type-d features. A comparison of Figure 5.11(c) and Figure 5.11(d) reveals that the type-r features are not completely negligible for $\delta = 50$ nm. Indeed, small vertical stripes are interrupting the horizontal stripes of equal absorbed energies. One can notice that, the absorbed energy profile for $N_e = 2 \times 10^{27}$ m^{-3} along the polarization direction is more regular than for $N_e = 0$ m^{-3}. This observation seems in contradiction with the type-d features being more pronounced in the frequency domain at lower N_e. While being indeed more pronounced, the type-d features occupy mainly the frequency region between $\|\vec{k}\| = 1$ and $\|\vec{k}\| = \mathrm{Re}\,(\tilde{n}^*)$. Hence, they are more spread in the frequency domain for lower values of N_e, so less regular in the space domain.

As expected from the FDTD-η maps of Figure 5.7, the absorbed energy profile below the rough surface is complex for $N_e = 3 \times 10^{27}$ m^{-3}, as shown in Figure 5.11(e) and Figure 5.11(f). For $\delta = 50$ nm, the phenomena observed in Figure 5.11(c) are enhanced. That is, the stripes of energy parallel to the polarization of the laser radiation are more regular, and they are more clearly interrupted by small vertical stripes related to the type-r features. For $\delta = 75$ nm, the small vertical stripes of energy induced by the type-r features in the same domain are almost absent. It is therefore easier to recognize a parallel pattern of absorbed energy. However, this pattern is modulated in the horizontal direction with a periodicity $\Lambda \approx 695$ nm. The absorbed energy profile for $N_e = 3 \times 10^{27}$ m^{-3} is characteristic for the competition of the type-s, type-d and type-r features in the space domain.

In Figure 5.12, 10×10 µm^2 top view representations of the absorbed energy at 50 nm and 75 nm below a random rough surface are shown in the left and right column, respectively, for larger N_e than in Figure 5.11. That is, $N_e = 4 \times 10^{27}$ m^{-3}, $N_e = 5 \times 10^{27}$ m^{-3} and $N_e = 8 \times 10^{27}$ m^{-3}. Compared to Figure 5.11, the orientation of the absorbed energy is now orthogonal to the polarization of the laser radiation. In Figure 5.12(a) two kind of periodicities are visible, even though it is difficult to establish their exact periodicity. They are the results of the type-s and the type-r features in the space domain. For a depth $\delta = 75$ nm, the periodicity related to the type-s features, $\Lambda \approx 635$ nm, can be observed more easily. It is worth noting that this periodicity is smaller than in the $N_e = 3 \times 10^{27}$ m^{-3} case since the type-r features are merging with the type-s features, leading to a decrease of periodicity.

With an increase of N_e, the periodicity resulting from the expression of the type-s features in the space domain becomes progressively more apparent, as shown in Figure 5.12(c) to Figure 5.12(f). Interestingly, the stripes of energy with small periodicities are still visible in apparent disagreement with the disappearance of the type-r features observed in Figure 5.9 on page 67. In fact, the amplitude of the type-s features is so large that the type-r features are completely concealed. However, the type-r features still exist as indicated by the space domain study in this section. A careful analysis shows that the periodicity linked to the type-s features increased, with $\Lambda \approx 725$ nm

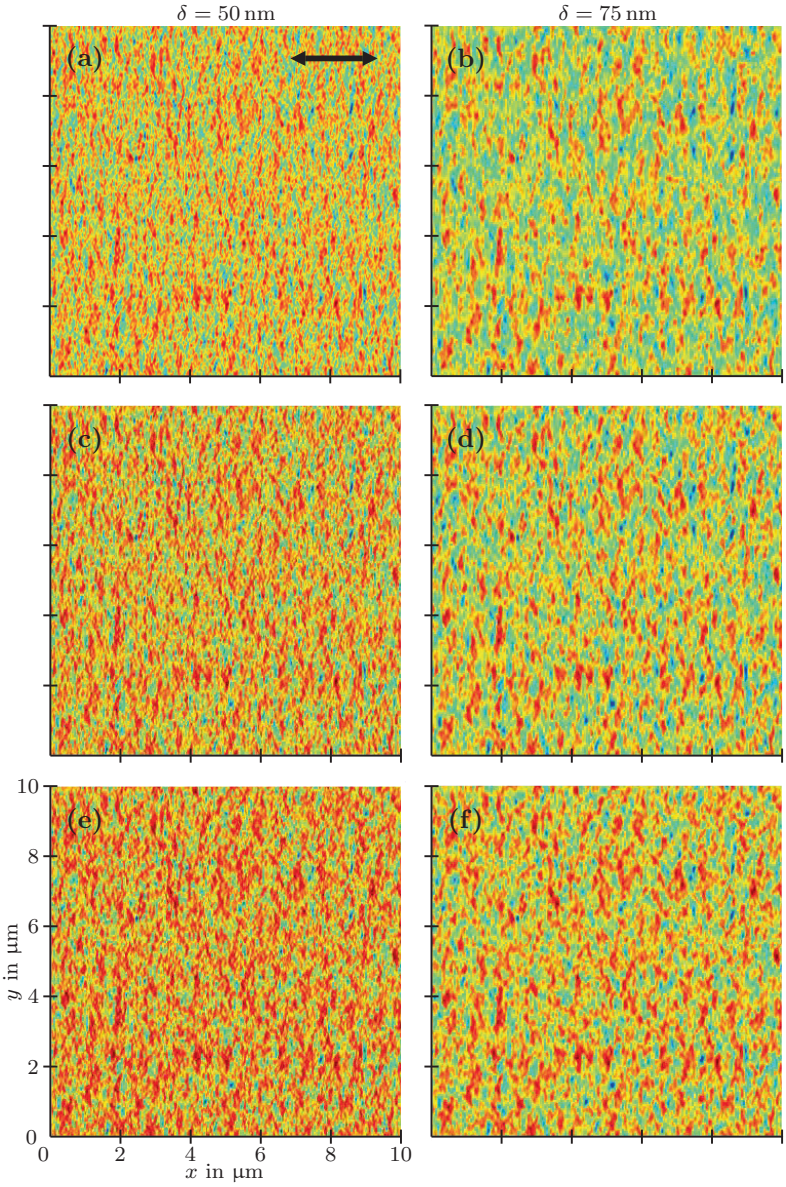

Figure 5.12: 10×10 µm^2 top view representations of the absorbed energy 50 nm (left column) and 75 nm (right column) below a random rough surface, for (a-b) $N_e = 4 \times 10^{27}$ m^{-3}, (c-d) $N_e = 5 \times 10^{27}$ m^{-3} and (e-f) $N_e = 8 \times 10^{27}$ m^{-3}. The polarization direction is indicated by the black arrow. Each picture is shown with a color map ranging from blue to red for the smallest to the largest value, respectively.

for $N_e = 5 \times 10^{27}$ m^{-3} and $\Lambda \approx 730$ nm for $N_e = 8 \times 10^{27}$ m^{-3}, in comparison to $\Lambda \approx 635$ nm for $N_e = 4 \times 10^{27}$ m^{-3}.

The space domain results reveal that the periodicity in absorbed energy below the rough surface can explain the formation of many kinds of LIPSSs, as expected from the FDTD-η maps. Stripes of equal absorbed energy running parallel or orthogonal to the laser polarization, and with a periodicity significantly smaller than the laser wavelength $\Lambda \ll \lambda$, can be the trigger of HSFL formation. Likewise, stripes of equal energy orthogonal to the polarization, with a periodicity slightly smaller than the wavelength $\Lambda < \lambda$, can lead to LSFL formation. However, LIPSSs are the result of the interaction of many pulses with the rough surfaces of materials, as mentioned in chapter 2. This requires that the new rough surface profile, resulting from the interaction of the absorbed energy pattern below the rough surface and the material, is beneficial for the growth of LIPSSs.

5.5 Conclusion

The FDTD calculations and the Sipe theory have been compared in this chapter. The results of the numerical approach, the FDTD-η maps, are in good agreement with the analytical solutions, the η maps, for not too large $|k_x|$. The type-s features and type-d features follow the same trends in the FDTD-η and the η maps. The main difference between the two approaches lies in the type-r features characteristics which are not handled correctly in the Sipe theory case. The FDTD approach allows to study the depth dependence of the frequency maps features and their expression in the space domain. The main outcome of these studies is that HSFLs and LSFLs properties, in terms of periodicity and orientation, can be explained by the interaction of electromagnetic waves with rough surfaces. That is, the absorbed energy profiles below the rough surface of materials show similar properties as LIPSSs. These patterns can show small periodicities in the direction orthogonal or parallel to the polarization of the laser radiation, leading to HSFL formation. Likewise, periodicities closer to the laser wavelength, leading to LSFL formation, can also be observed. A summary of the frequency domain features which were reported in this chapter is shown in Figure 5.13, along with the kind of LIPSSs they can represent. It is worth noting that the type-g features, possibly related to grooves, were not characterized in terms of orientation and periodicity. While these different features show a good agreement with the various properties of LIPSSs, it is not clear how the new rough surface created by the absorbed energy will enhance LIPSS growth. The latter is the focus of chapter 6.

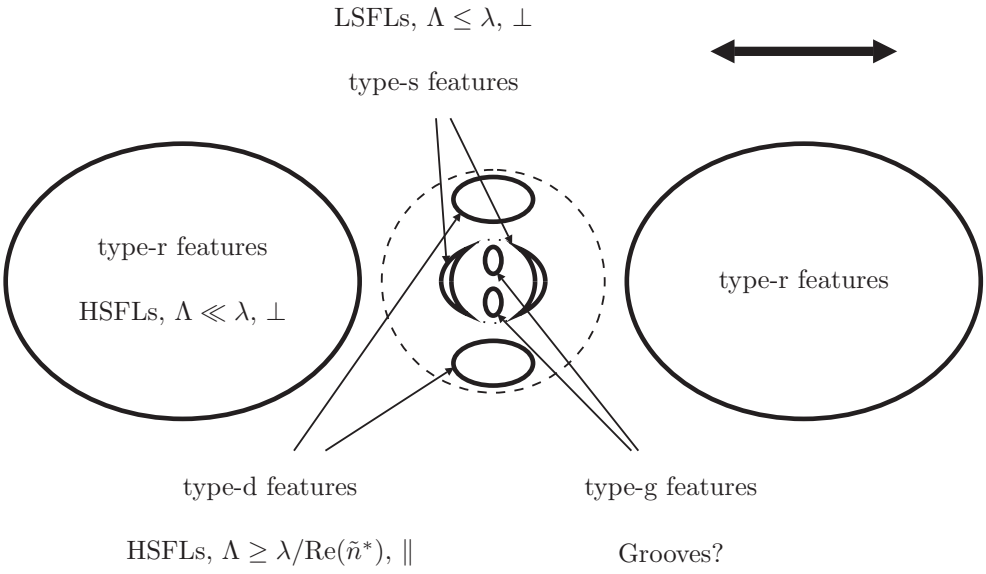

Figure 5.13: Summary of the frequency domain features which were reported in this chapter, along with the kind of LIPSSs they can represent. The dotted and dashed circles denote $\|\vec{k}\| = 1$ and $\|\vec{k}\| = \mathrm{Re}(\tilde{n}^*)$, respectively. The polarization direction is indicated by the black arrow.

Chapter 6

Inter-pulse feedback mechanisms in LIPSS formation

In this chapter the FDTD calculations are combined with an holographic ablation model, in order to study the role of inter-pulse feedback mechanisms in LIPSS formation. The simulations show that LSFLs and HSFLs are able to develop. The characteristics of these simulated LIPSSs are compared to literature.

6.1 Introduction

In chapter 5, it was shown that the properties of the absorbed energy profile below the rough surface of materials can explain most of the characteristics of LIPSSs. It was shown that the type-s features correspond to the periodicities and orientation of LSFLs, while the type-d and type-r features match the periodicities and orientations of HSFLs parallel and orthogonal to the polarization of the laser radiation, respectively. These features, and their equivalents in the space domain, depend on the optical properties of materials and on the depth at which they are studied. Therefore, the prediction of the type of LIPSSs which grow is approximative when FDTD-η maps are used.

To predict more accurately which LIPSSs form, the inclusion of inter-pulse feedback mechanisms in the model is required. That is, the progressive pulse per pulse modification of the roughness, is responsible for the development of a certain type of LIPSSs to the detriment of the others. As discussed in chapter 2, the physics of inter-pulse feedback mechanisms is complex. In the case of nanosecond laser pulses for example, several melting regimes, during which LSFLs form, have been identified by Young et al. [41]. In the case of ultra-short laser pulses, such a study is missing, but ablation seems to play a key role regarding the growth of LIPSSs [10, 51, 72].

A detailed physical modeling of the mechanisms governing the transport of molten or ablated material is out of the scope of this thesis since the focus is on the interaction of electromagnetic waves with rough surfaces. Instead, a simplified approach was chosen to account for inter-pulse feedback mechanisms due to ablation. This simplified model is presented in section 6.2, along with the assumptions used. Then, the simulation results are presented. That is, the formation of LSFLs, see section 6.3, HSFLs orthogonal to the polarization, see section 6.4, and HSFLs parallel to the polarization, see section 6.5, are discussed. An overview of the LIPSSs predicted by the FDTD-feedback simulations is presented in the space domain, as well as in the frequency domain, see section 6.6. Finally, the formation of a complex superimposed LIPSS pattern is shown in section 6.7.

6.2 Holographic ablation model

6.2.1 Characteristics of the model

Figure 6.1 shows schematically the approach chosen to account for inter-pulse feedback mechanisms, which is referred to as "holographic ablation model" (HAM). In the HAM, the linearly polarized plane wave interacts with the rough surface and the absorbed energy distribution $A(x, y, z)$, resulting from this interaction, is calculated based on the FDTD method, as explained in chapter 4 and 5. Once $A(x, y, z)$ is obtained, an isoline of absorbed energy, $A(x, y, z) = A_{\text{ablation}}$, is selected. The rough surface is modified by material removal. That is, all the material above the chosen isoline is "removed" from the simulation domain and the new surface morphology follows the isoline. The surface morphology is used for another FDTD simulation, leading to a new absorbed energy profile and a further modification of the surface. The FDTD-feedback cycle can be iterated as many times as necessary. This approach allows to study qualitatively the inter-pulse feedback mechanisms involved in LIPSS formation. The word "holographic" was used in a recent article [91], to refer to the Sipe theory [13] and the work of Young et al. [5, 41]. While, the Sipe theory does not involve inter-pulse feedback mechanisms, the term "holographically eroded pattern" mentioned in [91] describes well the HAM.

The constant A_{ablation} is an additional parameter, which needs to be chosen carefully. Although the ablation thresholds of materials can be determined experimentally [48]. An exact value would be of little use in the HAM, because the intra-pulse feedback mechanisms are included in the FDTD calculations only qualitatively. That is, the optical properties are kept constant during one run of FDTD simulations, in accordance with the number of electrons in the conduction band and the Sipe-Drude model [58]. Similarly, the dynamics of the carriers, the electron and the lattice temperatures of the material are not calculated. Hence, no quantitative prediction of the absorbed energy is possible, therefore, A_{ablation} should be calculated differently. Prior to FDTD simulations including feedback, a FDTD simulation, with identical parameters, is used to calculate the absorbed energy below a flat surface. At a certain depth, the absorbed energy A_{ablation} necessary to remove a thickness of material, referred to as ablation depth Δ_{ablation}, can be read and

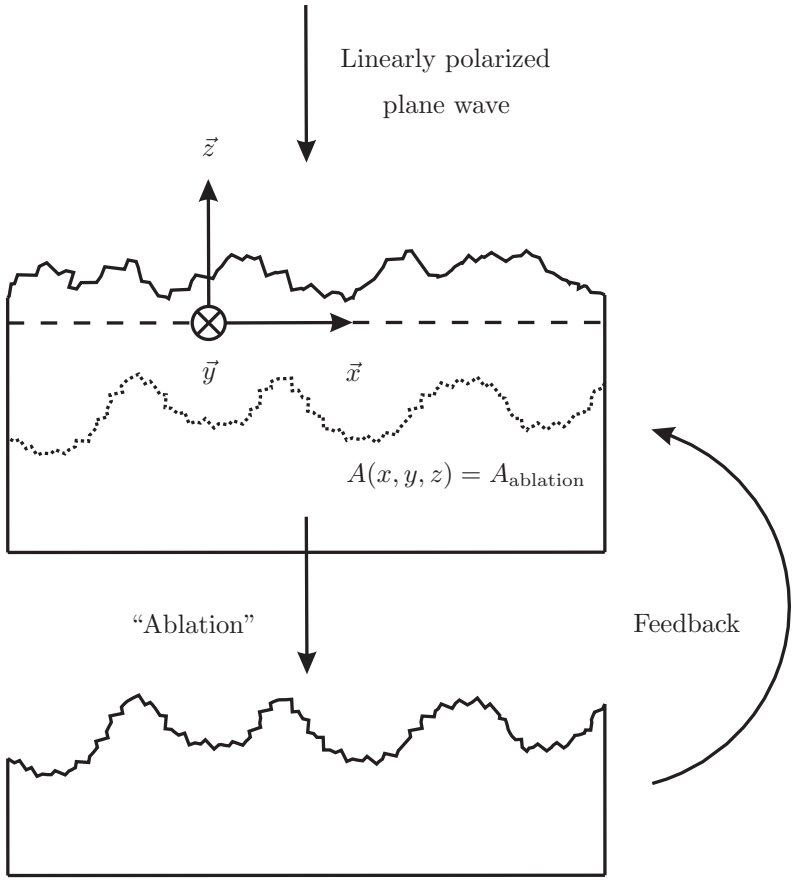

Figure 6.1: Holographic ablation model. The dotted line represents an isoline of absorbed energy, $A(x, y, z) = A_{\text{ablation}}$. The function $A(x, y, z)$ denotes the absorbed energy profile below the rough surface. The parameter A_{ablation} is the absorbed energy level above which the material is "ablated".

stored to perform the feedback step in the HAM. That is, the removal of material required to create a new roughness. Since there is a bijection between A_{ablation} and Δ_{ablation}, for constant simulation parameters, Δ_{ablation} is employed to discuss the simulations presented in this thesis. It is worth noting that in the HAM, Δ_{ablation} is an input parameter, as well as the number of electrons in the conduction band N_e. However, in experiments, a qualitative relation exists between these quantities: a high fluence leads to large values of N_e and a large value of Δ_{ablation}, where the exact magnitude depends on the material. In the HAM, these two quantities are decoupled since the relation between N_e and Δ_{ablation} is too complex to be included quantitatively in the model. This is not always a drawback, since this decoupling

allows to investigate hypothetical materials. Hence, it allows to discuss the results of the FDTD-feedback simulations for other materials than silicon only.

6.2.2 Conditions and parameters of the FDTD-feedback simulations

The HAM can be applied with numerous sets of parameters, such as different laser wavelengths, optical properties or thickness of the ablated layer. However, it would be impractical to test all these combinations of parameters, therefore a limited scope of the FDTD-feedback simulations must be carefully selected. To allow comparison, the simulations results presented in this chapter were calculated with the parameters discussed in chapter 5. That is, the simulation domain is spanned by Yee cells of dimensions $\Delta x = \Delta y = 20\,\text{nm}$ and $\Delta z = 5\,\text{nm}$. A linearly polarized plane wave, along $\vec{x}$, with a wavelength $\lambda = 800\,\text{nm}$ is incident on the rough surface of the semi-infinitely extended medium. Like in chapter 5, the optical properties of the medium were chosen based on the Drude model proposed by Bonse et al. [58]. The FDTD calculations were performed with a simulation domain similar to the domain described by Figure 5.3 on page 56, except that the roughness region was not limited to a 1 yc thickness, because surface morphologies grew in this region. The initial roughness was extracted from the set of 100 different roughness patterns used to generate the FDTD-η maps, as discussed in section 5.2.4. A top view of this $20 \times 20\ \mu\text{m}^2$ roughness profile is shown in Figure 6.2(a) along with its Fourier transform in Figure 6.2(b). Only white noise can be observed, indicating that no frequency of the roughness spectrum is favored. This is in accordance with the slowly varying function $b(\vec{k})$ mentioned in chapter 3.

Compared to chapter 5, the only new parameter in this chapter is the ablation depth Δ_{ablation}. While the FDTD-η maps were studied as function of the depth δ, Δ_{ablation} is a fixed parameter for each FDTD-feedback simulation. As discussed in chapter 2, LIPSSs grow at fluence levels close to the single pulse ablation threshold, where the average ablation rate is less than 100 nm/pulse [48]. Moreover, it was shown in chapter 5 that the FDTD-η maps show less variations at large depths, i.e. $\delta \geq 50\,\text{nm}$. Therefore, the thickness of material removed per FDTD-feedback cycle is limited to 50 nm in this thesis, $\Delta_{\text{ablation}} \leq 50\,\text{nm}$. In addition, the minimum thickness of material removed per FDTD-feedback cycle was chosen to be less than 20 nm, $\Delta_{\text{ablation}} \geq 20\,\text{nm}$, since simulations with $\Delta_{\text{ablation}} < 20\,\text{nm}$ did not bring interpretable results. The latter is explained in more details in section 6.6.

6.3 Formation of LSFLs

In this section, an example of formation of LSFLs is presented in the framework of the FDTD-feedback simulations. Then, a recurrent topic regarding LSFLs, the variation of their periodicity, is discussed in 6.3.2.

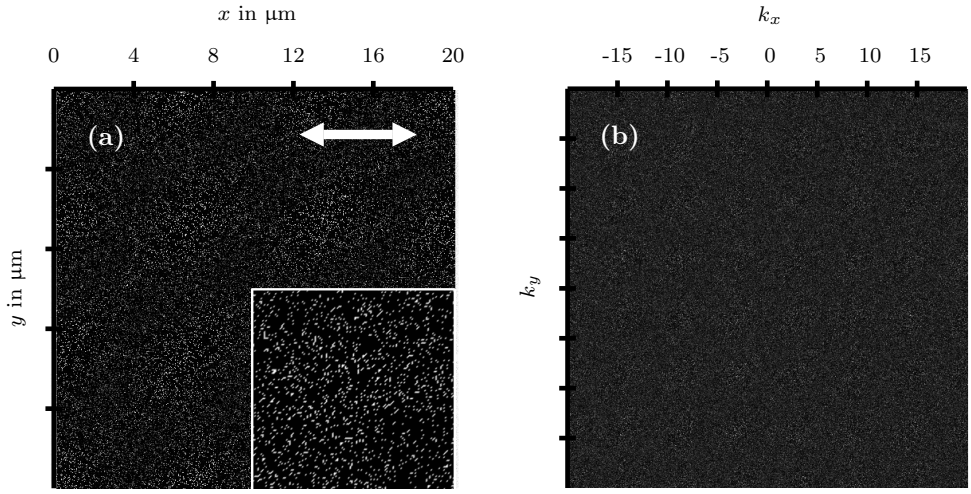

Figure 6.2: (a) 20×20 µm^2 top view of the rough surface at the start of the FDTD-feedback simulations, with a zoom in the bottom right insert. (b) Fourier transform of the rough surface shown in (a). Both figures use a grayscale colormap, where the white color represents the largest values. The polarization direction is indicated by the white arrow.

6.3.1 Example

Figure 6.3 shows the formation of LSFLs, starting from the rough surface presented in Figure 6.2, as a function of the number of FDTD-feedback cycles. The FDTD-feedback simulations were performed with $N_e = 8 \times 10^{27}\mathrm{m}^{-3}$ ($\tilde{n}^* = 1.339 + 3.220j$) and $\Delta_{\mathrm{ablation}} = 50\,\mathrm{nm}$.

The surface morphology changes mainly during the first 3 FDTD-feedback cycles. After the first cycle, in Figure 6.3(a), the initial roughness is completely "erased" and only seeds for the excitation of SPPs remain. The second cycle, in Figure 6.3(b), results already in the presence of periodic structures which will enhance strongly the plasmonic effects, leading to well defined LSFLs after the third cycle shown in Figure 6.3(c).

The remaining cycles induce four phenomena. First, the LSFLs "connect" progressively in the vertical direction, which increases their regularity. Secondly, the contrast increases from Figure 6.3(d) to Figure 6.3(i), implying that the LSFLs deepen. Thirdly, "beams" of SPPs (white lines in Figure 6.3(f)) occur gradually with increasing number of cycles. Finally, a periodicity in the direction orthogonal to LSFLs can be observed, mainly in Figure 6.3(h) and Figure 6.3(i). The first two phenomena show that the HAM introduces inter-pulse feedback mechanisms, which promote the formation of LSFLs. The third phenomenon is characteristic of LSFL formation on silicon. Indeed, Bonse et al. showed that SPPs are involved in LSFL

formation and that "beams" of SPPs can be observed after laser treatment of the sample [38, 58]. Concerning the last phenomenon, the stripes running parallel to the laser polarization show a periodicity Λ ranging from 1.5 µm to 3.3 µm in Figure 6.3(i). Interestingly, the orientation and the range of periodicity of these stripes match the characteristics of the grooves observed by Bonse et al. [39]. The results of the FDTD-feedback simulations presented in Figure 6.3 suggest that the grooves grow where LSFLs are not able to "connect". After 9 FDTD-feedback cycles, LSFLs are still the dominant phenomenon. It seems that the grooves need a more accurate modeling of inter-pulse feedback mechanisms to grow in the framework of this approach.

The HAM is too "simple" to predict the height of LIPSSs correctly. However, the averaged peak-to-valley height h measured in Figure 6.3(i), $h = 124 \pm 14$ nm, is in the range of expected heights of LSFLs, which is a few hundreds of nanometers, as mentioned in chapter 2.

6.3.2 Variation of the periodicity of LSFLs

As discussed previously, once the LSFLs form, the subsequent FDTD-feedback cycles make them connect vertically and deepen. The periodicity of LSFLs is already well defined after 3 cycles and does not evolve significantly afterwards. Their periodicity is $\Lambda = 714 \pm 21$ nm in Figure 6.3(i). In chapter 2, it was reported that Bonse and Krüger gathered three possible explanations for the periodicity of LSFLs being smaller than the laser wavelength ($\Lambda \leq \lambda$) [39]. Firstly the authors argued that, the periodicity of SPPs depends on the optical properties of the material under consideration [37, 58]. Since the optical properties vary with the excited state of the material (i.e. number of electrons in the conduction band of semiconductors and dielectrics), different fluences lead to different optical properties. Hence, different periodicities of SPPs. This assertion will be discussed in more detail in the next paragraph. Secondly, the periodicity of SPPs is affected by the presence of gratings on the surface, LSFLs in this case. According to Huang et al. [37], the grating like LSFLs deepens with the number of pulses applied and this deepening leads to a decrease of the phase velocity of SPPs [71], therefore, a decreased periodicity of the interference pattern. It was argued in chapter 2 that this scenario suggests that the whole surface region containing LSFLs melts and subsequently new LSFLs with a smaller periodicity form after resolidification. It is in apparent disagreement with the cross-section study of Borowiec et al. [72], in which only a little resolidified layer of material is visible, mostly on top of LSFLs. Likewise, the combination of the FDTD calculations with the HAM does not support the grating-assisted variation of the periodicity of LSFLs. Thirdly Bonse and Krüger claim that, LSFL periodicity is affected by the angle of incidence. When numerous pulses have been applied to form an ablation crater on the surface, the local angle of incidence of the laser light on the walls of the crater can play a role. This last assertion is out of the scope of this thesis since the FDTD-feedback simulations were developed for normal incidence.

In Figure 6.4, the periodicity Λ of LSFLs is presented as a function of the number of electrons in the conduction band N_e, after 9 FDTD-feedback cycles. The solid

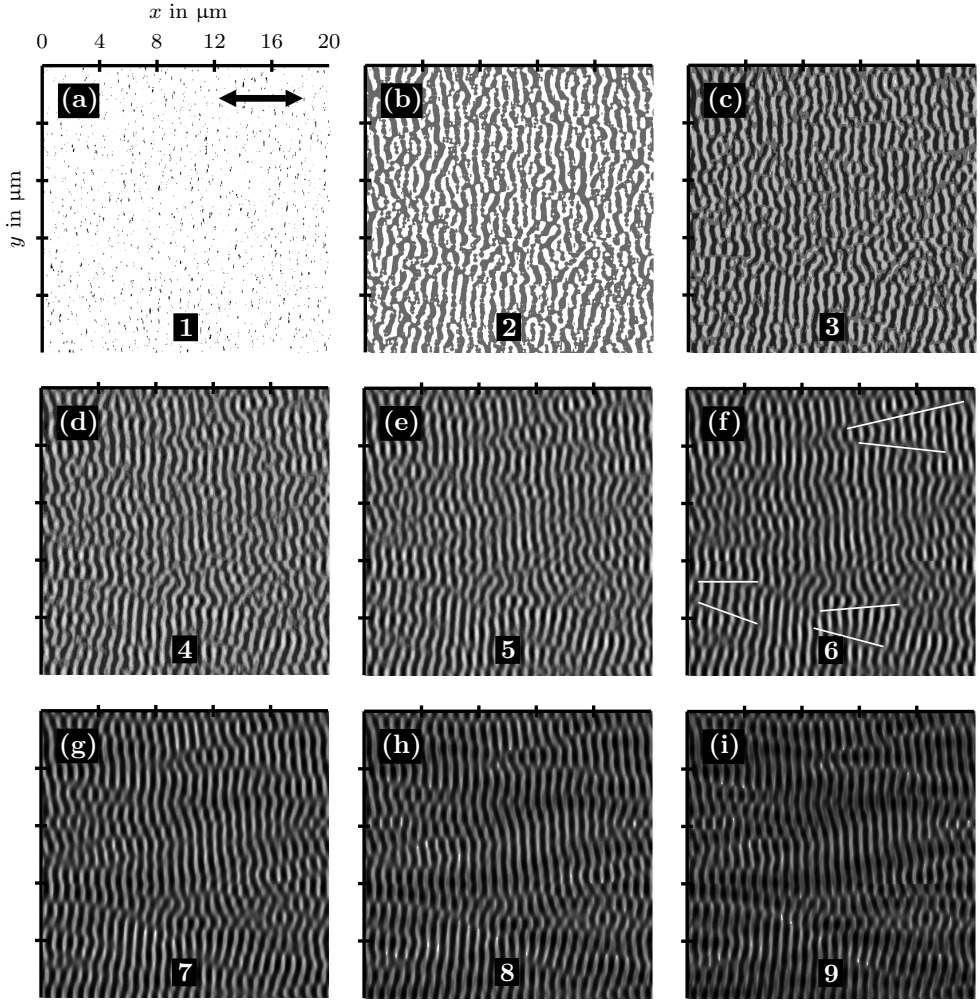

Figure 6.3: Formation of LSFLs, starting from a random rough surface, as a function of the number of FDTD-feedback cycles. The number of cycles is indicated in the bottom of each picture. The simulations were performed at $N_e = 8 \times 10^{27}\mathrm{m}^{-3}$ ($\tilde{n}^* = 1.339 + 3.220j$) and $\Delta_{\mathrm{ablation}} = 50\,\mathrm{nm}$. The white lines in (f) show SPPs "beams". A grayscale colormap, where the white color represents the largest values, is used to represent the evolution of the top view of the surface. The polarization direction is indicated by the black arrow in (a).

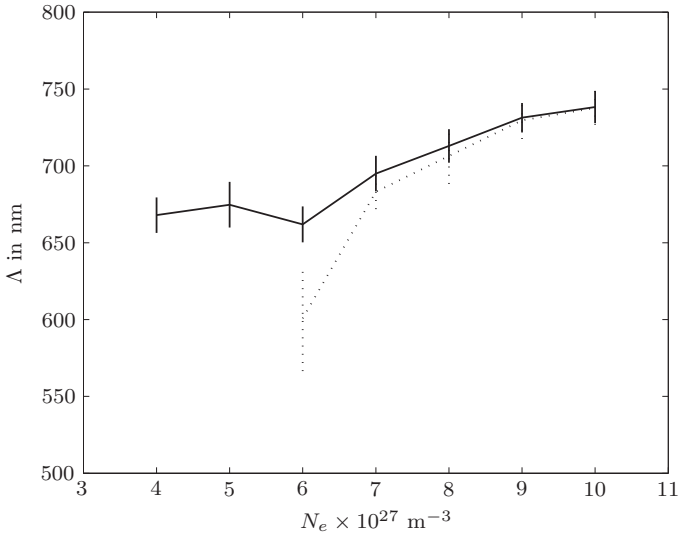

Figure 6.4: Periodicity Λ of LSFLs after 9 FDTD-feedback cycles as a function of the number of electrons in the conduction band N_e. The solid and dotted lines correspond to simulations performed with $\Delta_{\text{ablation}} = 50\,\text{nm}$ and $\Delta_{\text{ablation}} = 30\,\text{nm}$, respectively. The error bars indicate the standard deviation of the periodicities measured in the $20 \times 20\ \mu\text{m}^2$ areas.

and dotted lines correspond to simulations performed with $\Delta_{\text{ablation}} = 50\,\text{nm}$ and $\Delta_{\text{ablation}} = 30\,\text{nm}$, respectively. For $\Delta_{\text{ablation}} = 50\,\text{nm}$, except for the decrease of periodicity observed for $N_e = 6 \times 10^{27}$ m^{-3}, the periodicity of LSFLs increases with increasing N_e, from $\Lambda = 668 \pm 23\,\text{nm}$ for $N_e = 4 \times 10^{27}$ m^{-3} to $\Lambda = 738 \pm 21\,\text{nm}$ for $N_e = 10 \times 10^{27}$ m^{-3}. The smallest value $\Lambda = 662 \pm 23\,\text{nm}$ of the solid curve is found at $N_e = 6 \times 10^{27}$ m^{-3}, while it was expected for $N_e = 4 \times 10^{27}$ m^{-3}. This phenomenon may be attributed to the random roughness of the surface set in the simulation, being more or less favorable for a given excitation state (it may also be simply in the range of the error bars). For a smaller ablation depth $\Delta_{\text{ablation}} = 30\,\text{nm}$, the periodicity of LSFLs is only slightly smaller than in the case of $\Delta_{\text{ablation}} = 50\,\text{nm}$, when $N_e > 6 \times 10^{27}$ m^{-3}. This observation is in agreement with the fact that the characteristics of the type-s features do not depend significantly on the depth δ, as discussed in chapter 5. The case of $N_e = 6 \times 10^{27}$ m^{-3}, for $\Delta_{\text{ablation}} = 30\,\text{nm}$, is striking. The periodicity of LSFLs, $\Lambda = 601 \pm 69\,\text{nm}$, is the smallest of Figure 6.4 and the simulation shows the largest error bar in the graph (standard deviation of the measured periodicities). The cause of these observations is the presence of HSFLs, orthogonal to the polarization of the laser radiation, on top of some LSFLs. The growth of these HSFLs is discussed in more detail in section 6.4 as well as in section 6.6.

It is worth noting that, excluding $N_e = 6 \times 10^{27}$ m^{-3} for $\Delta_{\text{ablation}} = 30\,\text{nm}$, the results of the FDTD-feedback simulations are in good agreement with the results of the Sipe-Drude model for silicon [58]. That is, the periodicities predicted are larger than 650 nm and smaller than the laser wavelength. However, this prediction alone does not allow to explain all the experimental observations found in literature. Indeed, for a number of pulses N smaller or equal than 10, the periodicity reported by Bonse et al. [39] are in the range of $650\,\text{nm} \leq \Lambda \leq 800\,\text{nm}$, while for larger number of pulses, $N \geq 100$, the periodicities decrease to $\Lambda \approx 500 - 600\,\text{nm}$. In the Sipe-Drude model, the periodicities of LSFLs are estimated from the location of the type-s features in the frequency domain. Likewise, Huang et al. use SPPs to explain the characteristics of LSFLs [37]. When the periodicities become too small, these theories fail and the grating-assisted SPPs theory was proposed [37, 39]. As discussed previously, the cross-section study of Borowiec et al. [72], along with the combination of the FDTD calculations with the HAM, do not support the grating-assisted variation of the periodicity of LSFLs. Instead, the results of the FDTD-feedback simulations suggest that these LSFLs are, in fact, a mix of LSFLs and HSFLs.

6.4 Formation of HSFLs orthogonal to the polarization

In this section, an example of formation of HSFLs orthogonal to the polarization is presented first. Then, the variation of the characteristics of these HSFLs is discussed in 6.4.2.

6.4.1 Example

Figure 6.5 shows the formation of HSFLs orthogonal to the polarization of the laser radiation, starting from the rough surface presented in Figure 6.2, after 1 to 9 FDTD-feedback cycles. The FDTD calculations were performed for $N_e = 4 \times 10^{27}\text{m}^{-3}$ ($\tilde{n}^* = 1.943 + 1.116j$) and $\Delta_{\text{ablation}} = 30\,\text{nm}$. For the sake of clarity, only the evolution of a 10×10 μm^2 area, extracted from the 20×20 μm^2 surface, is presented.

Three different stages can be identified: (i) a net of stripes after 1 and 2 FDTD-feedback cycles, see Figure 6.5(a) and Figure 6.5(b), (ii) the growth of small protrusions after 3 to 5 FDTD-feedback cycles, see Figure 6.5(c) to Figure 6.5(e), and (iii) the formation and expansion of HSFLs orthogonal to the polarization of the laser radiation after 6 to 9 FDTD-feedback cycles, see Figure 6.5(f) to Figure 6.5(i).

In the first stage, that is in Figure 6.5(a) and Figure 6.5(b), the net of stripes is the result of the contribution of the type-d features and the type-r features to the surface morphology. These first features are responsible for the modulation of the absorbed energy in the y direction while the latter features affect the x direction. The second FDTD-feedback cycle reinforces the two sets of stripes.

The second stage, in Figure 6.5(c) to Figure 6.5(e), is characterized by a dark background. The reason for the dark background is the presence of protrusions with high amplitudes, indicated by the white circles in the graphs, which are progressively

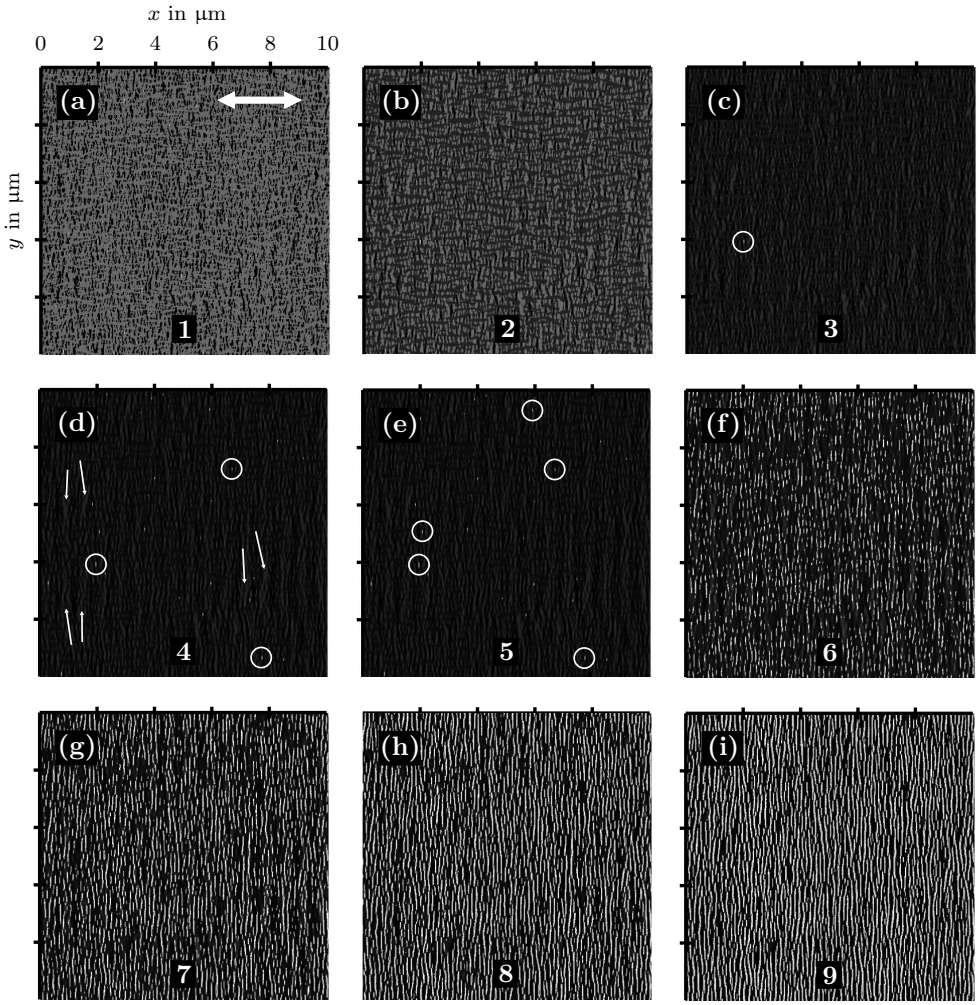

Figure 6.5: Formation of HSFLs orthogonal to the polarization of the laser radiation, starting from a random rough surface, from 1 to 9 FDTD-feedback cycles. The number of cycles is indicated at the bottom of each graph. The simulations were performed at $N_e = 4 \times 10^{27}\mathrm{m}^{-3}$ ($\tilde{n}^* = 1.943 + 1.116j$) and $\Delta_{\mathrm{ablation}} = 30\,\mathrm{nm}$. The white circles in (c), (d) and (e) indicate the location of small protrusions. The white arrows in (d) show the contribution of the type-s features to the surface topography. A grayscale colormap, where the white color represents the largest values, is used to represent the evolution of the top view of the surface. The polarization direction is indicated by the white arrow in (a).

growing, in amplitude and density, and concealing the net of stripes. A careful study of the dark background shows that the net of stripes can still be observed but evolves towards a dominance of the stripes in the y direction from Figure 6.5(c) to Figure 6.5(e). In addition, the type-s features contribute to the background by superimposing a larger periodicity in the x direction, as indicated by the white arrows in Figure 6.5(d).

The third stage involves the formation of HSFLs orthogonal to the polarization of the laser radiation. In Figure 6.5(f), the first HSFLs appear as the result of the growth of the protrusions present in the second stage. However, the "fingerprints" of the type-s features are still visible below these HSFLs. From Figure 6.5(g) to Figure 6.5(i), the HSFLs expand in the y direction and their density increases with each FDTD-feedback cycle until the whole surface is covered. The periodicity of HSFLs in Figure 6.5(i) is $\Lambda = 125 \pm 13\,\text{nm}$, $0.14\lambda \lesssim \Lambda \lesssim 0.17\lambda$, which is in the range of expected periodicities listed in Table 2.3 on page 10.

The averaged peak-to-valley height h of the HSFLs orthogonal to the polarization increases after each cycle in the FDTD-feedback simulations. After 7, 8 and 9 FDTD-feedback cycles the averaged peak-to-valley heights calculated are $h = 152 \pm 4\,\text{nm}$, $h = 182 \pm 1\,\text{nm}$ and $h = 206 \pm 1\,\text{nm}$, respectively. It is worth noting that these heights are comparable to the observations, $h \approx 185\,\text{nm}$, of Hsu et al. on gallium phosphide [10], and that the cross-sectional transmission electron microscopy images show that HSFLs orthogonal to the polarization appear as protrusions with a high aspect ratio, which is in agreement with the FDTD-feedback simulations discussed above. While HSFLs develop on many materials, very few studies about the height of LIPSSs are available in literature.

6.4.2 Variation of the properties of HSFLs

HSFLs orthogonal to the polarization can grow in the simulation domain for various sets of parameters. While this is discussed in more detail in section 6.6, the properties of HSFLs can vary significantly as shown in Figure 6.6. In Figure 6.6(a) to Figure 6.6(c), three different kinds of HSFLs orthogonal to the polarization, and their respective Fourier transform, in Figure 6.6(d) to Figure 6.6(f), are presented. For the sake of clarity, only $5 \times 5\ \mu\text{m}^2$ regions of the $20 \times 20\ \mu\text{m}^2$ surfaces obtained after the simulation are shown. However, the Fourier transform was applied to the total areas of $20 \times 20\ \mu\text{m}^2$.

In the space domain, HSFLs can show variations of width (lateral dimension), length (vertical dimension) and density (number of HSFLs per μm^2). In Figure 6.6(a), HSFLs are wide, long and closely packed, in contrary to Figure 6.6(b), where HSFLs are thin, short and loosely packed. At certain simulation conditions also thin, long and closely packed HSFLs are obtained, see Figure 6.6(c). As a result, these HSFLs cannot be fully characterized by a single well defined periodicity. The same conclusions can be drawn from the frequency domain analysis. The type-r features in Figure 6.6(d) are less spread than in Figure 6.6(e) or Figure 6.6(f), leading to long thick HSFLs in the space domain. The type-r features in Figure 6.6(d) are present at larger values of k_x than in Figure 6.6(e), implying that the overall periodicity of

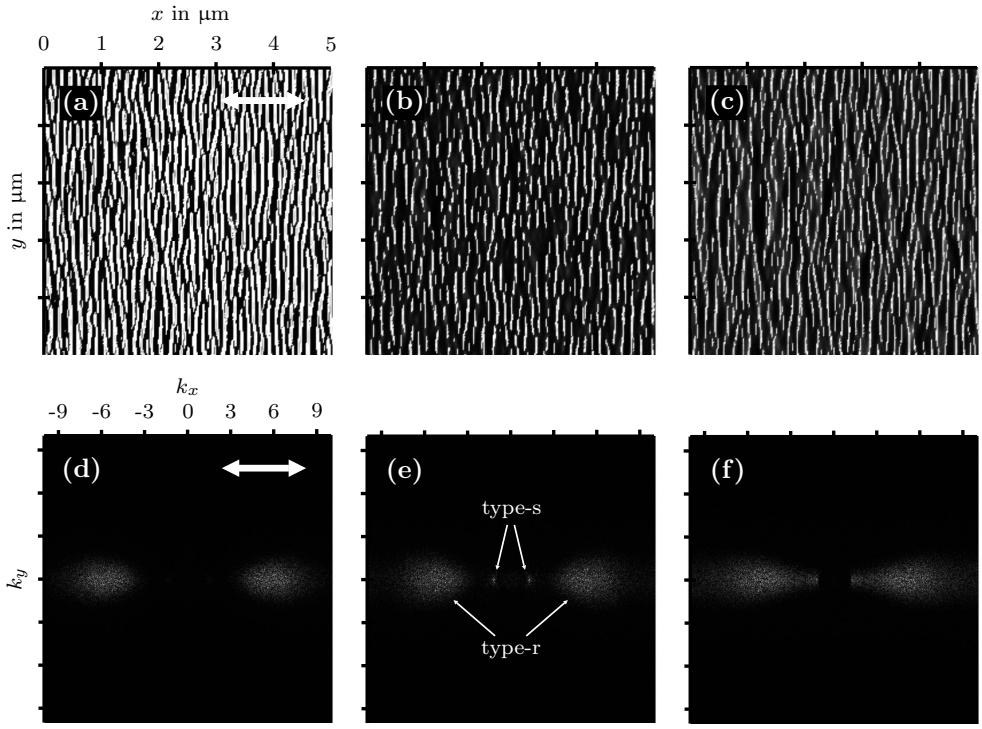

Figure 6.6: 5×5 µm^2 areas covered with HSFLs (upper graphs) and their Fourier transforms (lower graphs), obtained under different simulation conditions. (a) $N_e = 3 \times 10^{27}$ m^{-3}, $\Delta_{\text{ablation}} = 30$ nm and 9 FDTD-feedback cycles. (b) $N_e = 4 \times 10^{27}$ m^{-3}, $\Delta_{\text{ablation}} = 30$ nm and 7 FDTD-feedback cycles. (c) $N_e = 6 \times 10^{27}$ m^{-3}, $\Delta_{\text{ablation}} = 25$ nm and 9 FDTD-feedback cycles. (d), (e) and (f) are the Fourier transforms related to (a), (b) and (c) respectively. The white arrows in (a) and (d) indicate the direction of the polarization of the laser radiation.

HSFLs is smaller in Figure 6.6(a) than in Figure 6.6(b). The type-r features spread in the k_x direction and merge with the type-s features in Figure 6.6(f). Hence, many frequencies contribute to the morphology of HSFLs in Figure 6.6(c), making them finer. While the type-r location is closer to $(k_x,k_y) = (0,0)$ than in Figure 6.6(d) for example, the large spread of the type-r features along the k_x axis implies closely packed HSFLs in the space domain.

It is worth noting that Figure 6.6(d) to Figure 6.6(f) show three kinds of frequency "arrangements" leading to HSFLs in the space domain. Indeed, the type-s features can be almost absent, in Figure 6.6(d), present and distinct from the type-r features, in Figure 6.6(e), or merged with the type-r features, in Figure 6.6(f). This panel of possibilities, and the strong dependence of the location and spread of the type-r

features on (N_e,Δ_{ablation}), is in agreement with what is reported in literature. That is, HSFLs orthogonal to the polarization have been reported with large variations of their properties, mainly in terms of periodicity.

6.5 Formation of HSFLs parallel to the polarization

In this section, an example of formation of HSFLs parallel to the polarization is presented. Then, the growth of these HSFLs on metal surfaces is discussed in 6.5.2.

6.5.1 Example

Figure 6.7 shows the formation of HSFLs parallel to the polarization of the laser radiation, starting from the rough surface presented in Figure 6.2, after 1 to 9 FDTD-feedback cycles. The FDTD calculations were performed at $N_e = 2 \times 10^{27}\text{m}^{-3}$ ($\tilde{n}^* = 2.868 + 0.382j$) and $\Delta_{\text{ablation}} = 30\,\text{nm}$. For the sake of clarity, only the evolution of a 10×10 μm^2 area, extracted from the 20×20 μm^2 surface, is shown.

Three different stages can be identified: (i) a net of stripes after 1 to 3 FDTD-feedback cycles, see Figure 6.7(a) to Figure 6.7(c), (ii) the erasure of the HSFLs orthogonal to the polarization of the laser radiation after 4 and 5 FDTD-feedback cycles, see Figure 6.7(d) and Figure 6.7(e), and (iii) the presence of HSFLs parallel to the polarization of the laser radiation after 6 to 9 FDTD-feedback cycles, see Figure 6.7(f) to Figure 6.7(i).

The first stage, in Figure 6.7(a) to Figure 6.7(c), can be described similarly to the first stage of Figure 6.5 in section 6.4.1: the net of stripes is the result of the contribution of the type-d features and the type-r features to the surface morphology. The first features are responsible for the modulation of the absorbed energy in the y direction while the latter features affect the x direction. However, the protrusions linked to the presence of HSFLs orthogonal to the polarization are already present after the first FDTD-feedback cycle, in Figure 6.7(a). In Figure 6.7(b) and Figure 6.7(c), two sets of ripples develop: HSFLs orthogonal to the polarization on top of HSFLs parallel to the polarization. It is worth noting that after the third FDTD-feedback cycle, in Figure 6.7(c), few of the HSFLs orthogonal to the polarization merge in the x direction, leading to the second stage.

The second stage, in Figure 6.7(d) and Figure 6.7(e), is characterized by the erasure of the HSFLs orthogonal to the polarization. Already after the fourth FDTD-feedback cycle, HSFLs orthogonal to the polarization have almost all merged into HSFLs parallel to the polarization. HSFLs orthogonal to the polarization are completely erased after the fifth FDTD-feedback cycle. In the third stage, HSFLs parallel to the polarization elongates by merging in the x direction. This is particularly clear when comparing Figure 6.7(e) and Figure 6.7(f). After 9 FDTD-feedback cycles, the periodicity of HSFLs is $\Lambda = 345 \pm 21\,\text{nm}$, which is in agreement with the observations in section 5.4.2. Indeed, the periodicity of HSFLs in this simulation is larger than what is expected from the Sipe theory, which

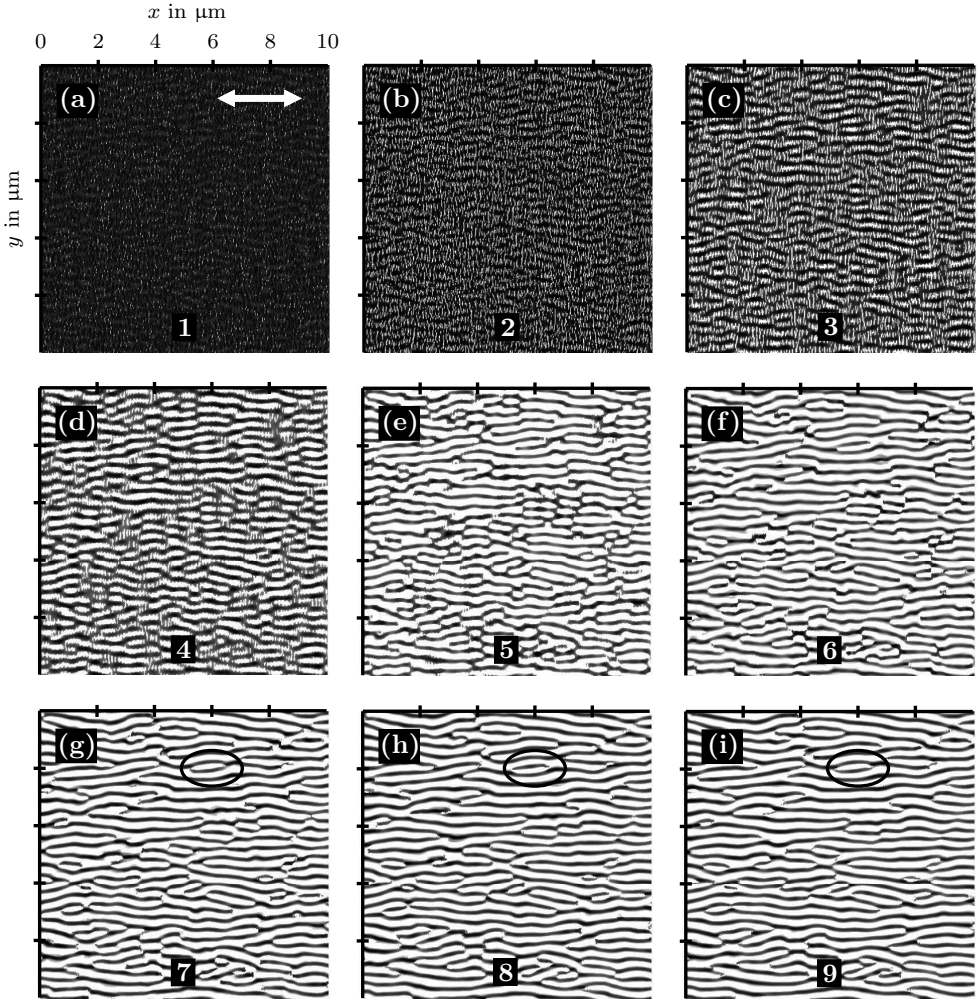

Figure 6.7: Formation of HSFLs parallel to the polarization of the laser radiation, starting from a random rough surface, after 1 to 9 FDTD-feedback cycles. The number of cycles is indicated in the bottom of each graph. The simulations were performed at $N_e = 2 \times 10^{27}\mathrm{m}^{-3}$ ($\tilde{n}^* = 2.868 + 0.382j$) and $\Delta_{\mathrm{ablation}} = 30\,\mathrm{nm}$. A grayscale colormap, where the white color represents the largest values, is used to represent the evolution of the top view of the surface. The polarization direction is indicated by the white arrow in (a). The ellipses in (g), (h) and (i) indicate a phase shift of the HSFLs in the y direction.

predicts a periodicity of about 280 nm. This is attributed to the depth dependence of the type-d features, as discussed based on the FDTD-η maps in section 5.4.1.

The ellipses in Figure 6.7(g) to Figure 6.7(i) are used to guide the eye. By comparing Figure 6.7(g) and Figure 6.7(h), it can be observed that HSFLs undergo a phase shift. Indeed, the peaks of the HSFLs become valleys and the valleys become peaks. The same can be observed by comparing Figure 6.7(h) and Figure 6.7(i). The fact that the phase of the simulated HSFLs alternates with each FDTD-feedback cycle suggest that the HAM is not suited to model their growth. In this transparent regime, i.e. low value of $N_e = 2 \times 10^{27}\mathrm{m}^{-3}$, the "removal" of material between each FDTD-feedback cycle is large which is in contradiction with what is expected from a low excitation regime. Feedback mechanisms involving "molten" material may be more appropriate to simulate this kind of HSFLs. Such a study is outside the scope of this thesis.

6.5.2 Type-d features and metals

HSFLs parallel to the polarization of the laser radiation are related to the presence of the type-d features in the frequency domain. It was shown in chapter 5 that the type-d features are absent in the FDTD-η maps for $N_e \leq 5 \times 10^{27}$ m^{-3}, implying that HSFLs parallel to the polarization should form only on semiconductors and dielectrics. However, these HSFLs were also observed on alloyed steel [14] and titanium [17] for example, as listed in Table 2.3. It was pointed out in section 5.4.2 that the type-d features are, in fact, present but concealed by other frequencies.

In the FDTD-feedback simulations, the effect of the type-d features on the surface morphology can be observed in Figure 6.8. Here, 5×5 μm^2 areas, extracted from the 20×20 μm^2 surfaces used in the simulations, are presented, along with the logarithm of their Fourier transforms. Presenting the Fourier transforms logarithmically allows to observe the presence of frequencies with small amplitudes compared to the maximum.

The three space domain figures, in Figure 6.8(a) to Figure 6.8(c), present nets of stripes, as in Figure 6.5(b). The parallel stripes, related to the type-d features, can be observed when $\mathrm{Re}(\tilde{n}^*) > \mathrm{Im}(\tilde{n}^*)$, shown in Figure 6.8(a), or when $\mathrm{Re}(\tilde{n}^*) < \mathrm{Im}(\tilde{n}^*)$, shown in Figure 6.8(b) and Figure 6.8(c). However, their presence requires a relatively small $\Delta_{\mathrm{ablation}}$ when the excitation state gets high, along with a small number of FDTD-feedback cycles, 3 here.

The characteristics of these stripes parallel to the polarization can vary significantly, in terms of density, length and width. In Figure 6.8(a), the stripes are wide and dense, mainly because they "connect" in the x direction. They are also better defined (sharper) than in the two other cases, in Figure 6.8(b) and 6.8(c). In Figure 6.8(b) and Figure 6.8(c), the stripes are less wide and less extended in the x direction. Their periodicity is also slightly smaller than in Figure 6.8(a), which is more easily concluded from the frequency domain. Naturally, the Fourier transforms are in agreement with the space domain observations. That is, the type-d features show a larger amplitude in Figure 6.8(d) than in Figure 6.8(e) and Figure 6.8(f). Further, the type-d features are present at larger values of k_y and more spread in the case of $N_e = 6 \times 10^{27}$ m^{-3} and the case of $N_e = 8 \times 10^{27}$ m^{-3}.

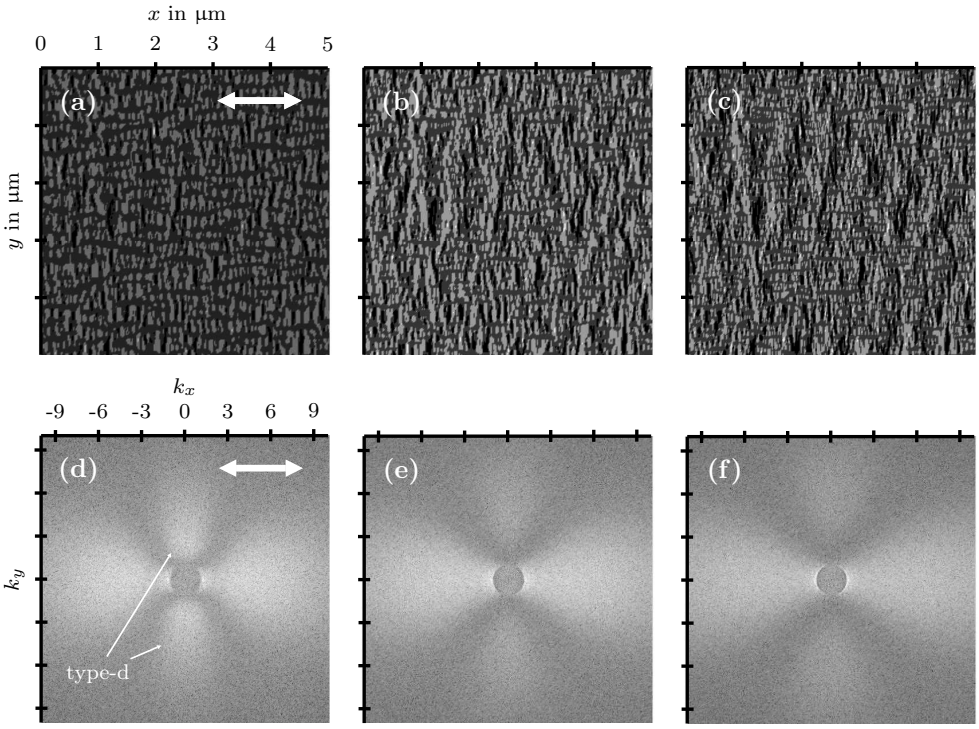

Figure 6.8: 5×5 µm^2 areas, obtained under different simulation conditions (upper graphs), and the logarithm of their Fourier transforms (lower graphs). (a) $N_e = 4 \times 10^{27}$ m^{-3} ($\tilde{n}^* = 1.943 + 1.116j$), $\Delta_{\text{ablation}} = 30$ nm and 3 FDTD-feedback cycles. (b) $N_e = 6 \times 10^{27}$ m^{-3} ($\tilde{n}^* = 1.436 + 2.255j$), $\Delta_{\text{ablation}} = 25$ nm and 3 FDTD-feedback cycles. (c) $N_e = 8 \times 10^{27}$ m^{-3} ($\tilde{n}^* = 1.339 + 3.220j$), $\Delta_{\text{ablation}} = 20$ nm and 3 FDTD-feedback cycles. (d), (e) and (f) are the Fourier transforms related to (a), (b) and (c) respectively. The white arrows in (a) and (d) indicate the direction of the polarization of the laser radiation.

Apart from these stripes parallel to the polarization of the laser radiation, HSFLs parallel to the polarization do not grow in the FDTD-feedback simulations when $\text{Re}(\tilde{n}^*) < \text{Im}(\tilde{n}^*)$. Experimentally, these HSFLs were found to grow on metals irradiated at low fluence levels, in comparison to the fluence levels at which LSFLs grow [14, 17]. As mentioned previously, the HAM seems to fail at describing properly regimes where the molten state of the material plays a role, which is not surprising considering the "ablative" nature of the HAM.

6.6 Overview

In this section, an overview of the LIPSSs predicted by the FDTD-feedback simulations is presented in the space domain first. Then, the characteristic frequency domain signatures of these LIPSSs is discussed in 6.6.2.

6.6.1 Space domain

It was shown in sections 6.3, 6.4 and 6.5 that the initiation and growth of LSFLs, HSFLs orthogonal to the polarization and HSFLs parallel to the polarization, can be modeled by combining FDTD calculations with the HAM. It would be impractical to show the results of FDTD-feedback simulations for each set of (N_e,Δ_{ablation}). Instead, a "map" indicating which kind of LIPSSs is predicted by the model, depending on (N_e,Δ_{ablation}), is presented in Figure 6.9.

This map was compiled by analyzing the LIPSSs obtained after 9 FDTD-feedback simulations for each set of parameters (N_e,Δ_{ablation}), with N_e ranging from 2×10^{27} m^{-3} to 10×10^{27} m^{-3} (with increments of 1×10^{27} m^{-3}) and Δ_{ablation} ranging from 20 nm to 50 nm (with increments of 5 nm). It is worth noting that the solid lines delimiting the different "regions" of the map are not strict boundaries. That is, a more accurate map, based on more simulations with smaller increments, should show transition zones, which could not be represented here to limit the computational efforts. The parameters at which no simulations were carried out are indicated by the hatched areas in the map. As discussed in section 6.2.2, Δ_{ablation} was varied in a limited range only. The upper limit $\Delta_{\text{ablation}} = 50\,\text{nm}$ was chosen because no significant variations of the LIPSS patterns were observed for larger values. The choice for the lower limit $\Delta_{\text{ablation}} = 20\,\text{nm}$ is related to the size of the Yee cells, $\Delta x = \Delta y = 20\,\text{nm}$. When $\Delta_{\text{ablation}} < 20\,\text{nm}$ is chosen, HSFLs with extremely small periodicities seem able to grow. However, an insufficient number of grid points is available to handle such small dimensions correctly. The range of electron densities N_e was selected according to the previous studies of Bonse et al. with the Sipe-Drude model [39, 58].

Six regions can be identified in the map: LSFLs, LSFLs + Grooves, LSFLs + HSFLs $\perp$, HSFLs $\perp$, HSFLs $\parallel$ and "Mix". HSFLs $\perp$ and HSFLs $\parallel$ refer to HSFLs orthogonal and parallel to the polarization of the laser radiation, respectively. Inset pictures which are representative for each region of the map have been included for the sake of clarity, excepted for the "Mix" region which will be discussed in section 6.7. It is important to stress that this map is drawn with the observations made after 9 FDTD-feedback cycles. A map at a lower number of cycles would be more complex, as can be extrapolated from Figure 6.5(b) and Figure 6.7(c) for example.

For high excitations states, i.e. for large values of N_e, and relatively large Δ_{ablation}, LSFLs, see Figure 6.9(d), and LSFLs + Grooves, see Figure 6.9(c), are the dominant LIPSSs. For low excitations states, HSFLs parallel to the polarization, see Figure 6.9(e), were observed, irrespective of the value of Δ_{ablation}. Interestingly, these are the only three kinds of LIPSSs which were reported in literature for silicon irradiated by $\lambda = 800\,\text{nm}$ femtosecond laser pulses [22, 38–40, 58]. This can be explained by

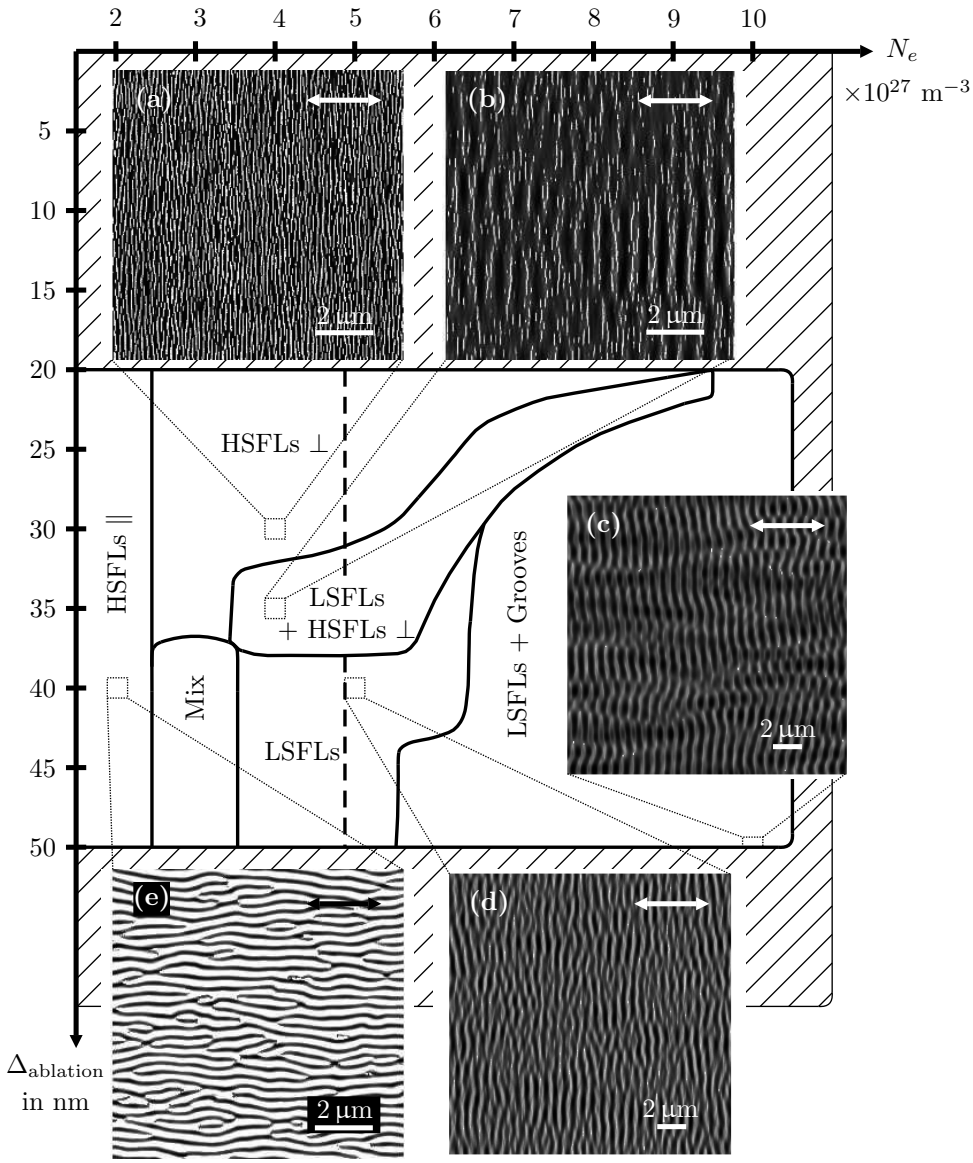

Figure 6.9: Overview of the LIPSSs observed after 9 FDTD-feedback cycles as function of N_e and Δ_{ablation}. The hatched regions indicate the sets of parameters without simulation results. The arrows in the insets indicate the polarization direction of the laser radiation. The dashed vertical line represents $\text{Re}(\tilde{n}^*) = \text{Im}(\tilde{n}^*)$.

recalling that N_e and Δ_{ablation} are decoupled in the HAM. It seems that silicon can hardly be textured in the low Δ_{ablation} regime.

LSFLs are the most common kind of LIPSSs. Their periodicity in Figure 6.9(c) and Figure 6.9(d) is $\Lambda = 738 \pm 21$ nm and $\Lambda = 655 \pm 40$ nm, respectively. This variation of periodicity was discussed in more details in section 6.3.2. It is worth noting that the LSFL region extends to the left of the dashed vertical line, which represents $\text{Re}(\tilde{n}^*) = \text{Im}(\tilde{n}^*)$. The current electromagnetic theories consider LSFLs to be a consequence of the propagation of surface plasmon polaritons, which can only occur when $\text{Re}(\tilde{n}^*) < \text{Im}(\tilde{n}^*)$ [37, 58]. Within the framework of these FDTD-feedback simulations, the propagation of SPPs is not a requirement for LSFL initiation and growth.

The occurrence of HSFLs orthogonal to the polarization, as can be observed in Figure 6.9(a), is the most striking feature of the FDTD-feedback simulations. While LSFLs and HSFLs parallel to the polarization can be predicted by the Sipe theory, HSFLs orthogonal to the polarization received few explanations [18, 21, 24], as discussed in chapter 2. The self-organization model of Reif et al. [24, 76] cannot predict a direct relation between the periodicity of LIPSSs and the wavelength of the laser radiation. While, the electromagnetic based approaches involve SHG [18, 21], which explains HSFL formation only in certain cases. According to Figure 6.9, HSFLs orthogonal to the polarization grow for small values of Δ_{ablation} and a large range of excitation states. However, they are more likely to develop for "moderate" excitation states. Qualitatively, small Δ_{ablation} can be related to hard materials. For example, sapphire [18], titanium nitride or diamond like-carbon [16] are hard materials which exhibits HSFLs very similar to the predictions of the FDTD-feedback simulations. Interestingly, a small value of Δ_{ablation} can be achieved easily with femtosecond lasers while nanosecond lasers tend to affect thicker layers of material. This provides an explanation for the absence of HSFLs after nanosecond laser processing.

HSFLs orthogonal to the polarization can also be found on top of LSFLs after 9-FDTD feedback cycles, as can be observed in Figure 6.9(b). This superposition of LIPSSs, denoted as LSFLS + HSFLs $\perp$, acts like a transition zone between HSFLs orthogonal to the polarization and LSFLs. It is worth noting that the LSFLS + HSFLs $\perp$ pattern can be observed for less FDTD-feedback cycles, prior to the growth of only HSFLs, as shown in Figure 6.5(f). How pronounced the LSFLs and HSFLs are in the space domain depends on the set of parameters (N_e,Δ_{ablation}). Experimentally, such a superposition of LIPSSs was reported by Yao et al. on stainless steel and nickel [92]. Interestingly, in that study, LSFLs grew first, before being covered by HSFLs. The latter is in agreement with the FDTD-feedback simulations presented in Figure 6.5.

HSFLs parallel to the polarization of the laser radiation grow in the FDTD-feedback simulations in the regime corresponding to a low excitation of silicon, as can be observed in Figure 6.9(e). Their periodicity is $\Lambda = 337 \pm 20$ nm. Costache et al. reported the presence of HSFLs on silicon, in the same direction as predicted by the present model [22]. However, they measured a smaller periodicity of $\Lambda \approx 200$ nm. This difference in periodicity is significant, but the LIPSSs observed by

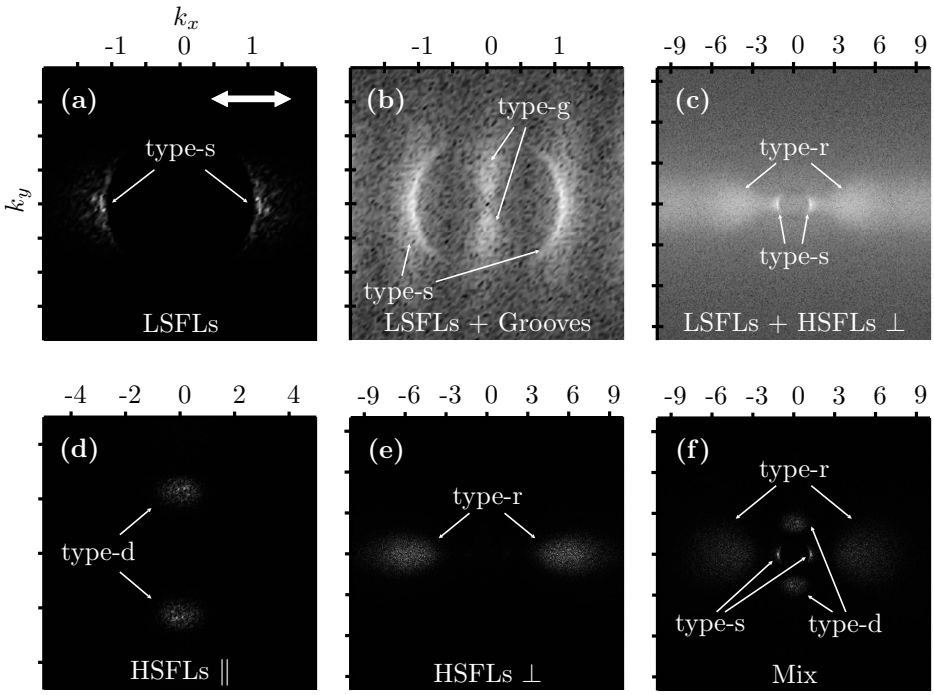

Figure 6.10: Overview of the signature of LIPSSs in the frequency domain. The number of FDTD-feedback cycles is 9, except for (a) and (f), where 6 and 3 cycles were used, respectively. The simulation parameters (N_e,Δ_{ablation}) are indicated without "$\times 10^{27}\text{m}^{-3}$" and "nm", respectively, for each sub-figure. (a) (5,50), (b) (10,30), (c) (4,35), (d) (2,20), (e) (3,30) and (f) (3,35).

Costache et al. were produced with a number of 60000 laser pulses, much larger than the 9 FDTD-feedback cycles. This difference in number of "pulses" can be the cause of a variation in Λ. In addition, it is questionable if the LIPSSs observed by Costache et al. grow under conditions where ablation is the dominant process, since very small fluence levels were involved in their work.

6.6.2 Frequency domain

In Figure 6.10, Fourier transforms which are characteristic of the LIPSS regions presented in Figure 6.9 are shown. One major difference with Figure 6.9 is that not all the results were obtained after 9 FDTD-feedback cycles. The main reason is that certain frequencies are easily concealed by others. In particular, the type-s features tend to dominate the frequency domain after 9 FDTD-feedback cycles, while other LIPSSs than LSFLs can still be observed in the space domain.

Figure 6.10(a) is the most common frequency domain representation of LIPSSs,

which is already known from the Sipe theory [13]. Bonse et al. studied the type-s properties extensively to explain the variation of characteristics of LSFLs [58]. The exact location and spread of the type-s features in the frequency domain depend on the parameters (N_e, Δ_{ablation}) and the number of FDTD-feedback cycles in these simulations, as expected from the space domain discussion and section 6.3.2. In Figure 6.10(b), the logarithm of the Fourier transform of a surface with LSFLs and grooves is shown. The type-g features are better defined than in the FDTD-η maps of section 5.3.3, see Figure 5.5(e) on page 59. It seems that feedback mechanisms are essential for the formation of grooves. It is worth noting that without taking the logarithm of the Fourier transform, only the type-s features would be observed. The same holds for Figure 6.10(c), which is a Fourier transform, characteristic for the presence of HSFLs orthogonal to the polarization on top of LSFLs. As mentioned in chapter 5, the type-r features depends strongly on the depth and the excitation state of the material, implying that HSFLs on top of LSFLs can show large variation of their properties. The type-d features can be observed alone in Figure 6.10(d). These features are located for values of k_y slightly smaller than $\text{Re}(\tilde{n}^*)$ here. However, it was shown in section 6.5.2 that their characteristics can differ from this usual description. The type-r features, in Figure 6.10(e), are the signature of HSFLs in the frequency domain. They can conceal the other frequency domain features, even the type-s features. Interestingly, it is possible to observe three types of frequency features (out of four) jointly in Figure 6.10(f). Inter-pulse feedback mechanisms do not always lead to a clear dominance of a specific kind of frequency domain features. The fingerprints in the space domain of such a frequency arrangement are discussed in the following section.

6.7 Superposition of three kinds of LIPSSs

In this section, the formation of a complex superimposed LIPSS pattern is discussed. This corresponds to the "Mix" region of Figure 6.9 on page 92.

Figure 6.11 shows the formation of a mixed pattern of LIPSSs, starting from the rough surface presented in Figure 6.2, after 1 to 9 FDTD-feedback cycles. The FDTD calculations were performed for $N_e = 3 \times 10^{27}\text{m}^{-3}$ ($\tilde{n}^* = 2.401 + 0.679j$) and $\Delta_{\text{ablation}} = 50\,\text{nm}$.

Unlike the FDTD-feedback simulation results presented earlier in this chapter, stages leading to the formation of the final pattern cannot be identified clearly. Indeed, the evolution of the pattern is progressive. LSFLs start to grow after the third FDTD-feedback cycle, then expand progressively in the y direction to cover finally almost the entire surface after the ninth cycle. While LSFLs evolve, dots, resulting from the expression of the type-d and type-r features in the space domain, are progressively "washed away". The dots can be observed mainly from Figure 6.11(b) to Figure 6.11(d). They are aligned in the x direction with a periodicity defined by the type-r features, while the pitch in the y direction between the "stripes of dots" is defined by the type-d features. The more the LSFLs connect in the y direction, the more the dots are fading away. The white circle in Figure 6.11(f) indicates a region of the surface

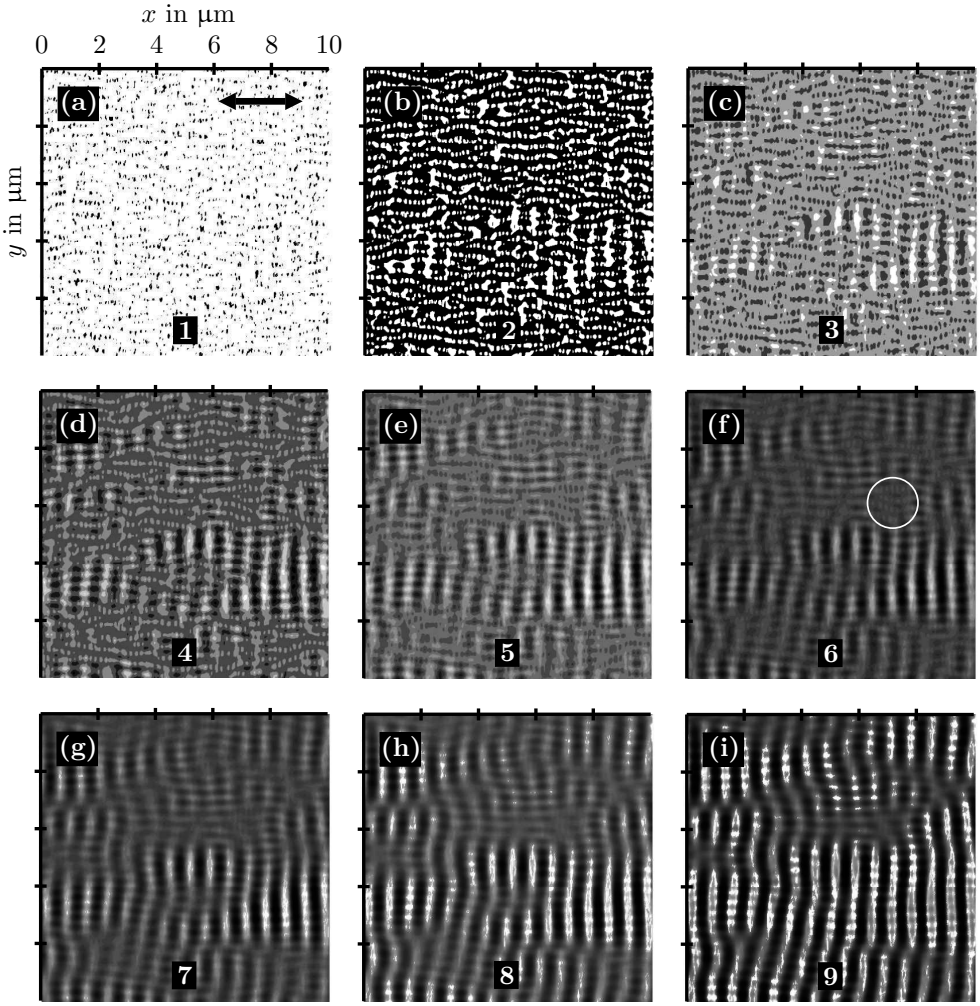

Figure 6.11: Formation of a mixed pattern of LIPSSs, starting from a random rough surface, after 1 to 9 FDTD-feedback cycles. The number of cycles is indicated in the bottom of each picture. The simulations were performed at $N_e = 3 \times 10^{27}\mathrm{m}^{-3}$ ($\tilde{n}^* = 2.401 + 0.679j$) and $\Delta_{\mathrm{ablation}} = 50\,\mathrm{nm}$. A grayscale colormap, where the white color represents the largest values, is used to represent the evolution of the top view of the rough surface. The polarization direction is indicated by the black arrow in (a). The circles in (f) and (g) indicate a region where the dots persist.

where the dots persisted. While the type-d features are combined with the type-r features to form small dots, larger dots are obtained by combining the type-d features to the type-s features. That is, dots can be observed on top of LSFLs, starting from the fourth FDTD-feedback cycle, see Figure 6.11(d). Their periodicity is related to the type-d features in the y direction, while their periodicity in the x direction follows the periodicity of LSFLs.

The superposition of LIPSSs, as shown in Figure 6.11, has not been reported in literature for $\lambda = 800\,\mathrm{nm}$. However, Crawford et al. observed a kind of LIPSSs with a periodicity $\Lambda \ll \lambda$, referred to as "fine bumps", on silicon [29]. These bumps were produced at relatively large wavelengths (about 1300 nm and about 2100 nm) compared to the wavelength of experiments at $\lambda = 800\,\mathrm{nm}$, typical for fs lasers. The array of dots present in the FDTD-feedback simulations offer the possibility to explain the formation of these fine bumps in experiments. The fact that this regime exists in the FDTD-feedback simulations, performed with $\lambda = 800\,\mathrm{nm}$, is probably due to the decoupling of N_e and $\Delta_{\mathrm{ablation}}$.

It is worth noting that the results at $N_e = 3 \times 10^{27}\mathrm{m}^{-3}$ of the FDTD-feedback simulations are particularly important, since it shows that an electromagnetic approach can account for the formation of mixed LIPSS patterns. While, the formation of these patterns was considered to be supporting the self-organization theory [24].

6.8 Conclusion

The combination of FDTD calculations with the holographic ablation model show that it is possible to understand the initiation and growth of LIPSSs in the frame of an electromagnetic approach. In Figure 6.12, a summary of the frequency domain signatures of the LIPSSs predicted by the FDTD-feedback simulations is presented. The model developed in this thesis can account for the formation of LSFLs, HSFLs parallel to the polarization, HSFLs orthogonal to the polarization, grooves and superimposed LIPSS patterns. In details, the model inherited the advantages of the Sipe-Drude theory, leading to good predictions of the characteristics of LSFLs. While the HSFLs and grooves parallel to the polarization of the laser radiation can be simulated, they are the kinds of LIPSSs which show the limitations of the holographic ablation model. It is worth noting that grooves orthogonal to the polarization are the only LIPSSs missing when comparing the results of this chapter and Table 2.4 on page 14. The growth of HSFLs orthogonal to the polarization of the laser radiation is the most important outcome of the FDTD-feedback approach, since it is the first time these LIPSSs are predicted by a model. Due to the lack of frequency analysis on this kind of LIPSSs in literature, it is not possible to conclude that the type-r features are really the cause of the formation of these HSFLs. Therefore, such an analysis is discussed in chapter 7.

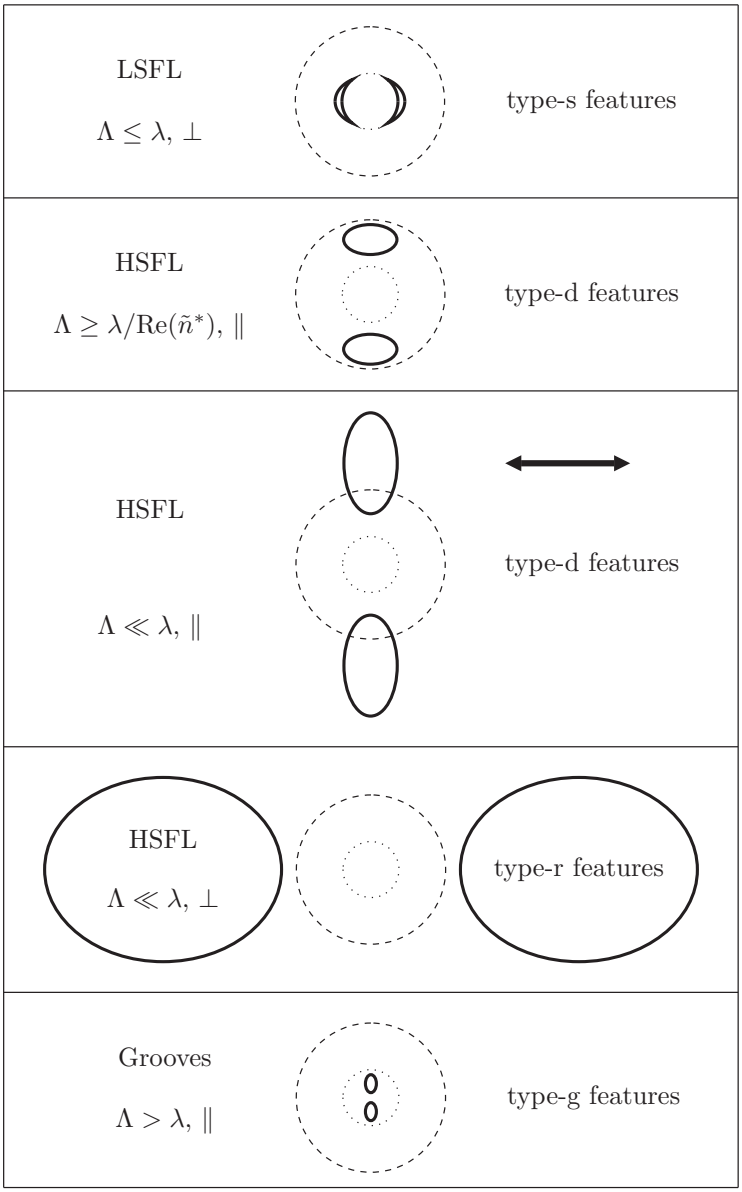

Figure 6.12: Summary of the frequency domain signatures of the LIPSSs predicted by the FDTD-feedback simulations. The dotted and dashed circles denote $\|\vec{k}\| = 1$ and $\|\vec{k}\| = \mathrm{Re}(\tilde{n}^*)$, respectively. The black arrow indicates the direction of the polarization of the laser radiation.

Chapter 7

Experimental validation

In this chapter, experimental results obtained by irradiating sapphire with femtosecond laser pulses are presented. It is shown that HSFLs orthogonal to the polarization, predicted by the FDTD-feedback simulations, are growing on sapphire. The characteristic frequency domain signature of these HSFLs, the type-r features, are used to validate the model.

7.1 Introduction

The core of this thesis was dedicated to the modeling of LIPSS formation. The main reason of this focus was that, while there is a plethora of LIPSSs reported in literature as shown in chapter 2, a model predicting the formation of the different kinds of LIPSSs was lacking.

In chapter 6, the FDTD-feedback simulation results were presented. These simulations predict the formation of a large variety of LIPSSs. Certain kinds of LIPSS, and their signatures in the frequency domain, were already reported in literature. That is, the LSFLs and the HSFLs parallel to the polarization of the laser radiation. Indeed, the formation of LSFLs, along with their variation of characteristics, was studied extensively within the framework of the Sipe theory [13] and the Sipe-Drude model [58], by analyzing the type-s features. Likewise, Wu et al. used the type-d features, predicted by the Sipe theory, to explain the formation of HSFLs parallel to the polarization [27]. The FDTD-feedback simulations inherited these features from the Sipe theory.

In addition to the features inherited from the Sipe theory, it was shown that the FDTD-feedback simulations provide an explanation for the occurrence of grooves and the presence of HSFLs parallel to the polarization on metals. The grooves and their frequency domain representation were reported experimentally [39, 40]. However, it is difficult to compare these observations to the FDTD-feedback results since the

Table 7.1: Summary of the frequency domain studies of LIPSSs. The first column indicates the kind of LIPSSs, the second column indicates the type of frequency domain features, the third column indicates the result of the FDTD-feedback simulations and the forth column indicates if a frequency domain study of these LIPSSs exists or if the Sipe theory was applied to explain the existence of these LIPSSs.

LIPSS	Frequency	FDTD-feedback simulations	Reference(s)
LSFL $\perp$ $\Lambda \leq \lambda$	type-s	Inherited from the Sipe theory	[5, 58]
HSFL $\parallel$ $\Lambda \geq \lambda/\mathrm{Re}(\tilde{n}^*)$	type-d	Inherited from the Sipe theory	[21, 27]
HSFL $\parallel$ $\Lambda \ll \lambda$	type-d	Predicted but not well developed	-
HSFL $\perp$ $\Lambda \ll \lambda$	type-r	Predicted but need validation	-
Grooves $\parallel$ $\Lambda > \lambda$	type-g	Predicted but not well developed	[12, 39, 40]

HAM does not allow to represent well developed grooves. The same holds for HSFLs parallel to the polarization on metals. These HSFLs grow under processing conditions where the melting mechanisms, for which the HAM is not suited, are likely to play an important role.

As mentioned in chapter 6, the prediction of HSFLs orthogonal to the polarization is the most striking result of the FDTD-feedback simulations. Unlike the above mentioned type-s and type-d features, the occurrence of HSFLs orthogonal to the polarization, along with the presence of type-r features, has not been predicted by any other model. Moreover, the ablative nature of the HAM seems to suit the growth of this kind of HSFLs. For these reasons, this chapter is dedicated to experiments to create these HSFLs, as predicted by the model. To prove that these HSFLs orthogonal to the polarization are related to the inhomogeneous absorption of the laser radiation, it must be verified that their frequency domain signature resembles the type-r features.

Table 7.1 summarizes this introduction. That is, the type-s features and the type-d features in the case of transparent materials are inherited from the Sipe theory, therefore they do not require a special attention in this experimental part. The type-d features for metals and the type-g features are predicted by the

FDTD-feedback simulations, but the LIPSSs related to these frequency domain features are not enough developed in the simulations to allow comparisons with experiments. Finally, the frequency domain signature of HSFLs orthogonal to the polarization, the type-r features predicted by the FDTD-feedback simulations, was not reported in literature, which is the focus of this chapter.

In the first part of this chapter, the experimental setup used to perform the experiments is described. In the second part, the results of the experiments are presented and compared to the predictions of the model.

7.2 Experimental setup

The experimental setup is shown schematically in Figure 7.1. The titanium sapphire based laser system, with a central wavelength of $\lambda = 800$ nm, is constituted of a seed/oscillator combination (Coherent, Vitesse Duo) together with a regenerative amplifier (Coherent, RegA 9000). It is used here to deliver femtosecond laser pulses at a repetition rate of 50 kHz. The pulse duration, with a temporal pulse shape assumed to be Gaussian, was adjusted to 180 ± 10 fs using an autocorrelator (APE *pulse*Check). The beam was guided by dielectric coated mirrors to a combination of a beam splitting cube and a $\lambda/2$ plate, which served as a power attenuator. A Galvo-scanner (Scanlab, Scangine 14) was employed to control the location of the laser spot on the sample. Finally, the beam was focused on the sample by a $f = 55$ mm F-Theta lens.

The Gaussian power density profile is characterized by its $1/e^2$ radius of $\omega_0 \approx 6.3\,\mu$m in the focal plane, which was determined by applying the D^2 method [48, 93]. The peak fluence ϕ_0 of the Gaussian distribution was calculated according to

$$\phi_0 = \frac{2E_p}{\pi\omega_0^2}, \tag{7.1}$$

where E_p is the (averaged) pulse energy. The pulse energy was calculated by measuring the average power P delivered by the laser system at the location of the sample, using a power meter (Coherent FieldMaxII-TO, Coherent PM10), and dividing it by the repetition rate. The material chosen to validate the model was sapphire, since it was identified as being a good candidate in section 6.6. The sapphire wafers were cleaned before and after the laser experiments in an ultrasonic bath of acetone.

7.3 Experimental results

7.3.1 Static experiment

Figure 7.2(a) shows a SEM image of the surface of the sample after it was exposed to $N = 16$ laser pulses at the same location. The peak fluence of the Gaussian distribution was $\phi_0 \approx 4.1\,\mathrm{J/cm^2}$. The SEM image reveals HSFLs orthogonal to the polarization of the laser radiation, with a periodicity of $\Lambda \approx 240 \pm 50$ nm. As can be

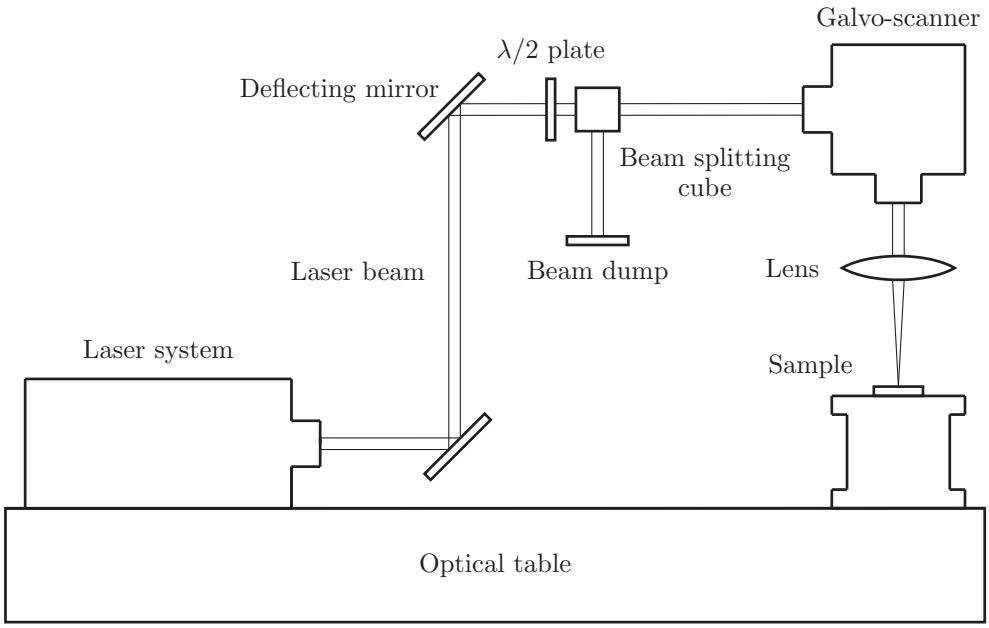

Figure 7.1: Schematic drawing of the experimental setup.

observed, the periodicity varies significantly from the center to the edge of the laser modified area. This is a first indication that the type-r features are involved, because their properties can vary considerably, as explained in chapter 5 and chapter 6.

In Figure 7.2(b), the Fourier transform of the SEM image in Figure 7.2(a) is shown. The type-r features can be clearly recognized from their location and their characteristic spreading in the frequency domain. The type-s features can also be identified around the $\|\vec{k}\| = 1$ circle, even though their amplitude is small compared to the amplitude of the type-r features. The small amplitude of these type-s features may be attributed to the fact that the diameter of the laser modified area is only few wavelengths wide. A larger area, covered with these LIPSSs, is of interest since it would show better defined frequency domain features. Such an area is discussed in the following section.

7.3.2 Dynamic experiment

Figure 7.3 shows an area of the sapphire sample, homogeneously covered with HSFLs orthogonal to the polarization of the laser radiation. This area was produced by using the scanner to place the laser pulses ($\phi_0 \approx 4.1\,\mathrm{J/cm^2}$ and $\omega_0 \approx 6.3\,\mu\mathrm{m}$) at different locations, creating horizontal laser tracks with a vertical pitch of 2 µm between each other. The horizontal pitch between each laser pulse is controlled by the scanning speed of the focal spot. Here, the speed was set to 55 mm/s, which gives a horizontal

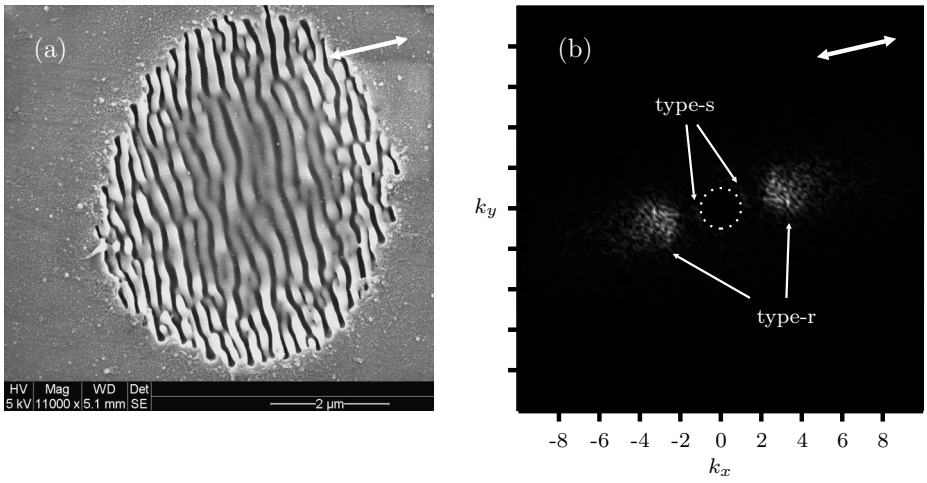

Figure 7.2: (a) SEM image of the surface of the sapphire sample after exposure to $N = 16$ pulses, at peak fluence $\phi_0 \approx 4.1\,\mathrm{J/cm^2}$ and a $1/e^2$ focal spot radius of $\omega_0 \approx 6.3\,\mu\mathrm{m}$. (b) Fourier transform of the SEM image. The frequency domain is normalized by the norm of the wave vector, $2\pi/\lambda$. A high pass filter was applied to suppress the frequencies at $\|\vec{k}\| < 1$, since these low frequencies are mainly related to the ablation crater. The dotted circle indicates $\|\vec{k}\| = 1$. The white arrows indicate the polarization of the laser radiation.

pitch of 1.1 µm at a repetition rate of 50 kHz. It is worth noting that the laser spots (white circles), represented by their $1/e^2$ beam radius, are larger than the apparent spot size on the sample, as can be observed in Figure 7.2. Hence, mainly the top of the Gaussian distribution is contributing to the formation of the HSFLs.

A Fourier transform of the area contained in the dashed white rectangle of Figure 7.3, is shown in Figure 7.4(a). As can be observed in this figure, the type-r features are slightly closer to the center of the frequency domain map, in comparison to Figure 7.2(b), which implies that the periodicity of HSFLs is slightly larger than in the static case, that is $\Lambda \approx 320 \pm 60$ nm. The type-s features in Figure 7.4(a) are better developed than in Figure 7.2(b). However, it is difficult to conclude if this is due to a larger space domain covered with LIPSSs, or different irradiation conditions (from a static experiment to a dynamic experiment). Nonetheless, the outcome of the static experiment and the dynamic experiment is similar. That is, the type-r features can be observed experimentally, which means that HSFLs orthogonal to the polarization are correctly modeled by the FDTD-feedback simulations.

In Figure 7.4(b), the simulation result presented in Figure 6.6(e), on page 86, is recalled. The same arrangement of frequencies can be observed in Figure 7.4(a) and Figure 7.4(b). That is, the type-s features and the type-r features are both present

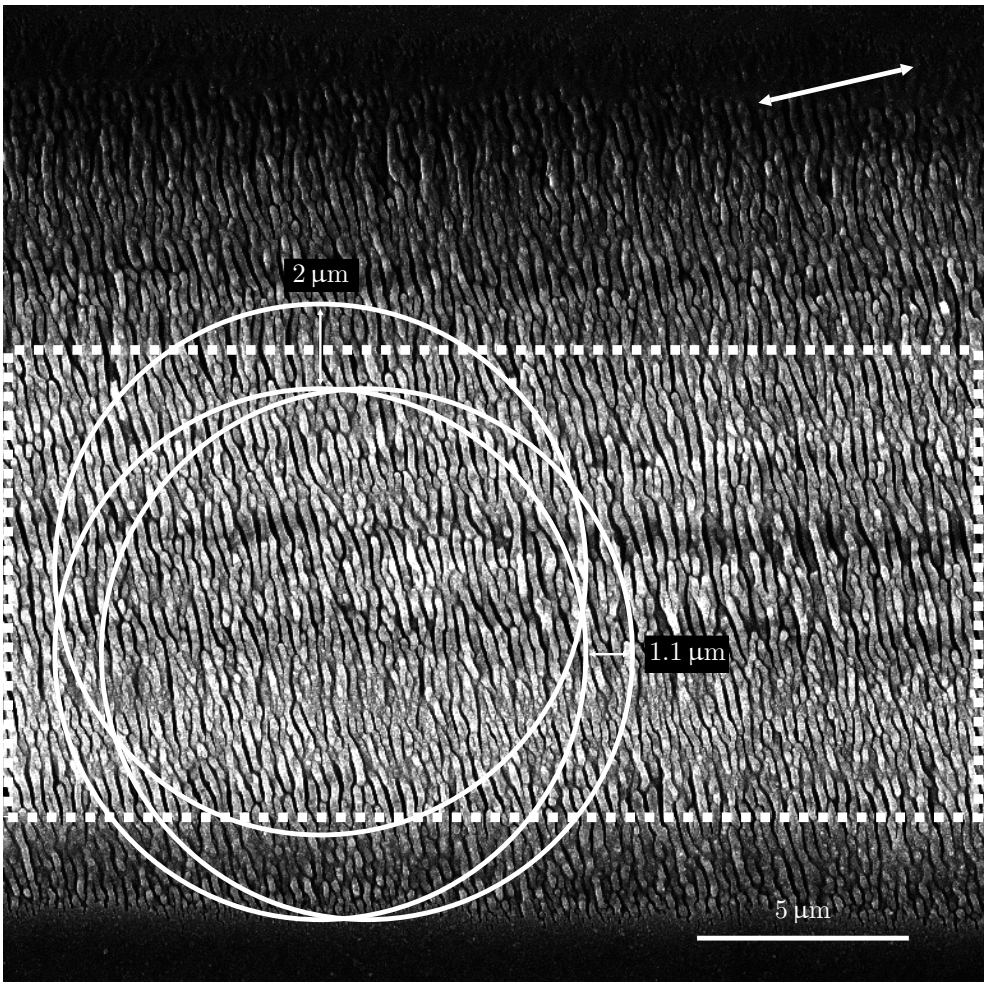

Figure 7.3: Area of the sapphire sample, covered with HSFLs orthogonal to the polarization of the laser radiation. The pulses applied were characterized by a peak fluence of $\phi_0 \approx 4.1\,\mathrm{J/cm^2}$ and a focal post radius of $\omega_0 \approx 6.3\,\mu\mathrm{m}$. The white arrow indicates the direction of the polarization. The white circles are used to indicate the size of the laser spots, in terms of $1/e^2$ beam radius, and the vertical (2 µm) and horizontal (1.1 µm) pitches between them. A Fourier transform of the area in the dashed white rectangle is presented in Figure 7.4(a).

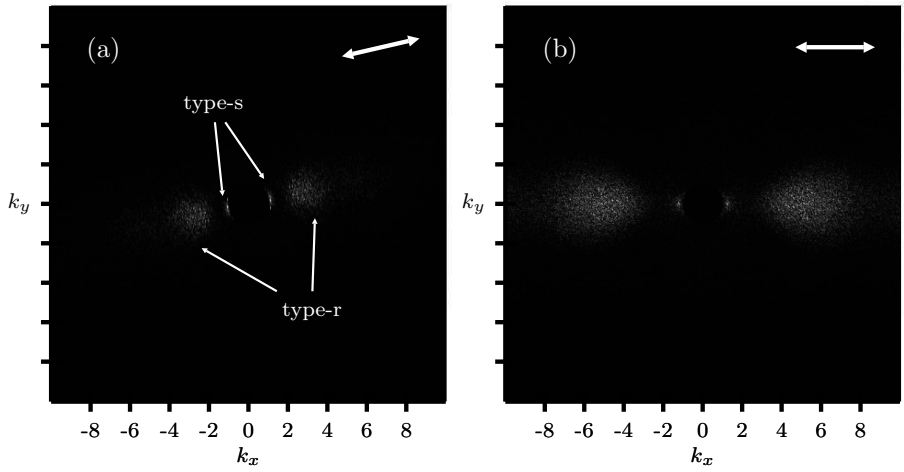

Figure 7.4: (a) Fourier transform of the area in the dashed white rectangle from Figure 7.3. (b) FDTD-feedback simulation result in silicon from Figure 6.6(e).

experimentally and in the FDTD-feedback simulations. However, since the optical properties of sapphire and silicon are different, the exact location and spreading of the type-r features in the frequency domain differ significantly. This was expected from chapter 5 and chapter 6, in which the properties of the type-r features were described as sensitive to the depth at which they are studied, and the optical properties of the material considered.

One should realize that the FDTD feedback simulations were done with the optical properties of silicon, derived from the Sipe Drude model [58]. The fact that the results of FDTD feedback simulations resemble the HSFLs found on sapphire shows the potential of the method developed in this thesis.

7.4 Conclusion

HSFLs orthogonal to the polarization, related to the type-r features in the frequency domain, were observed experimentally. This observation validates the prediction of the FDTD-feedback simulations. That is, HSFLs orthogonal to the polarization can grow on materials and their formation can be explained in the framework of an electromagnetic approach. Moreover, non-linear phenomena, such as SHG, are not a sine qua non condition for HSFL formation. However, it is worth noting that the FDTD-feedback simulations results do not invalidate previous studies where SHG was said to be involved [18, 21]. Each case should be treated separately by performing a frequency domain study.

Chapter 8

Conclusions and recommendations

In this chapter, the conclusions of this thesis are summarized and discussed with respect to the research objective stated in the first chapter. Next, recommendations are made to pursue this work in order to further increase the knowledge about LIPSS formation.

8.1 Conclusions

The observation of a plethora of laser-induced periodic surface structures (LIPSSs), whose properties could not be explained by the theories developed in the 1980s, triggered intensive studies since the early 2000s. Alternative theories to the classical electromagnetic explanation of LIPSS formation, such as self-organization, were proposed. However, the strong correlation between the geometrical properties of LIPSSs and the electromagnetic properties of the laser radiation suggests that the formation of LIPSSs can be understood from an electromagnetic approach. Therefore, the problem discussed in this thesis was formulated, in chapter 1, as follows: what are the LIPSSs features which can be explained in the frame of an electromagnetic approach?

To that aim, LIPSSs were characterized according to their periodicities and orientations with respect to the polarization of the laser radiation in chapter 2. The most common kind of LIPSSs, the low spatial frequency LIPSSs (LSFLs), are found to develop orthogonal to the polarization with a periodicity slightly smaller than the laser wavelength. These LSFLs can be produced with either continuous wave or pulsed lasers, for a large range of pulse durations, on metals, semiconductors and dielectrics. In contrary to LSFLs, high spatial frequency LIPSSs (HSFLs) develop only when ultra-short laser pulses are applied on metals, semiconductors, dielectrics. That is, pulses in the picosecond or femtosecond regime. The periodicity of HSFLs is significantly smaller than the laser wavelength and their orientation is either

orthogonal or parallel to the polarization. LIPSSs with a periodicity larger than the laser wavelength, referred to as grooves, have also been reported, as well as "fine bumps" with a small periodicity compared to the wavelength, but less directional than HSFLs. From literature, the theory developed by Sipe et al. in 1983, and its extension, the Sipe-Drude theory developed by Bonse et al. in 2009, was identified as the most promising model to explain the formation of LIPSSs.

The Sipe theory and its outcome, the efficacy factor or η map, were presented and discussed in chapter 3. In the framework of the Sipe theory, the interaction of electromagnetic waves with rough surfaces of materials is studied analytically by solving Maxwell's equations. This approach results in the prediction of the frequency domain spectrum of the absorbed energy, just below the rough surface. More precisely, the efficacy factor quantifies the efficacy with which frequency domain components of the spectrum of rough surfaces lead to an inhomogeneous energy absorption. In the η maps, two kinds of frequency domain features were identified: the type-s features and the type-d features, which can account for the formation of LSFLs and HSFLs parallel to the polarization, respectively. However, the Sipe theory cannot explain the formation of HSFLs orthogonal to the polarization, nor the formation of grooves. These limitations were attributed to the approximations and assumptions made by Sipe et al. in the derivation of the efficacy factor.

In order to overcome some of these limitations, a numerical approach, the finite-difference time-domain (FDTD) method, was selected. The theoretical background and expressions required to perform FDTD calculations for electromagnetic plane waves, interacting with rough surfaces, were presented in chapter 4. The total-field scattered-field technique, which allows to introduce plane waves in the simulation domain, was described, as well as the convolution perfectly matched layer (CPML). The latter simulates infinitely extended media. Expressions for FDTD calculations in non-dispersive as well as dispersive media were derived.

In chapter 5, the results of the FDTD simulations were compared to the Sipe theory. A good agreement was found between the two approaches for the type-s features and the type-d features. The use of FDTD calculations showed two advantages over the Sipe theory. First, the FDTD simulations allowed to study the absorbed energy profile in depth, rather than just below the rough surface only. Secondly, the absorbed energy profile could be studied in the space domain instead of just in the frequency domain. Thanks to these two advantages, another type of frequency domain features, referred to as type-r features, was predicted by the FDTD simulations. These features account for the formation of HSFLs orthogonal to the polarization. Moreover, the type-r features showed strong variations of their characteristics, in terms of spread and location in the frequency domain, which coincide with the fact that HSFLs orthogonal to the polarization were reported in literature with quite some variations of periodicity. Frequency domain features corresponding to LIPSSs with periodicities larger than the laser wavelength, referred to as type-g, were also predicted by simulations. The FDTD calculations could explain the formation of many LIPSSs, but it was not clear how the new rough surface, created by the absorbed energy, would enhance LIPSS growth after successive laser pulses.

Therefore, the FDTD method was combined with an holographic ablation model in order to study the effect of inter-pulse feedback mechanisms in chapter 6. This combination, referred to as FDTD-feedback simulations, was able to account for the formation of LSFLs, HSFLs orthogonal to the polarization, HSFLs parallel to the polarization, grooves parallel to the polarization, as well as, complex superimposed LIPSS patterns. The emphasis of the work presented in this chapter was put on the prediction of the HSFLs orthogonal to the polarization, related to the type-r features, because these HSFLs were not predicted by any other model in literature.

Moreover, in chapter 7, the existence of these HSFLs orthogonal to the polarization, related to the type-r features, was shown experimentally. That is, it was shown that these LIPSSs developed on sapphire after femtosecond laser irradiation. The signature of these HSFLs in the frequency domain was used to validate the FDTD-feedback simulations of chapter 6.

Based on the results of the work in this thesis, it can be stated that the formation of nearly any type of LIPSSs can be be explained in the frame of an electromagnetic approach. The only type of LIPSSs which is not predicted by FDTD-feedback simulations are grooves orthogonal to the polarization. Nonetheless, this lack can be attributed to the limitations of the holographic ablation model, in particular to the fact that melting effects are not incorporated.

8.2 Recommendations

The focus of this thesis was on the modeling of LIPSSs using an electromagnetic approach. As a consequence, the holographic ablation model which involves other physical phenomena, such as material removal, is the weakest step of the FDTD-feedback simulations. A better model of the inter-pulse feedback mechanisms would lead to a significant improvement of the simulation results. In particular, HSFLs parallel to the polarization and grooves seem to suffer of this aspect.

Intra-pulse feedback mechanisms were qualitatively taken into account in the FDTD-feedback simulations, by following the same approach as in the Sipe-Drude theory. That is, the optical properties were set, and kept constant during the FDTD calculations, based on the level of excitation modeled. The simulation results would benefit from a more accurate handling of the time dependent variation of the optical properties during the pulse, in particular for semiconductors and dielectrics.

Further, the FDTD-feedback simulations can be simply extended to allow to study LIPSS formation under the influence of circular polarized laser radiation for example. In addition, other kinds of initial rough surfaces can also be used, such as rough surfaces with Gaussian frequency domain spectrums or anisotropic rough surfaces.

Finally, including the effect of the angle of incidence in the FDTD-feedback simulations would provide additional insights. More precisely, this recommendation concerns mainly HSFL formation, since nearly no studies were performed experimentally on the effect of the angle of incidence on the periodicity and direction of HSFLs.

Bibliography

[1] M. Birnbaum. Semiconductor surface damage produced by ruby lasers. *Journal of Applied Physics*, 36:3688–3689, 1965.

[2] M. Siegrist, G. Kaech, and F. Kneubühl. Formation of a periodic wave structure on the dry surface of a solid by TEA-CO_2-laser pulses. *Applied Physics A: Materials Science & Processing*, 2:45–46, 1973.

[3] Y. Jee, Michael F. Becker, and Rodger M. Walser. Laser-induced damage on single-crystal metal surfaces. *Journal of the Optical Society of America B*, 5:648–659, 1988.

[4] D. C. Emmony, R. P. Howson, and L. J. Willis. Laser mirror damage in germanium at 10.6 μm. *Applied Physics Letters*, 23:598–600, 1973.

[5] J. F. Young, J. S. Preston, H. M. van Driel, and J. E. Sipe. Laser-induced periodic surface structure. II. Experiments on Ge, Si, Al, and brass. *Physical Review B*, 27:1155–1172, 1983.

[6] P. Temple and M. Soileau. Polarization charge model for laser-induced ripple patterns in dielectric materials. *IEEE Journal of Quantum Electronics*, 17:2067–2072, 1981.

[7] S. Baudach, J. Bonse, and W. Kautek. Ablation experiments on polyimide with femtosecond laser pulses. *Applied Physics A: Materials Science & Processing*, 69:S395–S398, 1999.

[8] M. Csete, S. Hild, A. Plettl, P. Ziemann, Zs. Bor, and O. Marti. The role of original surface roughness in laser-induced periodic surface structure formation process on poly-carbonate films. *Thin Solid Films*, 453-454:114–120, 2004.

[9] T. Okada, H. Kawahara, Y. Ishida, R. Kumai, T. Tomita, S. Matsuo, S. Hashimoto, M. Kawamoto, Y. Makita, and M. Yamaguchi. Cross-sectional

TEM analysis of laser-induced ripple structures on the 4H-SiC single-crystal surface. *Applied Physics A: Materials Science & Processing*, 92:665–668, 2008.

[10] E. M. Hsu, T. H. R. Crawford, C. Maunders, G. A. Botton, and H. K. Haugen. Cross-sectional study of periodic surface structures on gallium phosphide induced by ultrashort laser pulse irradiation. *Applied Physics Letters*, 92:221112–1–3, 2008.

[11] S. Kaneko, T. Ito, K. Akiyama, M. Yasui, C. Kato, S. Tanaka, Y. Hirabayashi, A. Mastuno, T. Nire, H. Funakubo, and M. Yoshimoto. Nano-strip grating lines self-organized by a high speed scanning CW laser. *Nanotechnology*, 22:175307–1–6, 2011.

[12] J. Bonse, M. Munz, and H. Sturm. Structure formation on the surface of indium phosphide irradiated by femtosecond laser pulses. *Journal of Applied Physics*, 97:013538–1–9, 2005.

[13] J. E. Sipe, J. F. Young, J. S. Preston, and H. M. van Driel. Laser-induced periodic surface structure. I. Theory. *Physical Review B*, 27:1141–1154, 1983.

[14] A. J. Huis in 't Veld and J. van der Veer. Initiation of femtosecond laser machined ripples in steel observed by scanning helium ion microscopy (SHIM). *Journal of Laser Micro/Nanoengineering*, 5:28–34, 2010.

[15] A. Weck, T. H. R. Crawford, D. S. Wilkinson, H. K. Haugen, and J. S. Preston. Ripple formation during deep hole drilling in copper with ultrashort laser pulses. *Applied Physics A: Materials Science & Processing*, 89:1001–1003, 2007.

[16] N. Yasumaru, K. Miyazaki, and J. Kiuchi. Femtosecond-laser-induced nanostructure formed on hard thin films of TiN and DLC. *Applied Physics A: Materials Science & Processing*, 76:983–985, 2003.

[17] J. Bonse, S. Höhm, A. Rosenfeld, and J. Krüger. Sub-100-nm laser-induced periodic surface structures upon irradiation of titanium by Ti:sapphire femtosecond laser pulses in air. *Applied Physics A*, 110:547–551, 2013.

[18] A. Borowiec and H. K. Haugen. Subwavelength ripple formation on the surfaces of compound semiconductors irradiated with femtosecond laser pulses. *Applied Physics Letters*, 82:4462–4464, 2003.

[19] M. Couillard, A. Borowiec, H. K. Haugen, J. S. Preston, E. M. Griswold, and G. A. Botton. Subsurface modifications in indium phosphide induced by single and multiple femtosecond laser pulses: A study on the formation of periodic ripples. *Journal of Applied Physics*, 101:033519–1–8, 2007.

[20] E. M. Hsu, T. H. R. Crawford, H. F. Tiedje, and H. K. Haugen. Periodic surface structures on gallium phosphide after irradiation with 150 fs - 7 ns laser pulses at 800 nm. *Applied Physics Letters*, 91:111102–1–3, 2007.

[21] D. Dufft, A. Rosenfeld, S. K. Das, R. Grunwald, and J. Bonse. Femtosecond laser-induced periodic surface structures revisited: a comparative study on ZnO. *Journal of Applied Physics*, 105:034908–1–9, 2009.

[22] F. Costache, S. Kouteva-Arguirova, and J. Reif. Sub-damage-threshold femtosecond laser ablation from crystalline Si: surface nanostructures and phase transformation. *Applied Physics A: Materials Science & Processing*, 79:1429–1432, 2004.

[23] T. Q. Jia, H. X. Chen, M. Huang, F. L. Zhao, J. R. Qiu, R. X. Li, Z. Z. Xu, X. K. He, J. Zhang, and H. Kuroda. Formation of nanogratings on the surface of a ZnSe crystal irradiated by femtosecond laser pulses. *Physical Review B*, 72:125429–1–4, 2005.

[24] J. Reif, F. Costache, M. Henyk, and S. V. Pandelov. Ripples revisited: non-classical morphology at the bottom of femtosecond laser ablation craters in transparent dielectrics. *Applied Surface Science*, 197-198:891–895, 2002.

[25] F. Costache, M. Henyk, and J. Reif. Surface patterning on insulators upon femtosecond laser ablation. *Applied Surface Science*, 208-209:486–491, 2003.

[26] M. Huang, F. L. Zhao, Y. Cheng, N. Xu, and Z. Xu. Mechanisms of ultrafast laser-induced deep-subwavelength gratings on graphite and diamond. *Physical Review B*, 79:125436–1–9, 2009.

[27] Q. Wu, Y. Ma, R. Fang, Y. Liao, Qi. Yu, X.i Chen, and K. Wang. Femtosecond laser-induced periodic surface structure on diamond film. *Applied Physics Letters*, 82:1703–1705, 2003.

[28] A. J. Huis in 't Veld, M. Groenendijk, and H. Fischer. On the origin, growth and application of ripples. *Journal of Laser Micro/Nanoengineering*, 3:206–210, 2008.

[29] T. H. R. Crawford and H. K. Haugen. Sub-wavelength surface structures on silicon irradiated by femtosecond laser pulses at 1300 and 2100 nm wavelengths. *Applied Surface Science*, 253:4970–4977, 2007.

[30] A. Y. Vorobyev and C. Guo. Colorizing metals with femtosecond laser pulses. *Applied Physics Letters*, 92:041914–1–3, 2008.

[31] B. Dusser, Z. Sagan, H. Soder, N. Faure, J. P. Colombier, M. Jourlin, and E. Audouard. Controlled nanostructrures formation by ultra fast laser pulses for color marking. *Optics Express*, 18:2913–2924, 2010.

[32] N. Yasumaru, K. Miyazaki, and J. Kiuchi. Control of tribological properties of diamond-like carbon films with femtosecond-laser-induced nanostructuring. *Applied Surface Science*, 254:2364–2368, 2008.

[33] J. Eichstädt, G. R. B. E. Römer, and A. J. Huis in 't Veld. Towards friction control using laser-induced periodic surface structures. *Physics Procedia*, 2011.

[34] C. H. Crouch, J. E. Carey, J. M. Warrender, M. J. Aziz, E. Mazur, and F. Y. Genin. Comparison of structure and properties of femtosecond and nanosecond laser-structured silicon. *Applied Physics Letters*, 84:1850–1852, 2004.

[35] T. Baldacchini, J. E. Carey, M. Zhou, and E. Mazur. Superhydrophobic surfaces prepared by microstructuring of silicon using a femtosecond laser. *Langmuir*, 22:4917–4919, 2006.

[36] J. Bonse, H. Sturm, D. Schmidt, and W. Kautek. Chemical, morphological and accumulation phenomena in ultrashort-pulse laser ablation of TiN in air. *Applied Physics A: Materials Science & Processing*, 71:657–665, 2000.

[37] M. Huang, F. L. Zhao, Y. Cheng, N. Xu, and Z. Xu. Origin of laser-induced near-subwavelength ripples: interference between surface plasmons and incident laser. *ACS Nano*, 3:4062–4070, 2009.

[38] J. Bonse, S. Baudach, J. Krüger, W. Kautek, and M. Lenzner. Femtosecond laser ablation of silicon – modification thresholds and morphology. *Applied Physics A: Materials Science & Processing*, 74:19–25, 2002.

[39] J. Bonse and J. Krüger. Pulse number dependence of laser-induced periodic surface structures for femtosecond laser irradiation of silicon. *Journal of Applied Physics*, 108:034903–1–5, 2010.

[40] M. Huang, F. Zhao, Y. Cheng, N. Xu, and Z. Xu. The morphological and optical characteristics of femtosecond laser-induced large-area micro/nanostructures on GaAs, Si, and brass. *Optics Express*, 18:A600–A619, 2010.

[41] J. F. Young, J. E. Sipe, and H. M. van Driel. Laser-induced periodic surface structure. III. Fluence regimes, the role of feedback, and details of the induced topography in germanium. *Physical Review B*, 30:2001–2015, 1984.

[42] A. Taflove and S. C. Hagness. *Computational Electrodynamics: The Finite-Difference Time-Domain Method*. Artech House, Norwood, MA, 3rd edition, 2005.

[43] H. M. van Driel, J. E. Sipe, and J. F. Young. Laser-induced coherent modulation of solid and liquid surfaces. *Journal of Luminescence*, 30:446–471, 1985.

[44] O. Varlamova, F. Costache, J. Reif, and M. Bestehorn. Self-organized pattern formation upon femtosecond laser ablation by circularly polarized light. *Applied Surface Science*, 252:4702–4706, 2006.

[45] J. Reif, O. Varlamova, and F. Costache. Femtosecond laser induced nanostructure formation: self-organization control parameters. *Applied Physics A: Materials Science & Processing*, 92:1019–1024, 2008.

[46] Y. Tang, J. Yang, B. Zhao, M. Wang, and X. Zhu. Control of periodic ripples growth on metals by femtosecond laser ellipticity. *Optics Express*, 20:25826–25833, 2012.

[47] W. C. Shen, C. W. Cheng, M. C. Yang, Y. Kozawa, and S. Sato. Fabrication of novel structures on silicon with femtosecond laser pulses. *Journal of Laser Micro/Nanoengineering*, 5:229–232, 2010.

[48] J. Bonse, J. M. Wrobel, J. Krüger, and W. Kautek. Ultrashort-pulse laser ablation of indium phosphide in air. *Applied Physics A: Materials Science & Processing*, 72:89–94, 2001.

[49] P. T. Mannion, J. Magee, E. Coyne, G. M. O'Connor, and T. J. Glynn. The effect of damage accumulation behaviour on ablation thresholds and damage morphology in ultrafast laser micro-machining of common metals in air. *Applied Surface Science*, 233:275–287, 2004.

[50] P. M. Fauchet and A. E. Siegman. Surface ripples on silicon and gallium arsenide under picosecond laser illumination. *Applied Physics Letters*, 40:824–826, 1982.

[51] T. Tomita, R. Kumai, S. Matsuo, S. Hashimoto, and M. Yamaguchi. Cross-sectional morphological profiles of ripples on Si, SiC, and HOPG. *Applied Physics A: Materials Science & Processing*, 97:271–276, 2009.

[52] J. F. Young, J. E. Sipe, J. S. Preston, and H. M. van Driel. Laser-induced periodic surface damage and radiation remnants. *Applied Physics Letters*, 41:261–264, 1982.

[53] H. M. van Driel, J. E. Sipe, and J. F. Young. Laser-induced periodic surface structure on solids: a universal phenomenon. *Physical Review Letters*, 49:1955–1958, 1982.

[54] Z. Guosheng, P. M. Fauchet, and A. E. Siegman. Growth of spontaneous periodic surface structures on solids during laser illumination. *Physical Review B*, 26:5366–5381, 1982.

[55] A. Y. Vorobyev, V. S. Makin, and C. Guo. Periodic ordering of random surface nanostructures induced by femtosecond laser pulses on metals. *Journal of Applied Physics*, 101:034903–1–4, 2007.

[56] D. Haneman and R. J. Nemanich. Surface topography of laser annealed silicon. *Solid State Communications*, 43:203–206, 1982.

[57] F. Keilmann and Y. H. Bai. Periodic surface structures frozen into CO_2 laser-melted quartz. *Applied Physics A: Materials Science & Processing*, 29:9–18, 1982.

[58] J. Bonse, A. Rosenfeld, and J. Krüger. On the role of surface plasmon polaritons in the formation of laser-induced periodic surface structures upon irradiation of silicon by femtosecond-laser pulses. *Journal of Applied Physics*, 106:104910–1–5, 2009.

[59] L. J. Willis and D. C. Emmony. Laser damage in germanium. *Optics & Laser Technology*, 7:222–228, 1975.

[60] N. Yasumaru, K. Miyazaki, and J. Kiuchi. Glassy carbon layer formed in diamond-like carbon films with femtosecond laser pulses. *Applied Physics A: Materials Science & Processing*, 79:425–427, 2004.

[61] N. Yasumaru, K. Miyazaki, and J. Kiuchi. Fluence dependence of femtosecond-laser-induced nanostructure formed on TiN and CrN. *Applied Physics A: Materials Science & Processing*, 81:933–937, 2005.

[62] H. Varel, M. Wähmer, A. Rosenfeld, D. Ashkenasi, and E. E. B. Campbell. Femtosecond laser ablation of sapphire: time-of-flight analysis of ablation plume. *Applied Surface Science*, 127-129:128–133, 1998.

[63] A. M. Ozkan, A. P. Malshe, T. A. Railkar, W. D. Brown, M. D. Shirk, and P. A. Molian. Femtosecond laser-induced periodic structure writing on diamond crystals and microclusters. *Applied Physics Letters*, 75:3716–3718, 1999.

[64] F. Costache, M. Henyk, and J. Reif. Modification of dielectric surfaces with ultra-short laser pulses. *Applied Surface Science*, 186:352–357, 2002.

[65] S. Höhm, A. Rosenfeld, J. Krüger, and J. Bonse. Femtosecond laser-induced periodic surface structures on silica. *Journal of Applied Physics*, 112:014901–1–9, 2012.

[66] V. I. Emel' yanov, E. M. Zemskov, and V. N. Seminogov. Theory of formation of surface gratings under the action of laser radiation on surfaces of metals, semiconductors, and insulators. *Soviet Journal of Quantum Electronics*, 13:1556–1561, 1983.

[67] S. E. Clark, N. C. Kerr, and D. C. Emmony. Anomalous laser-induced periodic surface structures. *Journal of Physics D: Applied Physics*, 22:527–534, 1989.

[68] S. A. Maier. *Plasmonics Fundamentals and Applications*. Springer, 2007.

[69] J. Wang and C. Guo. Formation of extraordinarily uniform periodic structures on metals induced by femtosecond laser pulses. *Journal of Applied Physics*, 100:023511–1–4, 2006.

[70] F. Garrelie, J. P. Colombier, F. Pigeon, S. Tonchev, N. Faure, M. Bounhalli, S. Reynaud, and O. Parriaux. Evidence of surface plasmon resonance in ultrafast laser-induced ripples. *Optics Express*, 19:9035–9043, 2011.

[71] H. Raether. *Surface Plasmons on Smooth and Rough Surfaces and on Gratings*. Springer-Verlag, 1988.

[72] A. Borowiec, M. Couillard, G. A. Botton, and H. K. Haugen. Sub-surface damage in indium phosphide caused by micromachining of grooves with femtosecond and nanosecond laser pulses. *Applied Physics A: Materials Science & Processing*, 79:1887–1890, 2004.

[73] J. C. Koo and R. E. Slusher. Diffraction from laser-induced deformation on reflective surfaces. *Applied Physics Letters*, 28:614–616, 1976.

[74] H. J. Leamy, G. A. Rozgonyi, T. T. Sheng, and G. K. Celler. Periodic regrowth phenomena produced by laser annealing of ion-implanted silicon. *Applied Physics Letters*, 32:535–537, 1978.

[75] R. Buividas, L. Rosa, R. Sliupas, T. Kudrius, G. Slekys, V. Datssyuk, and S. Juodkazis. Mechanism of fine ripple formation on surfaces of (semi)transparent materials via a half-wavelength cavity feedback. *Nanotechnology*, 22:055304–1–6, 2011.

[76] J. Reif, O. Varlamova, S. Varlamov, and M. Bestehorn. The role of asymmetric excitation in self-organized nanostructure formation upon femtosecond laser ablation. *Applied Physics A: Materials Science & Processing*, 104:969–973, 2011.

[77] E. Palik. *Handbook of Optical Constants of Solids*. Elsevier Science, 1985.

[78] J. E. Sipe, H. M. Van Driel, and J. F. Young. Surface electrodynamics: radiation fields, surface polaritons, and radiation remnants. *Canadian Journal of Physics*, 63:104–113, 1985.

[79] K. S. Yee. Numerical solution of initial boundary value problems involving maxwell's equations in isotropic media. *IEEE Transactions on Antennas and Propagation*, 14:302–307, 1966.

[80] A. Taflove. Application of the finite-difference time-domain method to sinusoidal steady-state electromagnetic-penetration problems. *IEEE Transactions on Electromagnetic Compatibility*, EMC-22:191–202, 1980.

[81] D. B. Davidson. *Computational Electromagnetics for RF and Microwave Engineering*. Cambridge University Press, 2005.

[82] J. D. Jackson. *Classical Electrodynamics*. John Wiley & Sons, 3rd edition, 1999.

[83] M. Okoniewski, M. Mrozowski, and M. A. Stuchly. Simple treatment of multi-term dispersion in FDTD. *Microwave and Guided Wave Letters, IEEE*, 7:121–123, 1997.

[84] A. Taflove and M. E. Brodwin. Numerical solution of steady-state electromagnetic scattering problems using the time-dependent Maxwell's equations. *IEEE Transactions on Microwave Theory and Techniques*, 23:623–630, 1975.

[85] J. A. Pereda, O. Garcia, A. Vegas, and A. Prieto. Numerical dispersion and stability analysis of the FDTD technique in lossy dielectrics. *Microwave and Guided Wave Letters, IEEE*, 8:245–247, 1998.

[86] K. Chun, H. Kim, H. Kim, and Y. Chung. PLRC and ADE implementations of Drude-critical point dispersive model for the FDTD method. *Progress In Electromagnetics Research*, 135:373–390, 2013.

[87] R. E. Mickens. *Advances in the Applications of Nonstandard Finite Diffference Schemes*. World Scientific Publishing Company, 2005.

[88] A. A. Kokhanovsky. *Light Scattering and Remote Sensing of Atmosphere and Surface*, volume 6 of *Light Scattering Reviews*. Springer, 2012.

[89] J. A. Roden and S. D. Gedney. Convolution PML (CPML): an efficient FDTD implementation of the CFS-PML for arbitrary media. *Microwave and Optical Technology Letters*, 27:334–339, 2000.

[90] J. P. Berenger. A perfectly matched layer for the absorption of electromagnetic waves. *Journal of Computational Physics*, 114:185–200, 1994.

[91] O. Varlamova, M. Bounhalli, and J. Reif. Influence of irradiation dose on laser-induced surface nanostructures on silicon. *Applied Surface Science*, 278:62–66, 2013.

[92] J. W. Yao, C. Y. Zhang, H. Y. Liu, Q. F. Dai, L. J. Wu, S. Lan, A. V. Gopal, V. A. Trofimov, and T. M. Lysak. High spatial frequency periodic structures induced on metal surface by femtosecond laser pulses. *Optics Express*, 20:905–911, 2012.

[93] J. M. Liu. Simple technique for measurements of pulsed Gaussian-beam spot sizes. *Optics Letters*, 7:196–198, 1982.

Nomenclature

Notations

$\vec{\bullet}$	Vector
$\|\vec{\bullet}\|$	Norm of $\vec{\bullet}$
$\hat{\bullet}$	Normalized vector $\vec{\bullet}/\|\vec{\bullet}\|$
$\tilde{\bullet}$	Fourier transform of the $\bullet$ function
$\tilde{\bullet}$	$\bullet$ is complex
$\|\bullet\|$	Absolute value of $\bullet$
$\bar{\bullet}$	Complex conjugate of $\bullet$
$\mathrm{Re}(\bullet)$	Real part of $\bullet$
$\mathrm{Im}(\bullet)$	Imaginary part of $\bullet$
$\partial \bullet / \partial t$	First order partial derivative of $\bullet$ with respect to t
$\partial^2 \bullet / \partial t^2$	Second order partial derivative of $\bullet$ with respect to t
$\vec{\nabla} \cdot \vec{\bullet}$	Divergence of $\vec{\bullet}$
$\vec{\nabla} \times \vec{\bullet}$	Rotational, or curl, of $\vec{\bullet}$
$\vec{\bullet} \cdot \vec{\bullet}$	Scalar product or dot product
$e^{\bullet}$	Exponential of $\bullet$
$\cos(\bullet)$	Cosine of $\bullet$
$\sin(\bullet)$	Sine of $\bullet$
$O[\bullet]$	Big O notation

Abbreviations

ADE	Auxiliary differential equation
CPML	Convolutional perfectly matched layer
FEM	Finite element method
FDTD	Finite-difference time-domain

HAM	Holographic ablation model
HSFL	High spatial frequency LIPSS
LIPSS	Laser-induced periodic surface structures
LSFL	Low spatial frequency LIPSS
MoM	Method of moments
SEM	Scanning electron microscopy
SHG	Second-harmonic generation
SPP	Surface plasmon polariton
TF	Total-field
TM	Transverse magnetic
SF	Scattered-field
TFSF	Total-field scattered-field

Greek symbols

α	Coefficient used in the ADE method	[-]
β	Coefficient used in the ADE method	[F/m.s]
γ	Characteristic frequency of the electron collisions $1/\tau_{\text{Drude}}$	[1/s]
Δ_{ablation}	Ablation depth	[m]
$\delta(\vec{r})$	Dirac delta function	[-]
δ	Depth below the rough surface	[m]
ε_0	Permittivity of vacuum	[F/m]
ε_r	Relative permittivity of a material	[-]
$\tilde{\varepsilon}$	Complex permittivity of a material	[-]
$\tilde{\varepsilon}_r$	Complex relative permittivity of a material	[-]
$\tilde{\varepsilon}_r^*$	Complex relative permittivity of an excited material	[-]
$\Delta\tilde{\varepsilon}_{\text{Drude}}$	Drude contribution to the variation of the complex relative permittivity of excited materials	[-]
$\eta(\vec{k}, \vec{k}_i)$	Efficacy factor	[-]
$\eta(\vec{k})$	Efficacy factor with $\vec{k}_i$ omitted	[-]
Θ	Heaviside, or unit, step function	[-]
θ	Angle of incidence of the laser beam	[°]
Λ	Periodicity of LIPSS	[m]
λ	Wavelength of the laser radiation	[m]
μ_0	Permeability of vacuum	[H/m]
$\xi_{\max}$	Maximum of the polynomial ξ	[-]
ξ	Polynomial used to define ψ_1 and ψ_2	[-]
σ	Conductivity of a material	[S/m]
$\rho_{\max}$	Maximum of the polynomial ρ	[-]
ρ	Polynomial used to define ψ_1 and ψ_2	[-]
$\vec{\rho}$	Vector spanning the $(\vec{x}, \vec{y})$ plane	[m]
τ	Laser pulse duration	[s]
τ_{Drude}	Drude damping time	[s]

ϕ	Fluence	[J/m^2]
ϕ_0	Peak fluence of a Gaussian distribution	[J/m^2]
χ	Dielectric susceptibility of a material	[-]
Ψ_E	Function modifying $\vec{E}$ in the CPML	[A/m^2]
Ψ_H	Function modifying $\vec{H}$ in the CPML	[V/m^2]
ψ_1	Coefficient used to define Ψ_E and Ψ_H	[-]
ψ_2	Coefficient used to define Ψ_E and Ψ_H	[-]
$\Omega_{\delta,\mathrm{N_e}}$	Set of frequencies extracted from an FDTD-η map computed at δ and N_e	[-]
ω	Angular frequency	[rad/s]
ω_p	Plasma frequency of the electron gas	[rad/s]
ω_0	$1/\mathrm{e}^2$ Gaussian beam radius	[m]

Roman symbols

$\mathrm{A}_{\delta,\mathrm{N_e}}$	Area covered by the frequencies in Ω	[-]
$A(x,y,z)$	Absorbed energy in the medium	[J]
$A(\vec{k})$	Fourier component of the absorbed energy just below the rough surface at $\vec{k}$	[J]
A_{ablation}	Absorbed energy necessary to remove a layer with a thickness $\Delta_{\mathrm{ablation}}$ of material from the surface	[J]
$\vec{B}$	Magnetic flux density	[T]
$b(x,y)$	Binary function used to describe rough surfaces in the Sipe theory	[-]
$b(\vec{k})$	Fourier component of the rough surface at $\vec{k}$	[-]
c	Speed of light in vacuum	[m/s]
$\vec{D}$	Electric flux density	[C/m^2]
$\vec{E}$	Electric field	[V/m]
$\vec{E}_{\mathrm{int}}$	Incident electric field	[V/m]
$\vec{E}_{\mathrm{scat}}$	Scattered electric field	[V/m]
E_p	Pulse energy	[J]
e	Elementary charge	[C]
F	Filling factor	[-]
$f_{\delta,\mathrm{N_e}}(\vec{k})$	Amplitude of the frequency of an FDTD-η map located at $\vec{k}$	[J]
f	Focal length of a lens	[m]
$\vec{H}$	Magnetic field	[A/m]
$\vec{H}_{\mathrm{inc}}$	Incident magnetic field	[A/m]
$\vec{H}_{\mathrm{scat}}$	Scattered magnetic field	[A/m]
h	(Averaged) peak to valley height	[m]
i,j,k	Space indices	[-]
$\vec{J}_{\mathrm{Drude}}$	Drude internal current	[A/m^2]

$\vec{J}$	Drude internal current with omitted subscript	[A/m^2]
j	Imaginary unit	[-]
$\vec{k}$	Normalized vector spanning the frequency domain in the $(\vec{x},\vec{y})$ plane	[-]
k_x	Component of $\vec{k}$ along the $\vec{x}$ axis	[-]
Δk_x	Frequency domain increment along the $\vec{x}$ axis	[-]
k_y	Component of $\vec{k}$ along the $\vec{y}$ axis	[-]
Δk_y	Frequency domain increment along the $\vec{y}$ axis	[-]
$\vec{\kappa}$	Wave vector	[1/m]
$\vec{k}_i$	Component of the wave vector parallel to the $(\vec{x},\vec{y})$ plane	[1/m]
l_s	Thickness of the selvedge	[m]
$\mathrm{M}_{\delta,\mathrm{N_e}}$	Maximum value of $f_{\delta,\mathrm{N_e}}(\vec{k})$	[J]
$\vec{M}$	Magnetization	[A/m]
m	Number of time steps	[-]
m_{eff}	Effective optical mass	[kg]
m_e	Electron mass	[kg]
m_{opt}	Optical mass	[-]
m_ξ	Order of the polynomial ξ	[-]
m_ρ	Order of the polynomial ρ	[-]
N_{med}	Number of Yee cells in the CPML of the medium	[-]
N_e	Density of free electrons	[1/m^3]
N	Number of pulses	[-]
$\tilde{n}$	Complex refractive index	[-]
$\tilde{n}^*$	Complex refractive index of an excited material	[-]
$\vec{P}$	Polarization	[C/m^2]
$\vec{P}^*$	Polarization of an excited material	[C/m^2]
$\vec{P}_{\mathrm{Drude}}$	Polarization of the material linked to the free electrons	[C/m^2]
$\vec{p}$	p-polarization	[-]
$\vec{r}$	Vector spanning the space domain	[m]
s	Shape factor	[-]
$\vec{s}$	s-polarization	[-]
t	Time	[s]
$\Delta t_{\max}$	Maximum time increment to ensure the stability of the FDTD algorithm	[s]
Δt	Time increment	[s]
$\vec{u}$	Unit vector	[-]
$\mathrm{W}_{\delta,\mathrm{N_e}}$	Weighted arithmetic mean of the position of the frequencies in Ω	[-]
x, y, z	Cartesian coordinates	[m]
Δx	Dimension of Yee cells in the $\vec{x}$ direction	[m]
Δy	Dimension of Yee cells in the $\vec{y}$ direction	[m]
yc	Yee cell	[-]
Δz	Dimension of Yee cells in the $\vec{z}$ direction	[m]

Acknowledgments

After four years of research, it is with great pleasure that I present this work. As I often say, it is not the place where you are which matters, it is the people you meet. These four years as PhD candidate are no exception. I met incredible persons during this journey, who contributed directly or indirectly to my research. I would like to seize the opportunity to acknowledge them.

Firstly, I acknowledge my promoter and assistant promoter, Bert Huis in't Veld and Gert-willem Römer. Bert, I thank you for accepting me in your research group and helping me to spread the outcome of my work. I appreciated that you always found time to discuss openly on any subjects, and gave me a lot of freedom to orientate my research. Gert-willem, my articles and this thesis would not have reached the same quality without your help, thank you. You even managed to make me create a Gantt chart, which was not an easy task. Secondly, I acknowledge the Materials innovation institute (M2i), and the industrial partners, for hiring me in the framework of the Texturing using Ultrashort Laser Pulses (TULP) project. On the experimental side, I thank Leo Tiemersma, Gerald Ebberink, Jozef Vincenc Obona, Vasek Ocelik and Jeff de Hosson. Leo and Gerald, many thanks for preparing the samples and helping me in the laboratory. Jozef, thank you for performing crucial experiments and analyzing the samples exhaustively. Vasek and Jeff, thanks for the support in Groningen. I enjoyed our discussions and I am grateful that Jeff granted Jozef the access to the facilities of his research group in Groningen. Furthermore, I would like to thank the members of my graduation committee – prof J. Reif, prof. J.Th.M. De Hosson, prof. K.J. Boller, prof. H.J.W. Zandvliet and prof. A.H. van den Boogaard – for taking their time to evaluate my thesis. Jürgen, thank you for traveling to be present at my defense. Many thanks to Martina Tjapkes for assisting me with the administration, and most importantly to try to make me smile every day of my PhD years.

I would like to acknowledge my colleagues from the mechanical automation group. Ger, I hope we will keep in touch, I will need your tips and tricks the next time I use a barbecue. Bert, we should have gone out more often, it seems you are a different person after drinking a certain beverage. Dirk, I did my best to defend my title as

best PhD of the group, I let you judge if I managed. Jitendra, I had a lot of fun going to the Dutch lessons with you. Niya, thank you for the cooking sessions. However, I would recommend you to stop putting nickel or other metals in your recipes. Ralph, I am glad I met you. It made me realize that I am not as nerdy as I thought after all. I enjoyed our various talks in the corridors, the trip to Germany, and your tireless good mood. Davide, I always wondered if you really were Italian. You barely speak with your hands, and I wished you had a "volume" button many times. Stefan, thank you for joining the lunch breaks, we had good times. I hope you take good care of your minions, now that I am not present to watch for them anymore. Dannis, talking about lunch breaks, I was only partly involved in the flying tomato story. Now, I can admit it, I was always jealous of your red pants and pink shirt. I thank Ronald, Ben, Pathiraj, Johannes, Ali, Wilco, Frank, Jonathan, Volkert and Jaap for the discussions during the coffee breaks.

I consider these four years as PhD candidate to be the best years of my life so far. This would not be the case without all the friends I made inside the research group, but also outside. Unfortunately, I am not able to cite all of them since I do not want to double the printing costs. However, I know people look at this part of the thesis to see if their names are cited, and read crusty stories. I tried to remember few to write these lines. Niels, thank you for your burger recipe. I do not know what I would have eaten during my 4^{th} year without you. I could write down the Lady Gaga joke or the "dog in a bag" story, but I let people ask you about them. Jasper, I never met someone that handsome. I appreciated that you returned the compliments back each time. Maria, even if we both know it is impossible, I hope you will find a dance partner that you like as much as me. Olga, I am glad you finally managed to stop stalking me. Burcu, in one word: bonjour. Nana, there is much and more to be said, but everything can be summarized by one quote "great minds think alike". You said this so many times, I actually started to believe that I am smart. Mihaela, I know it is hard not to come from Sibiu. Barry, thanks for the music. You managed to make my evenings at Molly Malone memorable. Clémence, I missed you and your sushi addiction. Alexandre, many thanks for giving me the template of your thesis, it was really helpful. Satadal, you arrived four years too late, which seems quite good for my reputation considering the photos you take of me. Alicia, do not forget you are one of the three musketeers, I hope you still party as such.

During a PhD, there is a place that you better enjoy: the office. I shared mine with four incredible persons, that I will not manage to thank enough. Paul, I cannot count how many times you helped me with my code, computer problems, Dutch documents... I appreciated your logic when facing any scientific problems. After spending three years in the same office, I can tell that you did not usurp your nickname: Walking Wiki. On top of this, you are capable of incredible imitations, such as the bouncing electron or the "fucked-up" laser beam, which definitely helps to understand physics. I would like to thank you for all this, for being a friend, and for our numerous discussions about the news in the office or around a beer. Jozef, let me thank you once again for helping me during my four years of research. The outcome would not be the same without your careful analyzes and experiments. You showed an incredible patience regarding my, sometimes lapidary, style of discussion. Most of all, I thank you for

your friendship. Through it, we illustrated boldly our favorite quote: “no great story starts with a salad”. Thank you for being there during the ups and dawns, and for all the memories... I am afraid that the list of private jokes is too long to be written here. Justus, two weeks after I started my PhD, I remember finding a strange German guy on the right side of my desk. While I could hardly find my keyboard, buried below stacks of papers, his desk was suspiciously clean. His tightly timed agenda contrasted severely with mine, nonexistent. One can hardly imagine such an opposition of style, but I would not have changed this for anything at all. Thank you for your unquenchable support. You taught me how to align a laser system and how to perform careful experiments. You helped me selflessly when I needed it the most, by offering your time and using your organization skills. Thank you for accepting to be one of my paranymphs, as a coworker and a friend. Steven, yes, I count you as an office member since you spent almost all your breaks in it. Although, I am glad you were not “working” in this office, we both know we would never have finished to write our thesis in that case. You blamed me for not finishing on time because of our night partying habits, but I am sure it was an excellent creativity boost. Anyway, my PhD years would not have had the same flavor without you, and I gladly take the blame. I have so many anecdotes, discussions and great stories in mind that I do not dare to start writing them down. Thank you for all these memories, for accepting to be one of my paranymphs, and for your unconditional friendship.

Mes derniers remerciements vont à tous les membres de ma famille, mes cousins et cousines, oncles et tantes, parrain et marraine, parents et grands-parents. Papa et maman, ces vingt-huit années n’ont pas toujours été de tout repos, et ces quatre dernières années ont aussi eu leur lot d’émotions. Ainsi, vous faites partie des rares parents à avoir donné la vie à un seul enfant, par deux fois! Et ces deux fois, j’ai eu une chance incroyable. Je veux vous remercier pour votre inébranlable soutien, votre amour, et pour l’éductation que vous m’avez donnée. Maman, merci d’avoir été aussi présente, attentive, douce et aimante, dans les bons et les mauvais moments. J’espère que nous partageront encore de nombreux moments en cuisine, tu n’as pas encore fini d’apprendre des choses à ton fils. Papa, les gens qui pensent que tu es un motard, un médecin et un père, ont raison, mais ils n’ont pas tout compris. Avant tout, tu es un philosophe de la vie et du bonheur. C’est avec admiration que j’essaye de m’approprier cet héritage. J’attend avec impatience nos prochaines parties de golf sous le soleil. Mes chers parents, en un mot, merci.

“To the Happy Few”

Marie-Henri Beyle

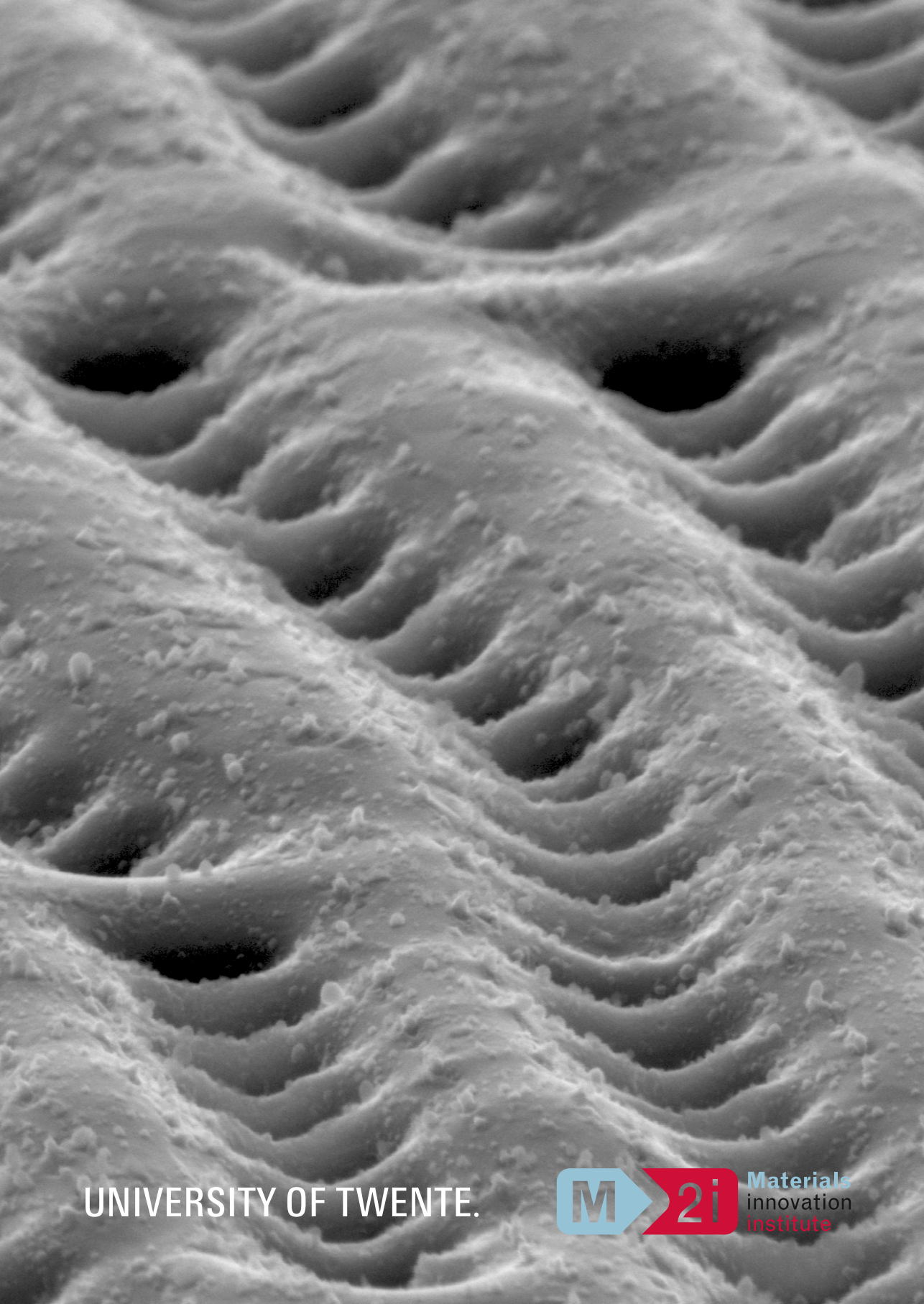

UNIVERSITY OF TWENTE.

Materials innovation institute